ALMA MATER STUDIORUM · UNIVERSITÀ DI BOLOGNA

DOTTORATO DI RICERCA IN
FISICA
Ciclo 34

Settore Concorsuale: 02/A1 - FISICA SPERIMENTALE DELLE INTERAZIONI FONDAMENTALI
Settore Scientifico Disciplinare: FIS/01 - FISICA SPERIMENTALE

The FOOT experiment: Trigger and Data Acquisition (TDAQ) development and data analysis

Presentata da: Riccardo Ridolfi

Coordinatore Dottorato
Prof. Michele Cicoli

Supervisore
Prof. Mauro Villa

Co-supervisore
Dott. Roberto Spighi

Esame finale anno 2022

Anything we can actually do
we can afford.
J.M. Keynes

Abstract

Hadrontherapy employs high-energy beams of charged particles (protons and heavier ions) to treat deep-seated tumours: these particles have a favourable depth-dose distribution in tissue characterized by a low dose in the entrance channel and a sharp maximum (Bragg peak) near the end of their path. Moreover, Carbon and Oxygen ions have an enhanced biological effect allowing to successfully treat radioresistant tumours. In these treatments nuclear interactions have to be considered: beam particles can fragment in the human body releasing a non-zero dose beyond the Bragg peak while fragments of human body nuclei can modify the dose released in healthy tissues. These effects are still in question given the lack of interesting cross sections data. Also space radioprotection can profit by fragmentation cross section measurements: the interest in long-term manned space missions beyond Low Earth Orbit is growing in these years but it has to cope with major health risks due to space radiation. To this end, risk models which are highly dependent on underlying physical models are under study: however, huge gaps in fragmentation cross sections data are currently present preventing an accurate benchmark of deterministic and Monte Carlo codes. To fill these gaps in data, the FOOT (FragmentatiOn Of Target) experiment was proposed. It is composed by two independent and complementary setups, an Emulsion Cloud Chamber and an electronic setup composed by several subdetectors providing redundant measurements of kinematic properties of fragments produced in nuclear interactions between a beam and a target. FOOT was designed to detect, track and identify nuclear fragments and aims to measure double differential cross sections both in angle and kinetic energy which is the most complete information to address existing questions. In this Ph.D. thesis, the development of the Trigger and Data Acquisition system for the FOOT electronic setup and a first analysis of 400 MeV/u ^{16}O beam on Carbon target data acquired in July 2021 at GSI (Darmstadt, Germany) are presented. When possible, a comparison with other available measurements is also reported.

Sommario

L'adroterapia è una tecnica di radioterapia esterna nella quale vengono utilizzati fasci di ioni (protoni e ioni più pesanti) ad alta energia per il trattamento di tumori profondi: tali particelle hanno una distribuzione dose-profondità nel tessuto molto favorevole, caratterizzata da un basso rilascio di dose nel canale di entrata e un massimo pronunciato (picco di Bragg) vicino alla fine del loro percorso. Inoltre gli ioni carbonio e ossigeno mostrano un effetto biologico più significativo che permette di trattare con successo anche i tumori radioresistenti. In tali trattamenti devono essere prese in considerazione anche le interazioni nucleari: le particelle del fascio possono frammentare nel corpo umano rilasciando una dose non nulla oltre il picco di Bragg mentre i frammenti dei nuclei del paziente possono modificare la dose rilasciata nei tessuti sani. L'entità di tali effetti è attualmente oggetto di studio vista l'assenza di misure sulle sezioni d'urto di interesse. Anche il campo della radioprotezione spaziale può trarre benificio da queste misure: in questi anni sta crescendo infatti l'interesse per le missioni spaziali con equipaggio oltre la bassa orbita terrestre ma i rischi per la salute causati dalla radiazione spaziale rimangono un grande problema da affrontare. Per questo motivo si studiano modelli di rischio che sono però molto dipendenti dai modelli fisici di partenza e risentono quindi della significativa mancanza di dati sulle sezioni d'urto impedendo così un accurato confronto con i codici deterministici e Monte Carlo. L'esperimento FOOT (FragmentatiOn Of Target) è stato proposto proprio per misurare queste sezioni d'urto mancanti: esso è composto da due apparati indipendenti e complementari, una *Emulsion Cloud Chamber* e un apparato elettronico composto da alcuni rivelatori che forniscono misure ridondanti delle quantità cinematiche dei frammenti nucleari prodotti dalle interazioni tra il fascio ed il bersaglio. FOOT è stato progettato per rivelare, tracciare ed identificare i frammenti nucleari con l'obiettivo di misurare le sezioni d'urto differenziali sia in angolo che in energia cinetica, informazioni fondamentali per rispondere ai problemi aperti. In questa tesi sono presentati sia lo sviluppo del sistema di trigger e acquisizione dati (TDAQ) per l'apparato elettronico dell'esperimento sia una prima analisi dei dati del fascio di ^{16}O a 400 MeV/u su un bersaglio di carbonio acquisiti a luglio 2021 presso il GSI (Darmstadt, Germania) oltre ad un confronto, quando possibile, con altre misure attualmente disponibili.

Contents

Introduction

Hadrontherapy is an external radiation therapy technique in which protons and heavier ions are used to treat deep-seated solid tumours. The main advantage to use charged particles to treat tumours is their favourable depth-dose profile which is very different from that of photons used in conventional radiation therapy. Indeed, while a photon beam reduces its intensity exponentially as it enters into a material, charged particles are characterised by a low energy release in the beginning followed by a sharp rise after which the particle stops (Bragg peak). This peculiar behaviour makes charged particles particularly suitable to treat tumours near critical organs that must be spared by the radiation, especially in younger patients. Moreover, the electric charge of hadrons allows to actively move the beam to cover all the tumour volume. Furthermore, heavier ions such as Carbon and Oxygen can play an important role in treating radioresistant tumours thanks to their enhanced biological effectiveness.

However, nuclear interactions have to be accounted for: beam particles can fragment in the human body producing low charge nuclei and these fragments are able to release a non-zero dose beyond the Bragg peak. This contribution has to be properly described. On the other hand, nuclear interactions providing the fragmentation of nuclei of the human body give rise to target fragments with low energy. These nuclear fragments can modify the dose released in healthy tissues and their effects are still in question given the lack of accurate cross sections data.

The study of such nuclear interactions is of strong interest also in the space radioprotection field. Indeed, the interest in long-term manned space missions beyond the Low Earth Orbit is growing in these years, both in national space agencies and in public-private sector. However, the health risks linked to space radiation are a major hazard which can potentially prevent any mission due to huge costs and unacceptable risks for the astronauts. For this reason, several mitigation strategies are employed, such as an intense development of risk models which strongly depend on the knowledge of underlying physical and radiobiological models. However, there are huge gaps in fragmentation cross sections data which are needed to benchmark both deterministic and Monte Carlo models currently in use.

To address all these questions, the FOOT (*FragmentatiOn Of Target*) experiment was proposed. It is composed by two independent and complementary setups, an Emulsion Cloud Chamber and an electronic setup composed by several subdetectors providing redundant measurements of kinematic properties of fragments produced in nuclear interactions between a beam and a target. FOOT was designed to detect, track and identify nuclear fragments and aims to measure double differential cross section both in angle and kinetic energy. Indeed, this would be the most significant contribution of experimental nuclear physics to the field providing the most complete information to develop a new generation of treatment planning system for patients, of transport codes and of risk models for space radioprotection. Thanks to its table top setup, the FOOT experiment can be mounted in several experimental rooms both in research centres and in clinical facilities to harness the available variety of beams and energies. Indeed, the core program of the experiment foresees the use of 250 MeV/u ^{4}He beams and $200-400$ MeV/u ^{12}C, ^{16}O beams with C, C_2H_4 and PMMA targets to measure fragmentation cross sections for hadrontherapy while $700-800$ MeV/u ^{4}He, ^{12}C and ^{16}O beams with C, C_2H_4 and PMMA targets for space radioprotection. Thanks to its flexibility, the experiment will be able to extend its physics program to other beam-target settings to possibly cover other data gaps.

The aim of this Ph.D. project was twofold, i.e. the development of the Trigger and Data Acquisition system for the FOOT electronic setup and a first analysis of 400 MeV/u ^{16}O beam on Carbon target data acquired in July 2021 at GSI (Darmstadt, Germany). The TDAQ system designed for the whole apparatus is a flexible hierarchical distributed system based on Linux PCs, VME crates and boards, detector integrated readout systems and standard communication links like Ethernet, USB and optical fibers. Given the large number of different subdetectors, its architecture is similar to that of bigger particle physics experiments. Thus, it is crucial to assure the synchronization among all the detectors and to design a safe dataflow from frontend electronics to data storage. In this context, this work aims to develop the Beam Monitor readout with Time to Digital Converter (TDC) and the remote detectors consisting in custom electronics. In the former case the TDC is hosted in a VME crate read via USB or optical fiber while in the latter detectors are connected via Ethernet. Moreover, an online data monitoring framework was developed to check both beam and detector status to promptly cope with issues and misalignments.

Furthermore, using GSI 2021 data sample, a first fragmentation cross section analysis, both total and differential in angle, is presented. To evaluate detection efficiency an analysis of Monte Carlo samples was carried out before analyzing acquired data together with a careful check on the alignment of interesting detectors. The charge of fragments was evaluated using the Tof Wall detector as well as the production angle. To this end, both minimum bias and fragmentation runs were used together with a run without target to estimate the uninteresting fragmentation events.

In Chapter 1, an overview of the underlying physics of the interactions of charged particles in matter will be presented. In Chapter 2, a focus on hadrontherapy and on its physics basis with a focus on the role of nuclear fragmentations will be set out. In Chapter 3 an overview on space radioprotection will be set out, from the description of the space radiation environment to shielding studies. In Chapter 4, a complete overview of the FOOT experiment, i.e. the setup, the physics program with current experimental panorama and the event reconstruction strategies will be presented. In Chapter 5, after an introduction on general concepts of data acquisition systems, the FOOT TDAQ system is presented. Then, the description of the implementation of VME and remote detectors in the system together with its performances under different settings will be reported. In Chapter 6, a first analysis on GSI 2021 data will be presented. Preliminary measurements of the elemental fragmentation cross sections for different produced charges have been obtained together with the first evaluations of the differential cross sections as a function of the fragment direction angle. When possible, a comparison with other available measurements is also reported.

Chapter 1

Interactions of charged particles in matter

Heavy charged particles, such as protons or heavier nuclei, undergo several interactions as they traverse a medium. These particles interact mainly with orbital electrons of atoms of the medium through inelastic interactions: this is the most important process for the energy loss. After the interaction, orbital electrons can have absorbed enough energy to jump to a higher level orbital (*excitation*) or to be completely removed from the atom (*ionization*). Moreover, also elastic interactions with nuclei of the medium may occur, thus contributing to the deflection of the particle. On the other side, nuclear interactions can play an important role: even if the probability for these interactions to occur is much smaller than the inelastic collision with atomic electrons, this contribution can become really important at large penetration depths and it has to be considered both in particle therapy and in space radioprotection field. In this chapter a wide introduction on the interactions of charged particles in matter will be given: regarding the electromagnetic interaction the Bethe-Bloch formula and the Multiple Coulomb Scattering will be presented including their statistical fluctuations. Then the phenomenology of nuclear interactions will be presented, focusing on those aspects that will turn to be very important in hadrontherapy and radioprotection in space.

1.1 The energy loss of massive charged particles

When a heavy charged particle, such as a proton, enters an absorbing medium, it immediately interacts simultaneously with a lot of electrons. In each interaction, the electron feels an impulse from the attractive electromagnetic Coulomb force as the particle passes nearby. Depending on the distance, this impulse may be sufficient either to raise the electron to a higher-lying shell within the absorber atom (*excitation*) or to remove completely the electron from the atom (*ionization*). The energy transferred to the electron comes from the kinetic energy of the incoming particle: thus, as a result of the interaction, the particle slows down [1]. From the relativistic two-body scattering calculation, the maximum energy which can be transferred from a charged particle of mass m with kinetic energy E_K to an electron of mass m_e in a single collision is $\approx 4E_K m_e/m$, i.e. about $1/500$ of the particle energy per nucleon. Since this is a small fraction of the total energy, the particle will interact many times before losing all its energy. As the number of these interactions is huge at any given time, the slowing-down of the particle can be considered as a continuous process and it is possible to define the so-called *stopping power*.

Along the path, the track of the primary particle remains almost straight since it is not deflected by these inelastic interactions occurring randomly in all directions. This means that for heavy charged particles it is possible to define also a *range*, i.e. the average length a particle of a given energy could travel in a given absorber.

1.1.1 The Bethe-Bloch formula

The linear stopping power S for charged particles in a given absorber is defined as the differential energy loss divided by the corresponding differential path length:

$$S = -\frac{\mathrm{d}E}{\mathrm{d}x}. \tag{1.1}$$

Its value depends on both the particle and absorber type. The value of $-\mathrm{d}E/\mathrm{d}x$ along a particle track is also called its *specific energy loss* and it represents a friction force experienced by the travelling particle. This quantity was first calculated by Bohr using classical arguments and later by Bethe, Bloch and others using quantum mechanics. From Bohr's view, a heavy particle with a charge ze, mass M and velocity v passing through a material is considered supposing that there is an atomic electron at a distance b from the particle trajectory. To perform this calculation three important assumptions have been done: firstly, it is assumed that the electron is free and initially at rest (i.e. its orbital velocity must be much lower than the ion velocity). Secondly, it is assumed that the electron only moves very slightly during the interaction with the heavy particle so that the electric field acting on it may be taken at its initial position. Eventually, it is supposed that the incident particle remains essentially undeviated from its original path because of its much larger mass $M \gg m_e$. Once summing up all contributions from atomic electrons by integrating over the impact parameter b, it is possible to write a expression for the specific energy loss [2]:

$$-\frac{\mathrm{d}E}{\mathrm{d}x} = \frac{4\pi z^2 e^4}{m_e v^2} N_e \ln \frac{\gamma^2 m_e v^3}{z e^2 \bar{\nu}} \tag{1.2}$$

where $\bar{\nu}$ is the mean orbital frequency of atomic electrons, γ is the Lorentz factor of the incident particle and N_e is the density of electrons. This formula gives a reasonable description of the energy loss for heavy particles such as the α particle or heavier nuclei. However, for lighter particles, like protons, the formula breaks down because of quantum effects.

The correct quantum-mechanical calculation was first performed by Bethe, Bloch and others. In the calculation the energy transfer is parametrized in terms of momentum transfer rather than the impact parameter. The Bethe-Bloch formula can be written as [2]:

$$-\left\langle \frac{\mathrm{d}E}{\mathrm{d}x} \right\rangle = \frac{2\pi N_a e^4 \rho}{m_e} \frac{Z}{A} \frac{z^2}{v^2} \left[\ln\left(\frac{2 m_e \gamma^2 v^2 W_{\max}}{I^2} \right) - 2\beta^2 - \delta - 2\frac{C}{Z} \right]. \tag{1.3}$$

with

m_e = electron mass
e = electron charge
N_a = Avogadro's number
Z = atomic number of the medium
A = atomic weight of the medium
ρ = density of the medium
z = charge of the incident particle
v = velocity of the incident particle
$\beta = v/c$
$W_{\max}$ = maximum energy transfer in a single collision
I = mean excitation potential
δ = density correction
C = shell correction.

The Eq. 1.3 is valid if $0.05 < \beta\gamma < 500$ and for particles heavier or equal than the muon ($m_\mu \simeq 106\,\mathrm{MeV}/c^2$). The mean excitation potential, I, is one of the parameters of the Bethe-Bloch formula and it is essentially $h\bar{\nu}$ where $\bar{\nu}$ is the average orbital frequency from Bohr's formula and h the Planck's constant; it is theoretically a logarithmic average of ν weighted by the oscillator strengths of the atomic levels [2]. The standard value for water (very similar to the composition of the average human body) is $I \simeq 75\,\mathrm{eV}$ but slightly larger values can be found in literature. Regarding other materials, in a first approximation the value of the mean excitation potential is given by:

$$I \approx 11.5 \cdot Z\,\mathrm{eV}. \tag{1.4}$$

The main feature of the incident particle for the energy loss rate is the dependence on $1/\beta^2$ and on the square of the particle charge. This means that the energy loss rate shows

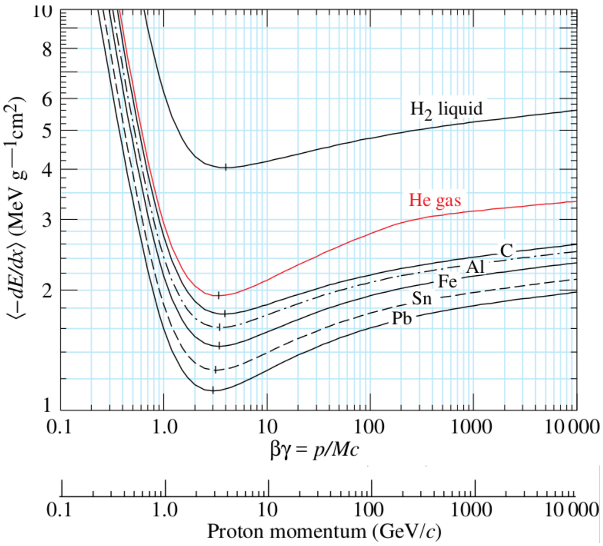

Figure 1.1: Mass stopping power versus $\beta\gamma$ for particles with $z = 1$ in different materials[a]. The proton momentum axis is also reported [4].

a fast increase as the particle slows down. Furthermore, the expression is not dependent on particle mass.

Also the absorber plays a role since the energy loss is proportional to the density of the electrons in the material ($N_a \rho Z/A$). The Z/A term for standard materials ranges from 0.5 for biological elements to 0.42 for some high-Z materials. Since the mean excitation potential I is inside a logarithm and other absorber terms have a limited variability, the density ρ is the most critical term as, for instance in the hadrontherapy field, can vary of three orders of magnitude between air in the lung and cortical bone [3]. In order not to depend too much on the density, it is useful to introduce the *mass stopping power* of a material, defined as:

$$\frac{\mathrm{d}E}{\mathrm{d}\chi} \equiv \frac{1}{\rho}\frac{\mathrm{d}E}{\mathrm{d}x} \tag{1.5}$$

where $\chi = \rho x$ is the mass thickness of the material in units of g/cm^2. This is a handy quantity since it is more related to the interaction centres and it can be also considered as a normalisation among different materials. Indeed, equal mass thicknesses of different materials have almost the same effect on the same radiation since the density is the leading term of Bethe-Bloch on the absorber side. Bethe-Bloch curves are shown in Fig. 1.1.

---

[a] $\beta\gamma$ is a handy quantity for this kind of plots since it allows to represent all particles with the same charge with a unique curve for a given material. Indeed, $\beta\gamma = p/m_0c^2 = \sqrt{\epsilon(\epsilon+2)}$ where p and m_0 are the particle momentum and mass and $\epsilon = E_k/m_0c^2$.

1.1.2 Other effects

The Bethe-Bloch formula has several corrections, both at low and high velocities. At low velocities (for light ions below 10 MeV/u) the charge of the particle (z in Eq. 1.3) decreases due to ionization and recombination processes and it has to be replaced with an effective charge z_{eff} which can be modeled as:

$$z_{\text{eff}} = z(1 - \exp(-125 \cdot \beta z^{-2/3})). \tag{1.6}$$

Still at low velocities there is another effect to take into account which is embedded in the Eq. 1.3, the *shell effect* [5]. This is due to the Pauli exclusion principle, stating that the only possible arrangements of electrons in a molecule or atom are those in which no electron has the same set of quantum number of another one. For an absorber with atomic number Z the shell correction term

$$U = 2\left(\frac{C}{Z}\right)$$

where $C = C(I, \beta\gamma)$ takes into account that electrons lying in inner shells do not participate in the collision process [2].

At higher energies, i.e. higher velocities, the energy-loss $\mathrm{d}E/\mathrm{d}x$ decreases swiftly following the $1/\beta^2$ term up to a minimum located at $\beta_{\min}\gamma_{\min} \approx 3 \Rightarrow \beta_{\min} \approx 0.95$. A particle satisfying this relation is called a *minimum ionizing particle* (mip). The energy-loss starts to increase again beyond this broad minimum thanks to the logarithmic term in Eq. 1.3. This is due to the increase of both the momentum and $W_{\max}$: in principle, the electric field of the particle is felt also by electrons in farther atoms so that the latter contribute more and more to the energy-loss. Nevertheless, the slope of this rise is controlled by the *density effect*: as a consequence of increased electric field, the atoms close to the path of the particle start to polarize resulting in a reduction of the force exerted on far electrons. This effect is stronger for dense material with respect to lighter materials such as gases.

1.2 Range and energy loss fluctuations

The particular behaviour of heavy charged particle in matter allows to define a *range*. For practical purposes, this quantity can be defined in different ways. A smart way to do so is to integrate the Bethe-Bloch formula so that

$$R = \int_0^{E_{K_i}} \frac{dE}{-dE/dx}, \tag{1.7}$$

where E_{K_i} is the initial energy of the particle. This equation neglects the effect of Multiple Scattering, which will be treated in next section, but it provides a good approximation for heavy ions.

At energies of our interest, relativistic effects are not so important and the energy loss in Eq. 1.3 becomes [5]:

$$-\frac{\mathrm{d}E}{\mathrm{d}x} \approx 2\pi e^4 \rho N \frac{Z}{A}\frac{z_p^2}{E_K}\frac{m_p}{m_e}\ln\left(\frac{2m_e v^2}{I}\right) = 0.0784\rho N \frac{Z}{A}\frac{z_p^2}{E_K}\frac{m_p}{m_e}\ln\left(\frac{2m_e v^2}{I}\right) \tag{1.8}$$

where $E_K = m_p v^2/2$ is the kinetic energy of the incident particle. Using this form it is possible to solve the previous formula as

$$R_{m_p} = \frac{m_e m_p}{0.1568\rho N \frac{Z}{A} z_p^2}\int_0^{v_i}\frac{v^3 \mathrm{d}v}{\ln\left(\frac{2m_e v^2}{I}\right)} \propto \frac{m_p}{z_p^2} f(v_i), \tag{1.9}$$

where v_i is the initial velocity of the particle. In the last formula it was assumed that the dependence in the integral on I can be neglected. Eq. 1.9 suggests a scaling law: if one knows the range of a particle with mass m_p and charge number z_p it is possible to get the range of another particle with mass m_x and charge number z_x with the same kinetic energy per nucleon such that the velocities are the same so that $f(v_{i,p}) = f(v_{i,x})$. Namely, the following relation holds:

$$R_{m_x} \approx \frac{m_x}{m_p}\frac{z_p^2}{z_x^2} R_{m_p}. \tag{1.10}$$

This relation will be of great importance in next chapters.

Combining Eq. 1.8 and Eq. 1.7 without substituting E_K it is possible to note that $R \propto E_K^2$ even if fits with different data suggest a different behaviour $R \propto E_K^{1.75-1.8}$. For instance, regarding protons in air with standard temperature and pressure conditions, the following equation holds:

$$R_{p,\mathrm{air}} = 10^2 \cdot \left(\frac{E_K}{9.3}\right)^{1.8} \quad [\mathrm{cm}] \tag{1.11}$$

where E_K is in MeV [6]. A plot of the proton range in air versus its kinetic energy using the Continuous Slowing Down Approximation (CSDA) is reported in Fig. 1.2.

A set of identical particles with the same initial velocity do not stop at the same depth, even if the energy loss process is continuous. Fluctuations in path length of particles are present due to the statistical nature of the collision process. This phenomenon is called *range straggling* and it is due to the fluctuations in the energy-loss. They are described by the Vavilov distribution which can be approximated to a Gaussian distribution in the limit of many collisions (i.e. in thick absorbers) as stated by the central limit theorem [8]:

$$f(\Delta E) = \frac{1}{\sqrt{2\pi\sigma_{\Delta E}^2}}\exp\left(\frac{(\Delta E - \overline{\Delta E})^2}{-2\sigma_{\Delta E}^2}\right) \tag{1.12}$$

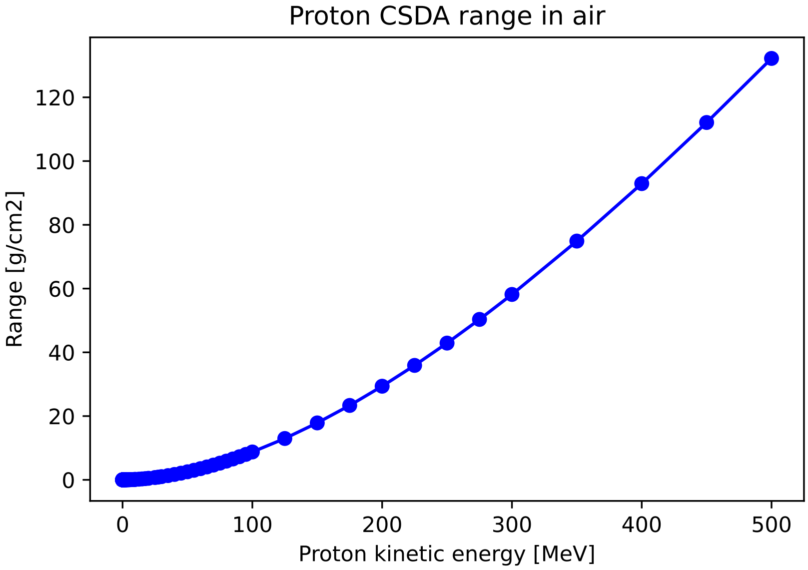

Figure 1.2: CSDA range of protons in air from PSTAR tables [7].

where $\sigma^2_{\Delta E} = 4\pi z^2 e^4 N x \left(\frac{1-\beta^2/2}{1-\beta^2}\right)$ with $N = \rho N_a Z/A$ is the density of the atoms in the absorber [9].

The energy straggling σ_R is directly related to the energy straggling by the equation [10]:

$$\sigma^2_R = \int_0^{E_{K_i}} \left(\frac{\mathrm{d}\sigma^2_{\Delta E}}{\mathrm{d}x}\right)\left(\frac{\mathrm{d}E}{\mathrm{d}x}\right)^{-3} \mathrm{d}E. \tag{1.13}$$

It turns out that the relative range straggling is almost constant and it can be written as [11]:

$$\frac{\sigma_R}{R} = \frac{1}{\sqrt{m}} f\left(\frac{E}{mc^2}\right). \tag{1.14}$$

where f is a slowly varying function. Also in this case it is possible to find a scaling law for different particles with the same range:

$$\frac{\sigma_{R1}}{\sigma_{R2}} \approx \sqrt{\frac{m_2}{m_1}}. \tag{1.15}$$

1.3 Multiple Coulomb Scattering

As already pointed out, a charged particle traversing a medium is affected by Coulomb field of electrons and nuclei. Unlike the energy loss discussed so far, the multiple scattering processes are dominated by deflections due to the electric fields of nuclei [12].

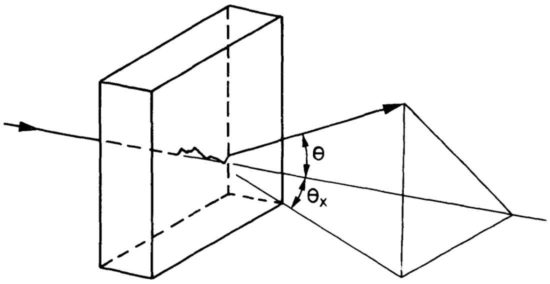

Figure 1.3: Multiple scattering of a charged particle in a medium. Here, θ_x is the projected scattering angle [2].

These lead to several elastic scattering events whose net effect is to deflect incident particles from the initial direction (Fig. 1.3). The distribution of scattering angles due to the Multiple Coulomb Scattering is described by the Molière's theory using several functions related to Bessel functions of the first kind [13]. In the first-order approximation the projected scattering angle distribution becomes a Gaussian distribution with a root mean square given by:

$$\sigma_\theta^{\text{proj}} = \frac{13.6\,\text{MeV}}{\beta c p} z \sqrt{\frac{x}{X_0}} \left[1 + 0.038 \ln \frac{x}{X_0}\right] \tag{1.16}$$

where p is the momentum of the particle in MeV/c, βc and z are its velocity and charge respectively and x/X_0 is the thickness of the traversed medium in units of radiation length, i.e.

$$X_0 = \frac{A}{4\alpha N_a Z^2 r_e^2 \ln\left(183\, Z^{-1/3}\right)} \tag{1.17}$$

where Z and A refer to the scattering medium and α is the fine-structure constant.

The former equation gives the projected distribution of the scattering angles: if one is interested in the non-projected distribution the formula has to be multiplied by $\sqrt{2}$:

$$\sigma_\theta^{\text{space}} \approx \frac{19.2\,\text{MeV}}{\beta c p} z \sqrt{\frac{x}{X_0}}. \tag{1.18}$$

The discussion above does not take into account the non-Gaussian tails of the distribution observed in data: these are caused by both single large angle scattering events and nuclear interactions which do not fit into a single Gaussian so that a most complex approach is needed as shown in Fig. 1.4. A detailed review of these kinds of parametrisations are described in [14, 15].

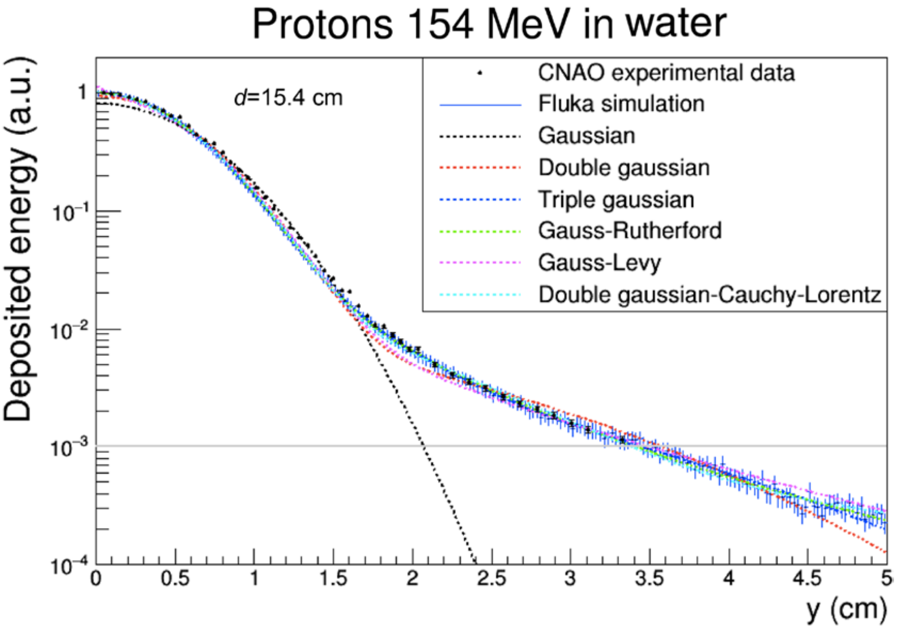

Figure 1.4: Lateral dose profile of 154.25 MeV protons at 15.4 cm depth in water [14].

1.4 Nuclear interactions

Up to now only electromagnetic interactions, i.e. inelastic collisions between the charged particle and the electrons of the absorber or elastic scattering with nuclei, were considered. However, the role of nuclear interactions cannot be neglected since they turn to be really relevant both from a clinical and radioprotection standpoint. The energy range we are interested in is quite high for nuclear physics and some assumptions, not valid at lower energies, can be made.

All nucleus-nucleus collision models use a two-step process, the so-called *abrasion-ablation* model, which was introduced in [17]. This model starts from a simple description: when two ions (projectile and target in the following) pass each other so close that a part of their volumes overlaps, some overlapping nucleons can be teared away (i.e. abrasion). These nucleons form a hot reaction zone, the fireball, while other nucleons are not affected by the interaction. The remaining part of the projectile continues its path nearly with the same velocity but, after abrasion, it is left in an excited state and it will lose energy by emitting one or several particles (i.e. ablation). The same occurs for target fragments as well as the fireball whose de-excitations generate nucleons and light clusters. In this framework, sketched in Fig. 1.5, peripheral collisions are more frequent so that the number of overlapping nucleons remains small. However, occasionally central collisions occur resulting in a total breakup of the two nuclei.

When two nuclei interact two different processes can occur: in the case of a *elastic* process the total kinetic energy is conserved and nuclei before and after the interaction

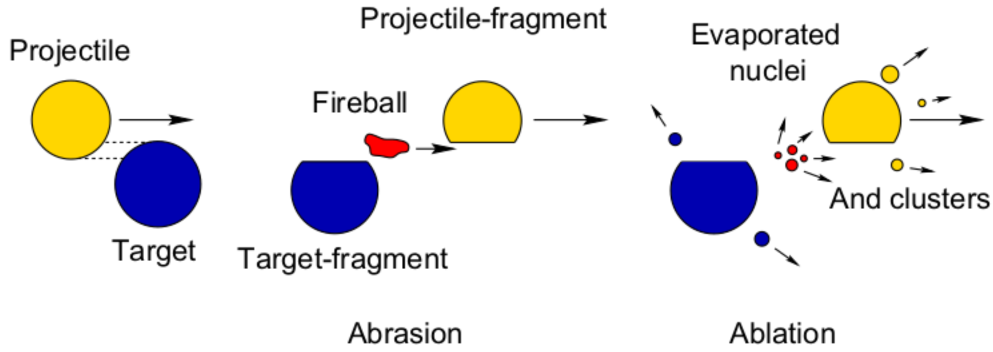

Figure 1.5: A drawing of the abrasion-ablation model [16].

are the same. On the other hand, in an *inelastic* interaction the total kinetic energy is not conserved. However, it is possible for nuclei both to fragment or to stay intact before de-exciting usually by γ ray emission. In the former case, final nuclei differ from initial nuclei. The first observable we are interested in is the *total reaction cross section* which is defined as the total minus the elastic cross section:

$$\sigma_R = \sigma_{\text{tot}} - \sigma_{\text{el}} \tag{1.19}$$

Using a geometrical approximation, which turns to be satisfying in a high-energy regime ($> 1.5\,\text{GeV/u}$), the nucleus can be modeled as a sphere according to the liquid drop nuclear model so that σ_R can be written as the overlapping area between the projectile and the target, namely $\sigma_R \propto (A_p^{1/3} + A_t^{1/3})^2$, where A_p (A_t) is the mass number of projectile (target) [18].

The first empirical expression is due to Bradt and Peters [19]:

$$\sigma_R = \pi r_0^2 (A_p^{1/3} + A_t^{1/3} - b)^2 \tag{1.20}$$

where $R_0 \approx 1.2\,\text{fm}$ is the nucleon radius and b is the overlap transparency parameter. In Eq. 1.20, all terms are energy-independent: however, it fails to tailor to lower energy data. Hence, several parametrisations were proposed: among them, the one proposed in [20] is used also in Monte Carlo and radiation transport codes:

$$\sigma_R = \pi r_0^2 c_1(E) \left(A_p^{1/3} + A_t^{1/3} - c_2(E) \right)^2 \tag{1.21}$$

where c_1, c_2 are energy-dependent. These empirical models were refined using intense experimental campaigns in order to find parameters which describe best the interaction at lower energies ($< 1\,\text{GeV/u}$) in which Coulomb interactions becomes important [21]. The optimization of total reaction cross sections involving some particular target-projectile combinations is still under investigation [22].

Most approaches for cross sections measurement are based on the attenuation of the primary beam: the probability for an incident particle to survive after traveling a distance x in a material is given by:

$$P(x) = \frac{N(x)}{N(0)} = \exp(-x/\lambda_{\text{int}}), \tag{1.22}$$

where $N(0)$ is the number of incident particles, $N(x)$ the number of incident particles survived after a distance x and λ_{int} is the mean free path or the interaction length, i.e. $\lambda_{\text{int}} = A_t/(N_a \sigma_R \rho)$ where σ_R is the total reaction cross section.

Nevertheless, most complete approaches involve measurements of the production of a particular fragment (e.g. *exclusive* cross sections) or even measurements of the so called *double differential cross sections* which take into account also other parameters, such as the kinetic energy and the scattering angle of a produced fragment as a result of the interaction. For instance, the double differential cross section in both kinetic energy and angle can be used to write the total reaction cross section:

$$\sigma_R = \int_0^{\Omega} \int_0^{\infty} \frac{d^2\sigma}{dE_K d\Omega} dE_K d\Omega. \tag{1.23}$$

This latter approach is very important since it can constrain Monte Carlo simulations which currently show large discrepancies when different nuclear models are used within the same code [23] or among different Monte Carlo codes [24]. Such measurements are considered one of the main contribution that nuclear physics can bring to the future of charged particle therapy against tumours [25] and in space radioprotection field [26].

Chapter 2

Motivations for Hadrontherapy

Cancer is a group of diseases characterized by the uncontrolled growth and spread of abnormal cells. If the spread is not controlled, it can result in death. Although the causes for many cancers, particularly the ones occurring during childhood, remain unknown, established cancer causes include lifestyle (external) factors, such as tobacco use, physical inactivity, exposure to air pollution and excessive body weight. Other internal factors, such as inherited genetic mutations, hormones, and immune conditions are included among cancer causes. These risk factors may act simultaneously or in sequence to initiate and/or promote cancer growth. Several years may often pass between exposure to external factors and cancer occurrence.

According to the *World Health Organization* WHO Media Centre [27], cancer is a leading cause of death worldwide, accounting for 10 million deaths in 2020; the most common deathly cancer are cancers of lung, liver, colorectal, stomach and breast: however, $30 - 50\%$ of cancers could currently be prevented by avoiding risk factors and implementing existing evidence-based prevention strategies. The cancer burden can also be reduced through early detection of cancer and management of patients. These risk factors combined with the growth and ageing of population and with delays in tumour treatment and prevention due to COVID-19, will lead to a increase of cancer incidence and deaths in the next years.

However, it seems to be a decreasing tendency in some cancer death rates: according to National Institutes of Health SEER program [28], the female breast cancer death rate in the US declined by nearly 40% in 1992-2018 due to improvements in early detection and treatment. Lung and bronchus cancers confirm themselves as the most lethal cancers in the US although they had a steep decrease over the last 30 years; however, pancreatic and liver cancers are slightly increasing both in males and females.

The overall improvement in the survival rate is due to both progress in early diagnosis technique and healing technology breakthroughs. Nowadays there are several ways to treat solid tumours: the most known are surgery, chemotherapy, *radiation therapy* (RT) and immunotherapy. All these techniques can be used alone or combined with each other while recent estimates indicate that approximately 50% of all cancer patients could benefit from RT in the management of their disease, both with curative and palliative purpose [29].

The roots of RT were established between the 19^{th} and 20^{th} century: the main discovery was in 1895 when Röntgen produced X-rays from a vacuum pipe. His report was followed soon by Becquerel's on the phenomenon of radioactivity and, in 1898, by that of Pierre Curie and Marie Sklodowska Curie on the discovery of radium. Becquerel and Curie reported on the physiologic effects of radium rays in 1901 and since then, such discoveries stimulated speculation that radioactivity could be used to treat disease. Indeed, X-rays were used to treat a patient with breast cancer for the first time in January 1896: these pioneering treatments marked the beginning of RT [30]. Unfortunately, a big issue arose soon: to have an efficient treatment of cancers it is mandatory to deliver radiation only to the tumour mass sparing normal tissues as much as possible.

After a brief history, charged particle therapy will be presented using all the physics developed in Chap. 1.

2.1 History and state of the art

The first application of accelerators in medicine was in 1931, when Ernest Lawrence and Stan Livingston built the first cyclotron. Ernest and his brother John irradiated patients with salivary glands cancer by means of neutron beams produced by 5 MeV accelerated deutons on a beryllium target. As these neutrons produce nuclear fragments, these treatments can be regarded as the first use of hadrons to cure cancers ever.

The groundwork for hadrontherapy (also called Charged Particle Therapy, CPT) was laid in 1946 when Robert R. Wilson wrote the landmark paper [31] in which he proposed that protons accelerated by machines such as Lawrence's could be used for medical purposes as well as scientific investigations. The first clinical use of a proton beam occurred at Berkeley, California in 1954; after a few years Berkeley scientists, notably Cornelius A. Tobias, began investigating biologically damage produced by Helium ions. Their fundamental research interest was on the effects of ionizing radiation on living cells.

Proton Therapy (PT) began to spread to other physics laboratories around the world. The second use of a physics research accelerator for PT occurred in Uppsala (Sweden) in 1957, while in 1967 beam therapy began at Dubna, USSR. The Japanese experience began in 1979, at Chiba and another facility opened at Tsukuba in 1983. At the Swiss Institute for Nuclear Research (now the Paul Scherrer Institute, PSI), PT began in 1985. The first hospital-based proton facility in the world opened at the Loma Linda University Medical Center (LLUMC) in California and it began to treat patients in 1990 after twenty years of development. In those years, the use of several ion beams (such as

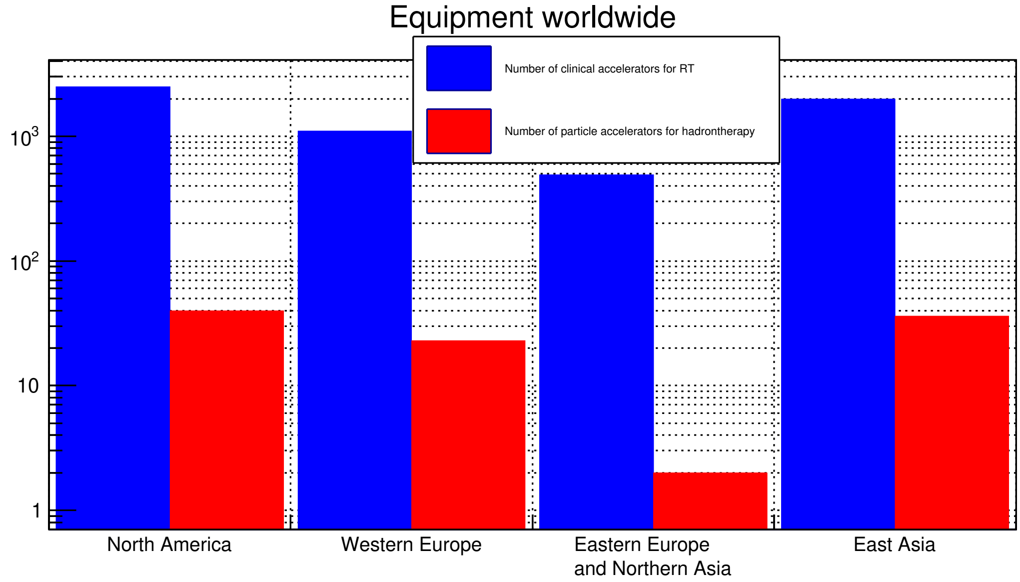

Figure 2.1: Number of RT centres worldwide divided by equipment type [33].

Helium, Argon, Neon and Silicon) and pion beams was investigated to improve clinical results: unfortunately excessive toxicity was observed in patients, especially due to the high dose in the entrance channel of high Z beams. Today proton and Carbon ions are used in clinical practice while other interesting ions, such as Helium and Oxygen, are going to be used in the next years.

From 1997 to 2008, a Carbon ion therapy unit for tumours at the base of the skull operated at GSI in Darmstadt, Germany. The success of this project laid the groundwork for the construction of the first heavy ion therapy center in Europe, at Heidelberg University. In Italy, the first operating hadrontherapy unit was set in 2002 at LNS (Laboratori Nazionali del Sud, INFN) for the treatment of ocular melanoma with protons. The first clinical facility, CNAO (Centro Nazionale di Adroterapia Oncologica), was set in Pavia and treatments began in 2011, both with protons and Carbon ions. Eventually, in 2014 another proton therapy centre, Centro di Protonterapia, started to treat patients in Trento.

Up to the end of 2020, in the world almost 250000 patients have been treated with protons while more than 39000 with carbon or other ions. As of 2020, there are 103 facilities treating with protons or carbon ions worldwide (Austria, Canada, Czech Republic, China, Denmark, France, Germany, Italy, Japan, Netherlands, Poland, Russia, South Africa, South Korea, Spain, Sweden, Switzerland, United Kingdom, USA) and other 37 facilities are under construction, also in other countries (Argentina, Australia, Norway, Slovakia) [32]. As it can be seen in figure 2.1, hadrontherapy accounts only for a small

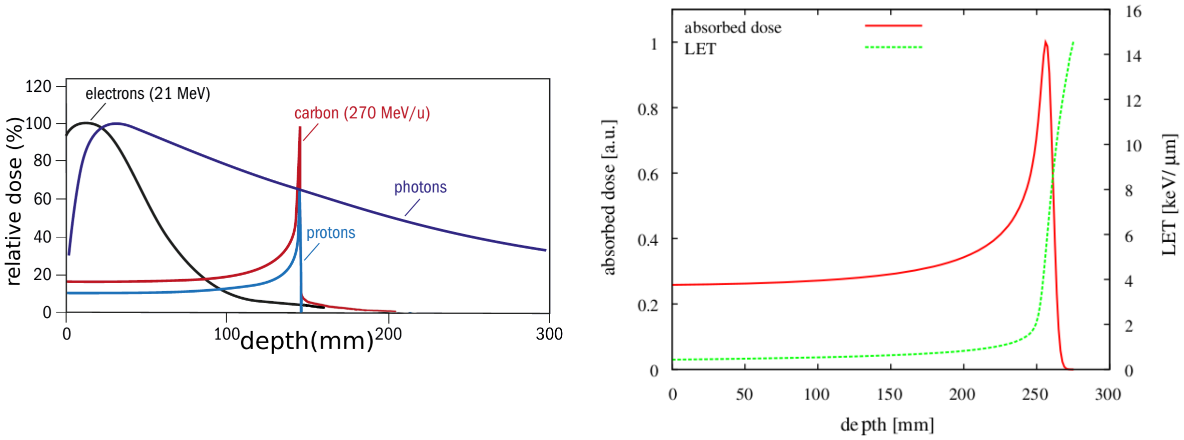

Figure 2.2: Dose-depth distribution for electrons, photons, protons and carbon ions for therapeutic purpose, adapted from [34] (left). Depth dose curve in water and corresponding dose-averaged linear energy transfer (LET) for a proton beam with an initial energy of 200 MeV [35] (right).

number of all external radiation therapy treatments [33].

2.2 The Bragg peak

The main advantage to use charged particles to treat tumours is their favourable depth-dose profile which is very different from that of photons. Indeed, while a photon beam reduces its intensity exponentially as it enters into a material, charged particles are characterised by a low energy release in the beginning followed by a sharp rise after which the particle stops (see Fig. 2.2, left).

This is due to the $1/\beta^2$ behaviour of Bethe-Bloch formula in Eq. 1.3: when the particle is fast, its mean energy loss is low so that its energy does not change so much for unit path length but the slower the particle the higher the energy loss is. This results in a sharp rise in depth-dose profile in which the particle loses all its energy: as shown in Fig. 2.2 right, this swift rise is driven by the rise of $\mathrm{d}E/\mathrm{d}x$. Moreover, the position of the Bragg peak is fully determined by the kinetic energy of the incident particle.

This peculiar behaviour makes charged particle suitable for the treatment of deep-seated solid tumours, in particular those close to Organs At Risk (OAR). These are organs, like the optical nerve or the spinal cord for instance, which are very sensitive to radiation: in the treatment planning stage it is mandatory not to exceed some dose values for such organs since it could increase the probability of side effects.

The depth-dose curve in Fig. 2.2 is called *Bragg curve* and its sharp maximum is called *Bragg peak*. They are named after W.H.Bragg's studies on the energy loss of α

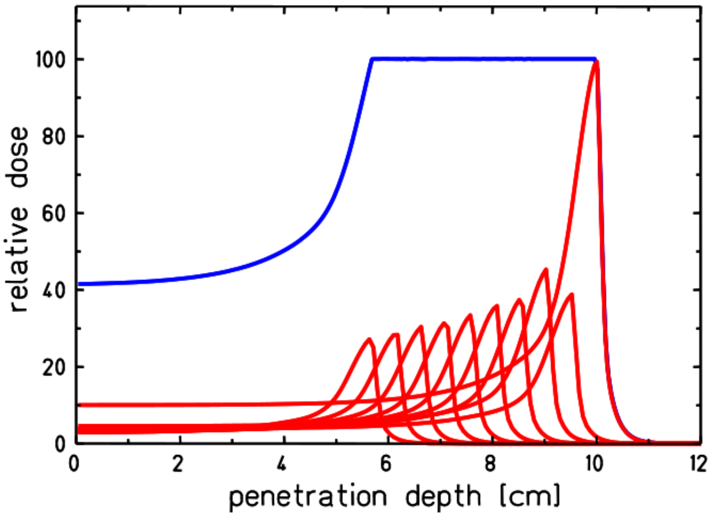

Figure 2.3: Multiple pristine Bragg peaks can be overlapped to achieve a quasi-uniform dose in the tumour (Spread Out Bragg Peak, SOBP) [25].

particles in different materials in the early 1900s.

Thanks to the aforementioned properties, charged particles have a very narrow peak: for instance, the range of 270 MeV/u ^{12}C ions in human body is almost 14 cm and the Bragg peak FWHM is $\approx$ 5 mm. However, tumours can be much larger so that many Bragg peaks have to be overlapped in order to cover all the cancer volume. The resulting curve is called Spread Out Bragg Peak (SOBP) and it is reported in Fig. 2.3. Nowadays in clinical practice, hadrontherapy can be used in all pediatric tumours, skull and spinal cancers, liver and pancreatic cancers, to mention a few. Generally, charged particles are used in all scenarios in which it is possible to harness their unique physical features, notably their finite range in the patient.

2.3 Range and straggling

As pointed out in Sec. 1.2, the range of charged particles depends on kinetic energy: this means that it is possible to tune the Bragg peak depth by changing the energy of incident ions. This can be achieved by an active energy selection in synchrotrons and by a passive energy degradation in cyclotrons. The state of the art in particle therapy is the use of active scanning technique: the tumour is divided in *voxels* and it is 3D-"painted" by the beam by using fast sweeping magnets to cover the transversal area and different energies to reach different depths. In the past, passive beam scattering with compensation and modulation was widely used, however the dose conformation to the tumour was poorer, resulting in a higher dose in healthy tissues.

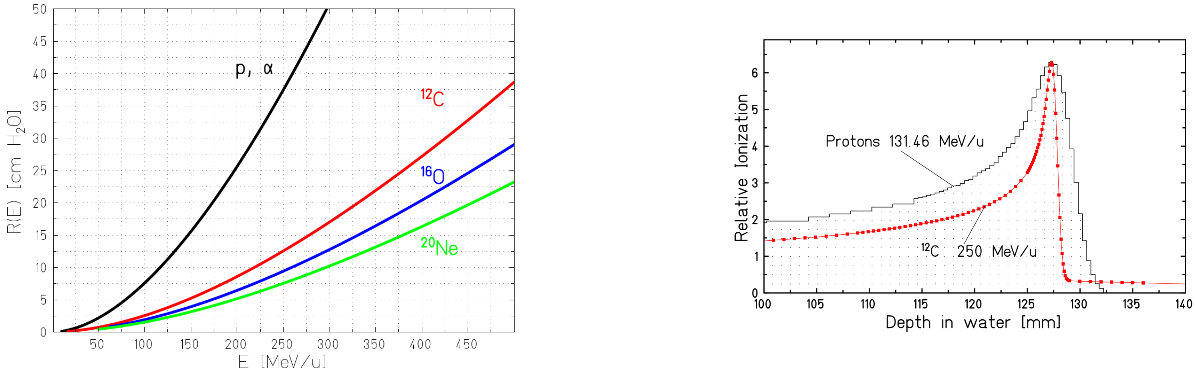

Figure 2.4: Mean range of ions in water (left). Measured Bragg peaks of protons and ^{12}C ions having the same mean range in water [36] (right).

The particle acceleration to therapeutic energies requires huge machines, especially when heavy ions, such as Carbon, are involved. This is also due to higher energy necessary to treat deep tumours: as shown in Fig. 2.4 left, while a 150 MeV proton beam has a range of $\approx 15\,\mathrm{cm}$ in water, a 150 MeV/u Carbon ion beam (i.e. with the same velocity) has a range of $\approx 5\,\mathrm{cm}$, three times lower. This ratio agrees with the scaling law reported in Eq. 1.10, namely:

$$\frac{R_{\text{proton}}}{R_{\text{Carbon}}} \approx \frac{m_{\text{proton}}}{m_{\text{Carbon}}} \frac{z^2_{\text{Carbon}}}{z^2_{\text{proton}}} \approx 3 \tag{2.1}$$

The range calculation is of great importance in charged particle therapy: the very sharp dose-depth profile is the main physical advantage of charged particle but the impact of a wrong range calculation can be dramatically important from a clinical standpoint. Indeed, a shift in the Bragg peak has a much larger impact on the dose than for photons so that range uncertainty is one of the major issues to cope with nowadays.

Another important aspect for charged particle therapy is the range straggling: as set out in Sec. 1.2, the statistical fluctuations in energy-loss result in a fluctuation in the range of primary particles. From Eq. 1.14 it is possible to notice that the relative range straggling has a $1/\sqrt{m}$ dependence so that the Bragg peak is sharper for particles of higher mass. The scaling law reported in Eq. 1.15 shows that the straggling of a proton beam is ≈ 3.5 times that of a ^{12}C beam with the same range in water (Fig. 2.4).

For this reason, and for the impact of elastic scattering which will be treated in the next section, Carbon ions are characterised by a sharper energy deposition which should always result in a better treatment. However, as explained later, some issues arise from projectile fragments due to nuclear interactions resulting in a change of depth-dose profile which is to be taken into account in clinical practice.

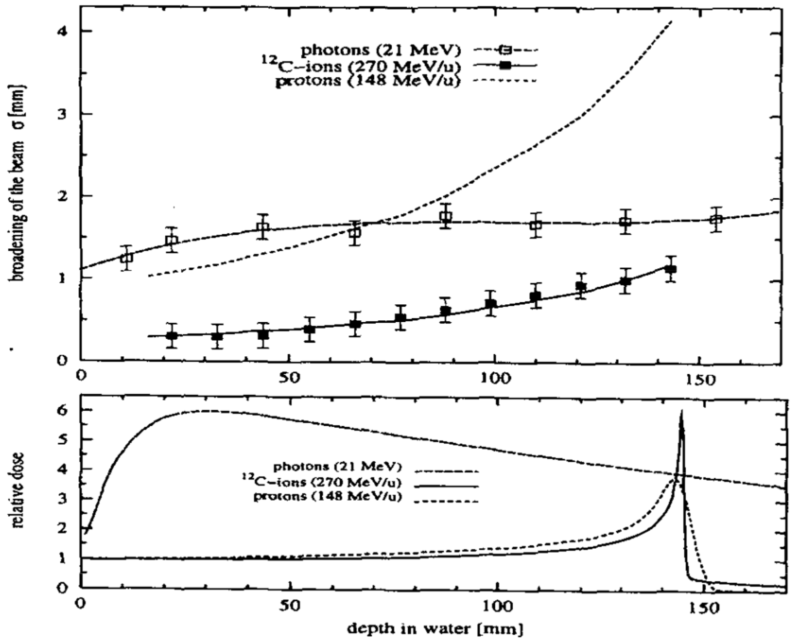

Figure 2.5: Comparison of the lateral scattering of photon, proton and Carbon beams as function of the penetration depth (top) and the depth dose correlation (bottom) in standard clinical settings [37].

2.4 Multiple Scattering

A beam of charged particles tends to spread in a medium, mainly due to Coulomb interactions with interacting nuclei. In Eq. 1.16 it can be noticed that the term βcp is the most important when dealing with different beams in hadrontherapy. Indeed, if one takes the lateral scattering of a proton beam and of a Carbon beam with the same range, as in Fig. 2.5, it is possible to calculate the ratio between the two lateral scattering simplifying the radiation length term. It results that the proton beam is up to four times larger than the Carbon one, except for the very last centimeters in which the contribution of nuclear reactions leads to a further increase.

Since the dose release of a Carbon ion beam is sharper than that of protons also in the longitudinal direction, this means that heavy ions should be more precise both in orthogonal and longitudinal direction with respect to the beam. This could result in a better dose conformation to the tumour but it can also make treatment plans less robust to misalignments or uncertainties.

In a typical clinical configuration, the beam spread in water for Carbon ions is always less than 1 cm while for protons could be more than 2 cm, especially in the treatment of shallow tumours in facilities with passive energy degraders for energy modulation.

2.5 Nuclear fragmentation

The potential drawback to deal with in treatments with heavy charged particles is nuclear fragmentation. In a hadrontherapy treatment, both the projectile and the target can undergo a fragmentation but their descriptions are quite different as their effects. For this reason they will be treated separately.

2.5.1 Nuclear fragmentation of the projectile

Nuclear interactions are far less frequent than inelastic collisions with atomic electrons. Nevertheless, their importance grows at large penetration depths because of the total number of interactions which can greatly modify the Bragg curve. This does not hold for protons since they do not fragment at therapeutic energies ($E_K < 250\,\mathrm{MeV}$) In particular, nuclear fragmentations result in a buildup of lower mass fragments, mainly of lower-Z fragments. This effect is not negligible as, for a 400 MeV/u ^{12}C in water, only 30% of primary ions reaches the Bragg peak placed at nearly 28 cm. Moreover, according to the dynamic of reaction, most of the fragments will travel nearly at the same velocity of the primary ion since peripheral collisions are more frequent so that the number of participating nucleons remains small. This assumption allows us to recall the Eq. 1.10 in which now the incident particle p is the primary ion while the particle x is a fragment of a projectile. If a ^{12}C ion fragments into a ^{11}C, Eq. 1.10 will give:

$$R_{^{11}\mathrm{C}} \approx \frac{11}{12} R_{^{12}\mathrm{C}} \tag{2.2}$$

indicating that a lower mass isotope of the primary ion will have a shorter range with respect to the latter. However, when lower-Z fragments are created, their range will be always longer than that of the primary ion. For instance, if a ^{4}He fragment is created:

$$R_{^{4}\mathrm{He}} \approx \frac{4}{12}\frac{36}{4} R_{^{12}\mathrm{C}} \approx 3 R_{^{12}\mathrm{C}}. \tag{2.3}$$

Since nuclear fragmentations can occur along the whole path of the primary beam, this results in a non-zero dose beyond the Bragg peak, the so-called *fragmentation tail.* Generally, as the particle p is fixed by the beam, we can say that the range of a fragment X scales as the following:

$$R_{X_Z^A} \propto \frac{A}{Z^2}. \tag{2.4}$$

A detailed Monte Carlo simulation able to describe the measured Bragg curve of a 200 MeV/u ^{12}C ion beam in water is reported in Fig. 2.6, top. As already pointed out, Carbon isotopes have a shorter range than that of the primary beam while lower-Z fragments stop after the Bragg peak.

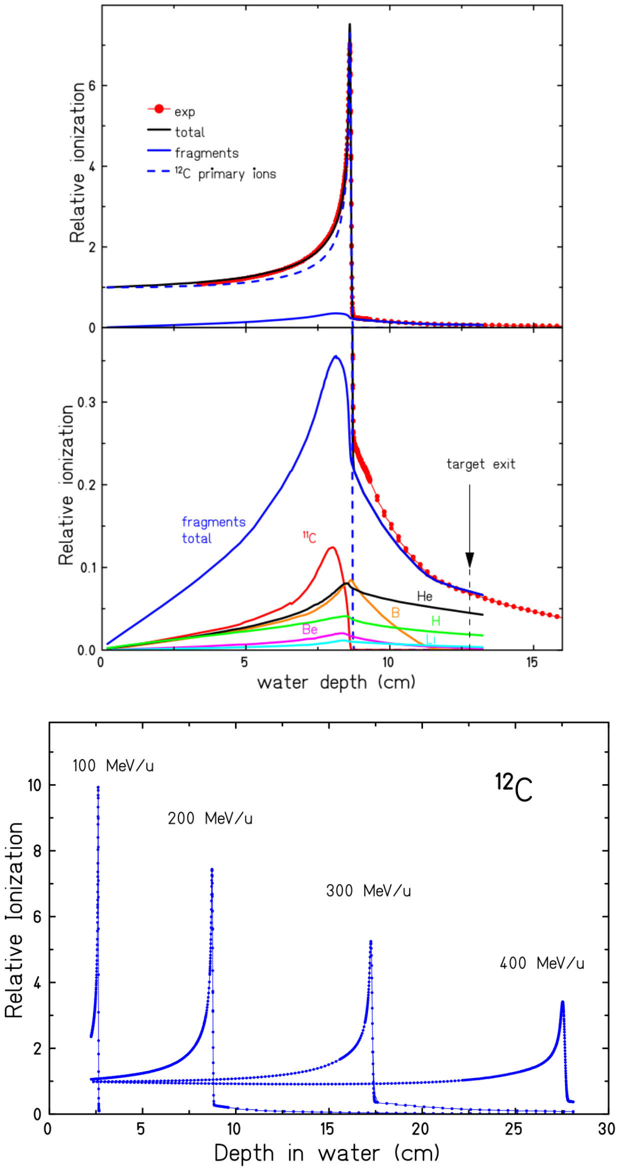

Figure 2.6: Measured Bragg curve for a 200 MeV/u ^{12}C ion beam in water. The lower part is magnified to show the contribution of projectile fragments with PHITS simulation (top) [16]. Measured Bragg curves of ^{12}C ions stopping in water [36] (bottom).

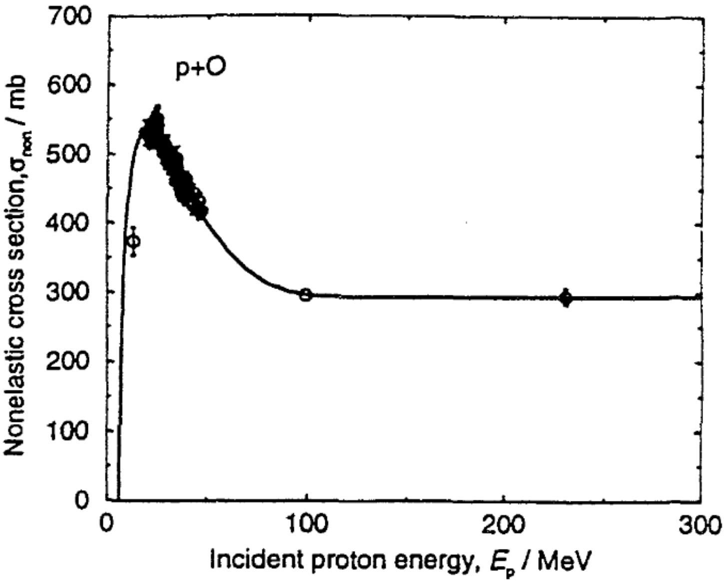

Figure 2.7: Evaluated total nonelastic cross sections for protons incident on Oxygen [38]. Data from [39].

The nuclear fragmentation effect increases with increasing depths and it leads to important changes to the Bragg curve. In Fig. 2.6, bottom, some measured Bragg curves for Carbon are reported: it can be noticed that at larger depths the peak-to-plateau ratio decreases while the tail becomes more and more important. Moreover, the Bragg peak is broadened by the straggling (see Eq. 1.14).

2.5.2 Nuclear fragmentation of the target

In a nuclear interaction both the projectile and the target can fragment. Even if the fragmentation of the projectile has a large impact on the Bragg curve, target fragmentation can assume a important role too, especially in proton therapy in which protons cannot fragment. Indeed, at these energies ($E_K < 290\,\mathrm{MeV}$, $p \approx 790\,\mathrm{MeV/c}$ in laboratory frame), all the high-energy inelastic channels, for instance the production of pions, are still closed.

For proton-nucleus interactions, parametrizations of the Bradt-Peters formula (see Eq. 1.21) are still valid even if comparisons with data are difficult due to the lack of measurements, especially in medium energy range. As it can be noticed from Fig. 2.7, the cross section estimated by the Bradt-Peters model of a proton beam on a Oxygen target reaches a plateau with $E_k > 200\,\mathrm{MeV}$ which is:

$$\sigma_R = 53 A_t^{2/3}\,\mathrm{mb}. \tag{2.5}$$

If we evaluate this latter equation for water as a proxy for human tissue, we end up with a mean free path for protons $\lambda = 82\,\mathrm{cm}$: this means that, for a treatment of a deep-seated tumour ($\approx 20\,\mathrm{cm}$), more than 20% of protons will undergo a inelastic interaction [25].

These interactions create secondary target fragments with very low energies and short range, as little as some human cell diameters. However, the real impact of target fragmentation from a clinical standpoint is still in question [40]. Indeed, low-energy target fragments are densely ionizing particles and their total energy release could enhance the biological damage.

Moreover, their contribution to the total dose seems to be more important in the entrance channel (i.e. in healthy tissue) with respect to the tumour region: according to simulations performed in [41] assuming that a single damage is enough to kill a cell, in the Bragg peak (i.e. when protons are already slow and their nuclear inelastic cross section is higher) only one cell over 40 is killed by a target fragment while the others are killed by ionization events described by the Bethe-Bloch formula. On the other hand, in the entrance channel when protons are still fast and their $\mathrm{d}E/\mathrm{d}x$ increases very slowly, target fragments can kill up to one cell every 8 so that their contribution starts to be quite high.

Some observations in radiobiological experiments indicate that it is worth investigating the production of target fragments: however, up to now there are large gaps in cross sections data and Monte Carlo codes show large discrepancies [42]. For these reasons the FOOT experiment, outlined in Chapter 4, was proposed.

Chapter 3

Radioprotection in space

National space agencies are planning human missions on the Moon and to Mars and the interest is growing in these years. However, among several worrying aspects such as physiological problems caused by microgravity and psychological and medical problems caused by isolation, the health risks related to the space radiation still remain one of the major risks for space exploration beyond Low Earth Orbit (LEO). These hazards could be so important to prevent space missions due to huge costs and unacceptable risks for the astronauts. Moreover, no effective countermeasures are available so far. In the following, the space radiation environment and the challenges on a passive shielding design will be presented.

3.1 Space radiation environment

The space radiation environment is very different from that on the Earth since protons and heavy ions are also present. Moreover, the basic principles to reduce exposure to radiation (increase the distance from the source, reduce the time of exposure, use a shielding) are not valid in space anymore: the space radiation is isotropic so that it is not possible to move away and the time of the exposure is set according to the scope of the mission. For these reasons, shielding is the only way to reduce the exposure to space radiation. In the next two subsections, the two main sources of radiation in space, Solar Particle Events (SPEs) and Cosmic Rays (CRs) will be set out.

3.1.1 Solar Particle Events

The Sun is one of the main sources of radiation in the Solar system. Besides continuous electromagnetic radiation, the Sun releases also a flux of particles, called solar wind, mainly composed of protons and electrons of very low energy (for protons between 1.5 and 10 keV). Due to their energy, they would be stopped in the very first μm of skin without any concern for the astronauts [43]. Nevertheless, from time to time protons are accelerated during *solar flares* up to the GeV region. A solar flare is a sudden brightening observed over the Sun's surface, which is interpreted as a large energy release. Flares occur in active regions around sunspots, where intense magnetic fields penetrate the photosphere to link the corona to the solar interior [44]. Despite the particle flux can undergo a great variation in these events, the total dose absorbed by an astronaut can be very harmful, even lethal if countermeasures are not put in place.

The Sun acts also as a modulator for CRs below few GeV: during solar maximum their flux is lower with respect to solar minimum (Fig 3.1, top). On the other hand, the occurrence of solar flares is more likely during solar maximum. Luckily, since SPEs are mostly protons (no projectile fragmentation) of relatively low energy (their maximum is below 100 MeV), there are no particular issues for astronauts except during Extravehicular Activities (EVA) in which the shielding is minimum or absent (Fig 3.1, bottom).

3.1.2 Cosmic Rays

Besides SPEs, the other important component of space radiation are Cosmic Rays. CRs are high-energy and stable particles originating in astrophysical environments. They are mainly protons and fully ionized atomic nuclei: namely, about 90% of the cosmic ray nuclei are protons, about 9% are helium and all of the rest of the elements make up only 1%. Their energy, as well as their fluxes, spans several orders of magnitude (Fig. 3.2, top) preventing any attempt to stop them in a shielding.

Moreover, the nuclear fragmentation due to the presence of heavy nuclei has to be addressed since, despite the flux of CRs decreases with increasing charge, they account as much as light nuclei to the dose (Fig. 3.2, bottom). Indeed, as it can be seen in Eq. 1.3, the energy loss (and, hence, the dose) scales with Z^2.

The highly mixed nature of the CRs poses big challenges in shielding design: indeed, the optimal choice for shielding is a complex compromise between the two processes occurring in a material exposed to radiation, energy loss and nuclear fragmentation.

3.2 Shielding

As heavy ions traverse the shielding, they undergo several nuclear interactions causing projectile fragmentation into lighter ions and neutrons. In many reactions, fragmentation products are less biologically harmful than the primary ion, hence fragmentation processes can play a role in reducing radiation risks [47]. Moreover, energy loss via electromagnetic interactions has to be taken into account: as the energy loss rate scales with the inverse square of the velocity, ions surviving after passing a shielding can release more energy after the shielding jeopardising the effect of fragmentation. On the other hand, slow ions can be stopped easily with a reasonable amount of material.

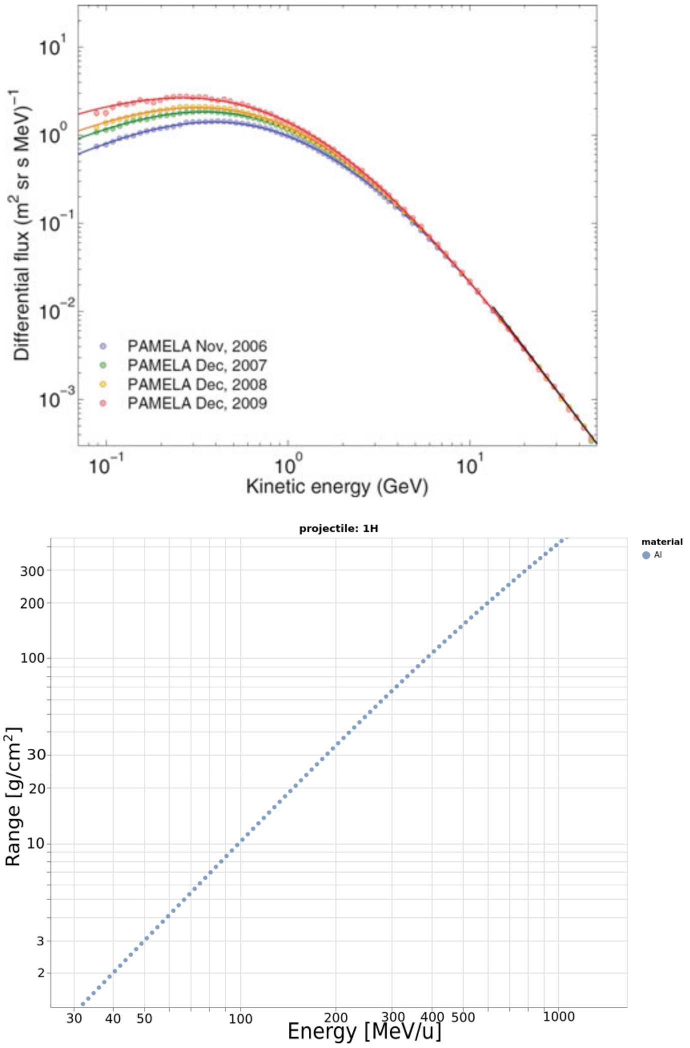

Figure 3.1: Top: The yearly proton energy spectrum measured by the PAMELA experiment from the beginning of the space mission in mid-2006 until the end of 2009. The variation in solar activity does not affect CRs with energy larger than a few GeV [44]. The solar cycle reached a minimum in 2009 and the flux of low energy CRs was higher. Bottom: Energy-range relationship for protons in aluminum. The range is expressed in g/cm^2 , Al density is 2.7 g/cm^3. Typical thickness of the Al spacecraft walls is 5 g/cm^2 while a realistic thickness in a spacecraft is 20 g/cm^2. Range is calculated with ATIMA.

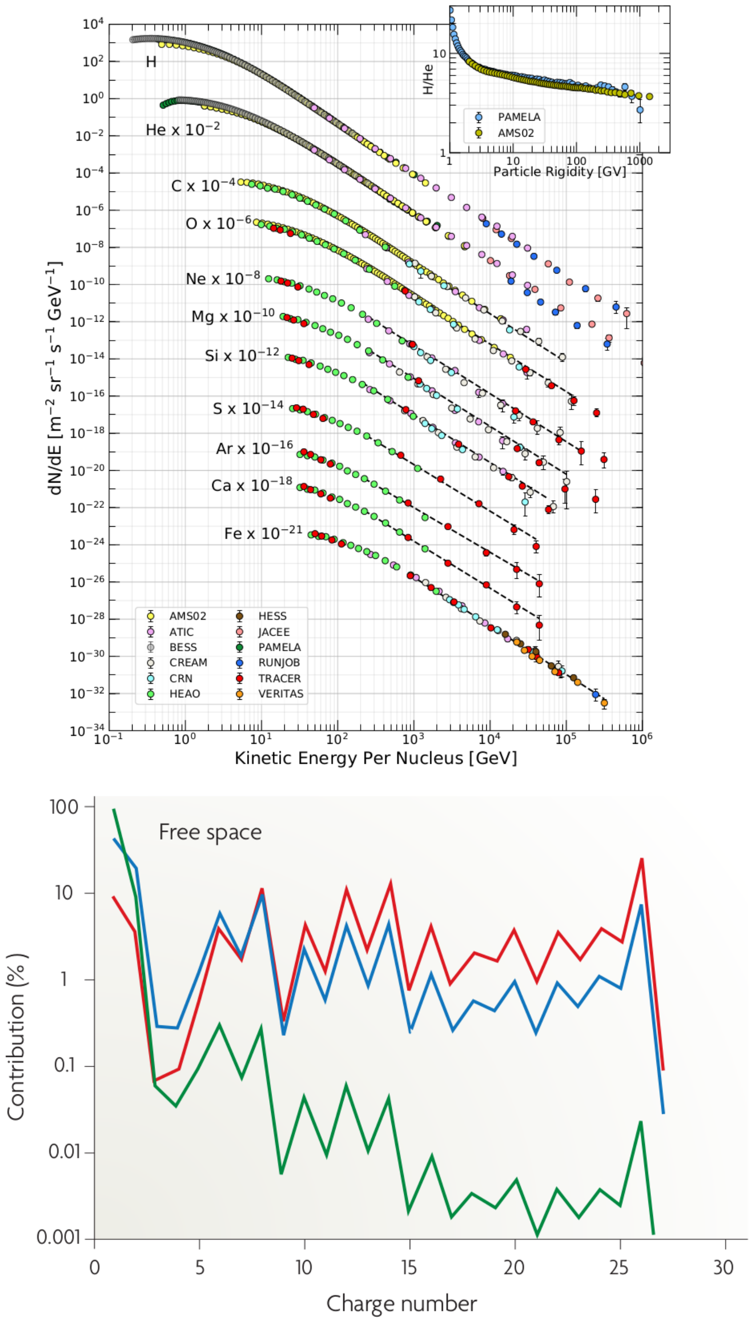

Figure 3.2: Fluxes of nuclei in CR plotted vs energy per nucleus [45] (top). Relative contribution in fluence (green), dose (blue), and dose equivalent (red) of different elements in the CR from the HZETRN computer code. The calculation is an average over a year in solar minimum behind 5 g/cm^2 Al shielding [46] (bottom).

In the design step of a shielding it is crucial to identify some quantities which can allow to characterise different materials, namely in terms of the stopping power and nuclear fragmentation. Regarding electronic energy loss, a handy quantity was already introduced in Chap. 1, i.e. the mass stopping power $\mathrm{d}E/\mathrm{d}\chi$ which can be used as a normalisation among materials.

When using mass stopping power, Bragg curves are plotted against the so called *mass thickness* or *areal density* whose units are $\mathrm{g\,cm^{-2}}$ since it is the product between the density and the thickness of a material: in this view, the total mass of the shielding, which has to be kept as low as possible to avoid a too heavy spaceship, is proportional to the areal density. Hence, the goal is to find the material which shows the highest dose reduction in the minimum areal density.

If we substitute Eq. 1.3 in Eq. 1.5, $\mathrm{d}E/\mathrm{d}\chi \propto Z_t/A_t$ as a first approximation. Indeed, as reported in Fig. 1.1, liquid H_2 has the highest mass stopping power due to its peculiar Z/A ratio. This means that liquid hydrogen can stop a 1 GeV/u heavy ion in a four times lower mass thickness (i.e. total mass) with respect to lead [48].

Regarding nuclear fragmentation, if we evaluate the total reaction cross section per unit mass recalling Eq. 1.21, we get (the number of targets per unit mass is N_a/A_t):

$$\sigma_{\text{mass}}\,[\mathrm{cm^2 g^{-1}}] = \frac{N_a \sigma_R}{A_t} \propto A_t^{-1/3} \tag{3.1}$$

so that lighter materials should be favourable to maximise fragmentations per unit mass.

To summarise in order to limit the weight of the shielding, light materials are more effective for shielding in space and liquid hydrogen has in principle the maximum performance as shield material. However, the use of Hydrogen is not feasible, being a low temperature liquid. Furthermore, using Hydrogen poses several challenges due to its high reactivity. So far, it appears that polyethylene and similar materials can be a good compromise. However, it is important also to characterise the products of such fragmentations since they can cause different effects from a radioprotection standpoint.

In addition, for missions to the Moon and Mars, also *in situ* regolith has to be characterised using available simulants. Indeed, these materials are foreseen to be used to build the shelters during the stay. Shielding transport calculations can harness both deterministic codes, such as HZETRN developed by NASA, and Monte Carlo codes. However, both methods need fragmentation cross sections as inputs which can be provided by models even if several discrepancies are present. The most useful contribution of experimental nuclear physics to this field is to provide double differential cross sections, allowing an extensive benchmark with models [49].

The other approach used to benchmark simulation and transport codes is to measure Bragg curves in different materials as shown in Fig. 3.3. In this scenario, the dose before and after the shielding is measured by ionization chambers in order to evaluate the dose reduction: the choice of materials is a trade-off of performance and safety. For instance, the use of an explosive material, even if excellent in dose reduction, is

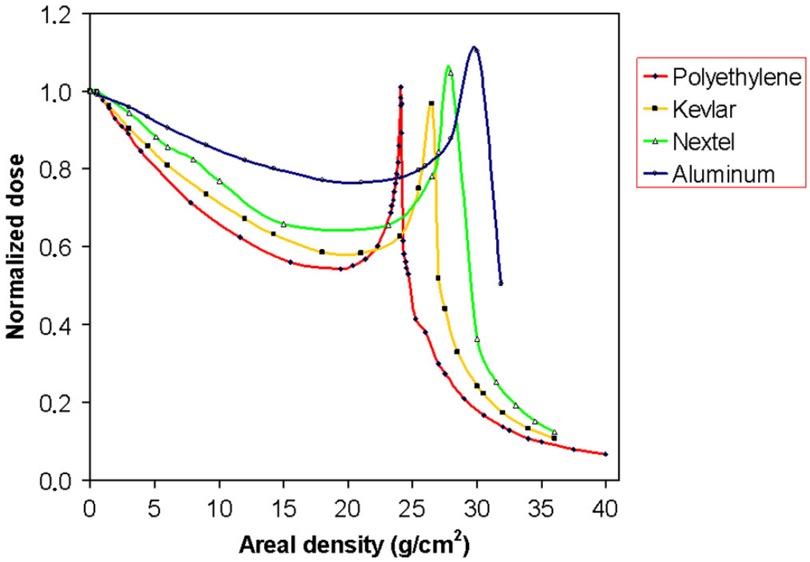

Figure 3.3: Measured Bragg curve of 1 GeV/u Fe ions in polyethylene, aluminum, kevlar, and nextel. The normalized dose is plotted vs. the thickness in g/cm^2. Materials effective for GCR shielding have a higher initial slope and shorter range. Polyethylene is clearly better than Al, and Kevlar is close to polyethylene [50].

forbidden due to safety concerns. Many materials already in use have been characterised in this way, for example nextel and kevlar (commonly used against micrometeorites in space structures as well as in bulletproof vests) or Aluminum. However, a lot of novel materials have not been characterised yet even if interest is growing in these years. In this context, the FOOT experiment could help providing precise measurements of differential fragmentation cross sections, with respect to kinetic energy and production angle of the fragment. These measurements can shed light on material efficiency against space radiation.

Chapter 4

The FOOT experiment

As anticipated in Chapter 2 and 3, the experimental panorama of nuclear cross sections in hadrontherapy and space radioprotection energy range suffers from huge lack of data.

The main goal of the FOOT (*FragmentatiOn Of Target*) experiment is the measurement of target and projectile fragmentation cross sections relevant for hadrontherapy and radioprotection in space using a wide variety of beam species and a large energy range. Firstly, FOOT will be able to measure target fragmentation in proton treatments: as seen in Sec. 2.5.2, the target fragment spectra are extremely peaked to very low energies so that fragments can travel only for distances shorter than $100\,\mu$m preventing any detection. This experimental problem is overcome by using an inverse kinematic approach. In order to obtain these data, 200 MeV/u ^{12}C and ^{16}O beams over C and C_2H_4 targets will be used.

Secondly, FOOT will be able to provide other data from direct kinematics approach about projectile fragmentation in hadrontherapy, notably with Carbon, Oxygen and Helium ions. As seen in Section 2.5.1, Carbon ions fragmentation generate a non-zero dose beyond the Bragg peak, such that they are not suitable to treat cancers just in front of Organs At Risk (OARs). Despite this potential drawback, Carbon ions suffer from a small lateral deflection and they have a narrow Bragg peak which allow a more precise treatment than with protons, and an enhanced biological effectiveness in the tumour. Thus, it is needed to know deeply Carbon fragmentation properties to use it properly in the clinical practice.

Furthermore, Oxygen ions are increasingly considered as a fundamental tool against radioresistant tumours since they can reach a higher value of $\mathrm{d}E/\mathrm{d}x$ while sharing similar characteristics with Carbon ions: their use as a treatment boost can be foreseen in next years.

In addition, Helium beams are regarded as a promising alternative to protons, both for their cost/benefit ratio and for the reduced impact of Multiple Coulomb Scattering. This feature, together with a lower impact of nuclear fragmentation, makes Helium ions suitable to treat cancers near OARs. In order to obtain these data, 250 MeV/u ^{4}He beams and 400 MeV/u ^{12}C, ^{16}O beams with C, C_2H_4 and PMMA targets will be used [51].

Thirdly, measurements performed with FOOT will be also interesting for radioprotection in space, especially for light fragments produced by ions up to Oxygen. Notably, FOOT will measure double differential fragmentation cross sections for $700 - 800$ MeV/u ^{4}He, ^{12}C and ^{16}O beams with C, C_2H_4 and PMMA targets. These beam species are important due to their share in Cosmic Rays (CRs) spectrum and they have a common ground with hadrontherapy measurements.

For these reasons the FOOT experiment was proposed. It is designed to detect, track and identify all charged fragments produced in ion collisions with different targets in order to measure both the projectile and target fragmentation for particle therapy and space radioprotection. In the following sections, the physics program, the experiment tools and the characteristics of the detector will be outlined.

4.1 Experimental panorama

In order to set up FOOT physics program and to define the experimental priorities it is necessary to examine the current experimental panorama (see [52] for a complete overview). Namely, for both hadrontherapy and space radioprotection purposes, a lot of cross sections are still missing. In particular, the interest for target fragmentation in proton therapy covers interactions with energies below pion production threshold, i.e. < 290 MeV/u, while for projectile fragmentation higher energies are involved up to $400 - 500$ MeV/u. Regarding space radioprotection, there are more ion species of interest and the energy can reach 10 GeV/u.

From a wide review of available double differential cross sections it turns out that large gaps in data are present, especially for heavier fragments. Notably, there are a few measurements with Helium projectiles and no double differential cross section data exist for light ion fragment production from Oxygen projectiles above the pion threshold. Moreover, models show large discrepancies even in total reaction cross sections.

Charge-changing cross sections are mostly present in literature since they can be measured with the attenuation approach described in Sec. 1.4: nevertheless, a lot of interesting beam-target settings are still missing between 280 MeV/u and 3 GeV/u and measurements below the pion production threshold are scarce. Regarding isotopic cross sections, their measurements involve mass identification capabilities thus large gaps in the literature are present, both for light (i.e. H and He) and medium fragments (up to Nitrogen).

This scenario turns to be poorer when dealing with differential cross section: regarding angular cross sections, there are very few data since most of experiments employ a on-axis setup and non-segmented detectors. For energy differential cross sections, a major problem is the need for a detector able to measure the energy of the fragment: for this reason, data are even more scarce than angular ones.

The physics program of the FOOT experiment aims at covering these gaps in data using both direct and inverse kinematics approaches with different targets to fully harness allocated beam time in various experimental facilities. In addition to the current physics program outlined at the beginning of this Chapter, FOOT will be able to test also other targets such as novel shielding materials in space radioprotection context.

4.2 Inverse Kinematics and Cross Sections

As already mentioned in Chapter 2, target fragments produced in proton collisions with a target have a very low recoil energy preventing them to exit even from a thin target. To overcome this difficulty, an inverse kinematic approach will be used: instead of shooting a proton beam on a human tissue-like target (^{16}O, ^{12}C), a ^{16}O, ^{12}C beam is shot on a Hydrogen target. Then, applying a proper Lorentz boost, it is possible to retrieve the proton-nucleus cross section of interest. This kind of measurements is quite challenging as the initial momentum of primary particle has to be known with extreme precision not to spoil the outcome of the measurement.

Moreover, as handling Hydrogen targets in FOOT-like scenarios could be a difficult task, cross sections will be evaluated using pure and composite targets with Hydrogen such as C and C_2H_4. Then, as shown in [53], it is possible to get back cross sections with Hydrogen by combining cross section on different targets as follows (here for angular cross section):

$$\frac{\mathrm{d}\sigma}{\mathrm{d}\Omega}(\mathrm{H}) = \frac{1}{4} \cdot \left(\frac{\mathrm{d}\sigma}{\mathrm{d}\Omega}(\mathrm{C_2H_4}) - 2 \cdot \frac{\mathrm{d}\sigma}{\mathrm{d}\Omega}(\mathrm{C}) \right). \tag{4.1}$$

It is worth considering that the uncertainties resulting from this method are the quadratic sum of the uncertainties of cross sections on both targets so that the number of primary particles has to be adjusted to keep the error on Hydrogen cross section as low as possible.

The FOOT experiment, given the wide experimental panorama and the requested adaptability, was designed in two alternative and complementary setups.

4.3 The electronic setup

The electronic setup was designed to detect and identify fragments heavier than ^{4}He with an angular acceptance up to a polar angle of 10°. Some constraints had to be taken into account during the design phase of the FOOT experiment: firstly, the need for an accurate charge and isotopic identification of the produced fragments required a redundancy in measuring kinematic quantities of produced fragments. Secondly, as the detector should be moved according to the availability of different ion beams, it has to be

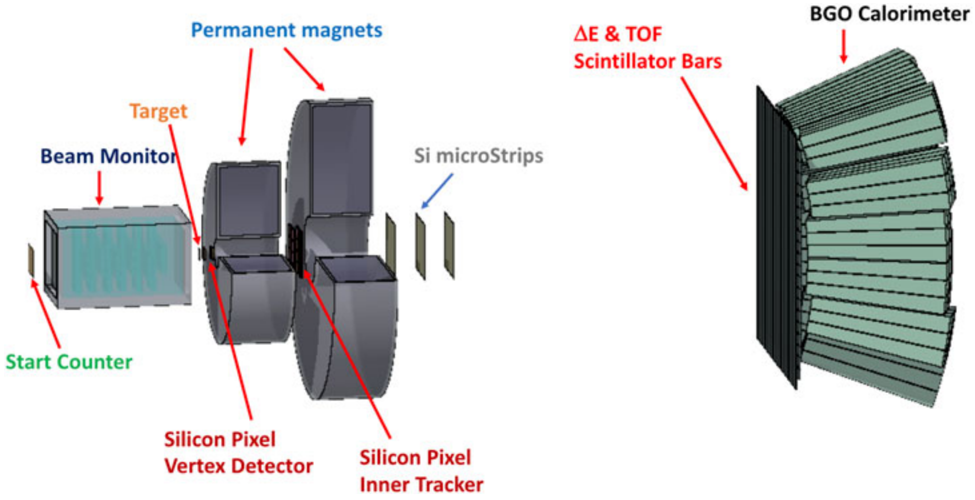

Figure 4.1: Schematic view of the electronic setup [51].

flexible and with a table-top concept. Eventually, in order not to spoil the measurements, the fragmentation contribution from the detector itself has to be kept as low as possible.

To achieve these goals, the FOOT setup includes a ΔE-TOF system and a calorimeter to measure the velocity, the charge and the kinetic energy of the fragment. Moreover, a magnetic spectrometer equipped with three tracking stations and two permanent magnets will provide a measure of the momentum of the fragments. A schematic view of the electronic setup is shown in Fig. 4.1.

The final goal of the FOOT experiment is to measure differential cross sections with respect to the kinetic energy $\mathrm{d}\sigma/\mathrm{d}E_{\mathrm{kin}}$ for the target fragmentation process with an accuracy better than 10% and double differential cross sections $\mathrm{d}^2\sigma/\mathrm{d}\Omega\mathrm{d}E_{\mathrm{kin}}$ for the projectile fragmentation process with an accuracy better than 5% on the determination of the fragment yields in angle and in kinetic energy.

In order to match the required resolution it will be necessary to achieve the following experimental resolutions (σ):

- $\sigma(p)/p$ at level of $4-5\%$;
- $\sigma(T_{\mathrm{tof}})$ at level of 100 ps;
- $\sigma(E_{\mathrm{kin}})/E_{\mathrm{kin}}$ at level of $1-2\%$;
- $\sigma(\Delta E)/\Delta E$ at level of 5%;

where p is the momentum of the fragment, T_{tof} is the Time of Flight measurement, E_{kin} is the kinetic energy of the fragment and ΔE is the energy lost in the ΔE-TOF detector by the fragment [51]. These experimental resolutions resulted from an intense analysis of Monte Carlo simulations during the design phase of the experiment.

In the following, all subdetectors composing the electronic setup will be described.

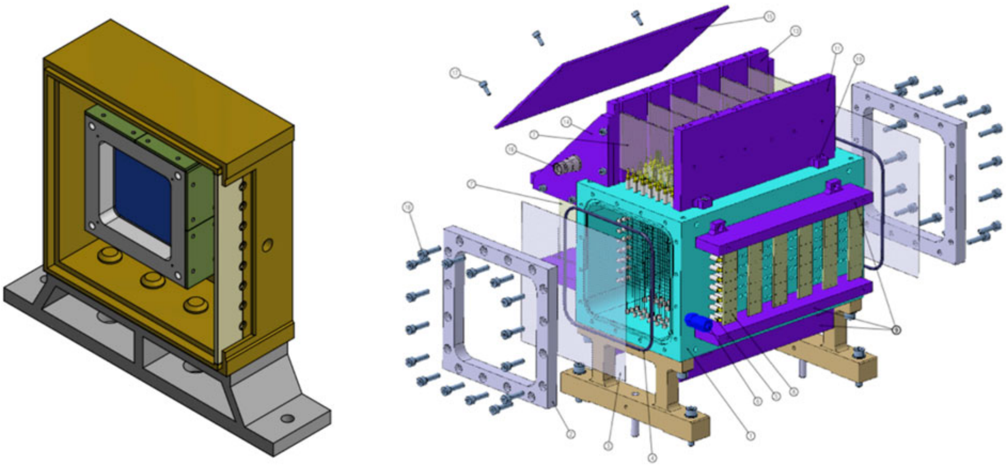

Figure 4.2: Start Counter detector inside the plastic box, the EJ-228 plastic scintillator foil is in dark blue (left). Technical drawing of the Beam Monitor drift chamber. The two orthogonal views x–y of the wires are clearly visible (right) [51].

4.3.1 Start Counter and Beam Monitor

The Start Counter (SC), placed at the very beginning of the setup, has several tasks: it provides the minimum bias trigger of the experiment, it measures the incoming ion flux, it provides the reference time for other detectors and the start time for the Time Of Flight (TOF) measurement. The SC is made by a thin foil of EJ-228 plastic scintillator 250 μm thick with an active surface of $5 \times 5\,\mathrm{cm}^2$. The light produced in the scintillator is collected laterally by 48 $3 \times 3\,\mathrm{mm}^2$ SiPMs, 12 per side, bundled in eight electronic channels. The readout and the power supply of the SiPMs is handled by the WaveDAQ system [54], which is able to sample signals at rates up to 5 GS/s in a dynamic range of 1 V. A gain between 0.5 and 100 can be applied to the incoming signal before digitization allowing to broaden the detector response in case of different beam types or energies. According to latest results, the SC time resolution is lower than 45 ps with 400 MeV/u Carbon ions.

The Beam Monitor (BM) is a drift chamber consisting of twelve wire layers, with three drift 16 mm × 10 mm cells per layer (Fig. 4.2). Planes with wires oriented along the x and y axes are alternated allowing the beam profile reconstruction in both views. In each view, two consecutive layers are staggered by half a cell to solve left-right ambiguities in track reconstruction. The BM operates at ≈ 0.9 bar with a 80/20% gas mixture of $\mathrm{Ar/CO_2}$, at a working point ranging between 1850 and 2200 V, depending on the primary beam. The BM efficiency is higher than 90% for a wide range of beams and energies while a lower limit on the spatial resolution of 100 μm, in the central part of the BM cell, has been achieved [55].

The BM detector will be placed between the SC and the target and will be used to measure the direction and interacting point of the beam ions on the target: in this way, it can provide a very important information which becomes mandatory at high beam rates to solve the pile-up ambiguity in tracking detectors. Moreover, the BM is able to veto on events in which a beam fragmentation occurs before the target. In order to reject pile-up vertices, an high precision alignment is required between the BM and the devices downstream the target so that dedicated alignment runs are mandatory.

The BM high spatial resolution is of paramount importance to measure the direction of the fragments with respect to the beam with an accuracy of few mrad which is necessary to measure the kinetic energy of the fragments in inverse kinematic with the required resolution.

4.3.2 Vertex detector and Inner Tracker

The Vertex detector (VTX) is organized in 4 different pixel sensor layers covering an area of $2 \times 2\,\text{cm}^2$, placed along the z axis, respectively at $0.6 - 0.9 - 2.1 - 2.4\,\text{cm}$ from the target center ensuring a geometrical acceptance of about 40° for the produced fragments.

In order to fulfill the required performances and constraints, the technology of the MIMOSA-28 (M28) Monolithic Active Pixel Sensors (MAPS) has been chosen (Fig. 4.3, left). The M28 sensor, developed by the Strasbourg CNRS PICSEL group for the upgrade of the vertex detector inner layer of the STAR experiment at RHIC, consists of a matrix with 928 (rows) $\times 960$ (columns) pixels of $20.7\,\mu$m pitch. The chip total size is $20.22\,\text{mm} \times 22.71\,\text{mm}$ and each M28 sensor is $50\,\mu$m thick, resulting in an overall material budget for the entire Vertex tracker of $200\,\mu$m. The sensor employs a rolling shutter readout technique with a $185.6\,\mu$s frame readout time: all the pixels output of one row are read out in parallel row by row at the end of the column. Hence the M28 sensor is the slowest detector, thus setting the maximum trigger rate for the experiment at the kHz level.

The VTX readout has been implemented using a DE10 board system equipped with an Intel System-on-Chip (SoC) FPGA (Cyclon V) with a dual-core Cortex-A9 CPU [51]. The FPGA is interfaced both with the sensors and with the central DAQ (trigger, time-stamping and busy signals) while the CPU sends data to the central DAQ via a 1 Gb Ethernet connection. The kinematic inverse approach requires to know the direction of primary particles before the target and the fragment emission angle after the target with an angular accuracy at the mrad level. The high spatial resolution of $5\,\mu$m achieved with the VTX, matched with the information from the BM, can provide the needed angular resolution.

The Inner Tracker (ITR) foresees two planes of pixel sensors to track the fragments between the two magnets at a distance of about 15 cm from the target. In order to fit the required acceptance, granularity and tracking performances the M28 sensors are arranged in ladders: each ITR plane is composed of two ladders supported by a mechanical frame as in Fig. 4.3, right and each ladder hosts eight M28 sensors. The ITR detector covers a sensitive area of about $8 \times 8\,\text{cm}^2$. Such design was adopted both for geometrical

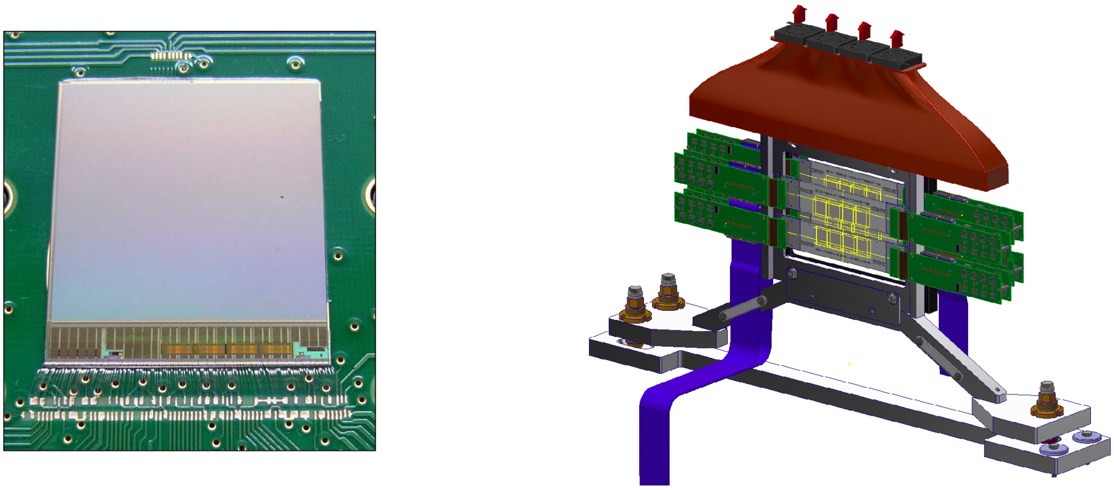

Figure 4.3: Picture of M28 pixel sensor (left). Drawing of the IT detector along the beam line (right).

constraints and for the need to keep low the overall material budget.

4.3.3 The magnetic system

The need to keep the electronic setup movable together with the tight constraints to reach the required momentum resolution, guided the choice for a permanent magnet. In order to avoid a magnetic system in vacuum without spoiling the resolution, two magnets in Halbach configuration were chosen: this configuration allows to add a tracking station inside the magnetic field (i.e. the ITR) as shown in Fig. 4.4. The first magnet has a gap diameter of 5 cm while the second one of 10.6 cm. They can provide respectively a maximum intensity of 1.4 T and 0.9 T along the y axis in the internal cylindrical hole. Each magnet will be made of twelve single units of Samarium-Cobalt, which maintains its magnetic properties also in high radiation environments.

Thanks to a detailed field map (Fig. 4.4, bottom), it will be possible to reach the intrinsic achievable accuracy of about 10 μm. Moreover, both magnets can be vertically lifted of about 40 cm, allowing to align the whole magnetic spectrometer in specific runs without the magnetic field and to access easily to the detectors.

4.3.4 Micro Strip Detector

After the magnets, a third tracking station is present: this is essential both to measure the momentum of fragments and to match them with the hits in the ΔE-TOF detector and in the calorimeter. For such a tracking station a microstrip silicon detector (MSD), which can also provide a redundant measurement of $\mathrm{d}E/\mathrm{d}x$ thanks to its analog readout,

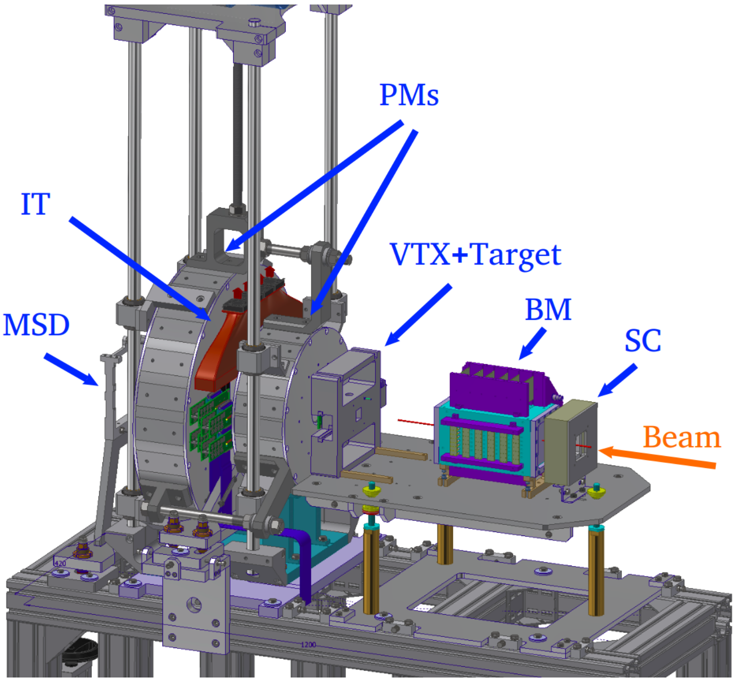

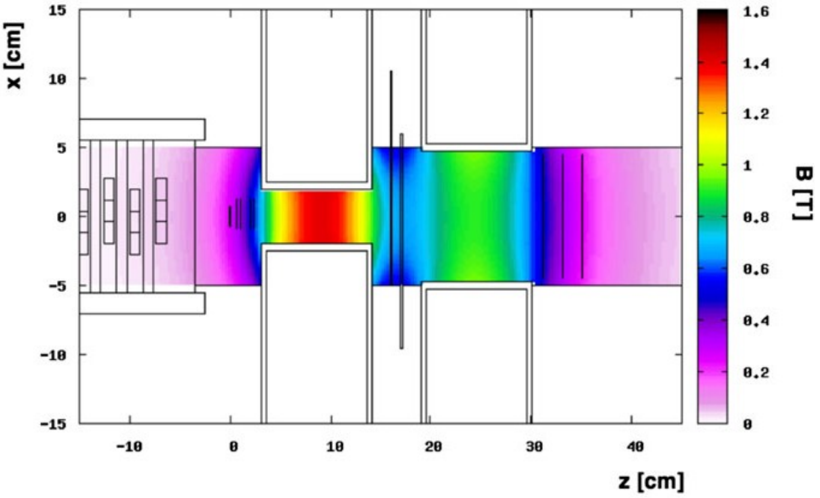

Figure 4.4: (Top) Technical design of the interaction and tracking regions: the vertical axis is the y axis, while the horizontal axis is the z axis. The beam coming from the right, along the z-axis, cross sequentially the Start Counter (SC), the Beam Monitor (BM), the target (TG), the vertex detector (VTX), moves into the Permanent Magnets (PMs) region and crosses the Inner Tracker (ITR) and, immediately after the second magnet, passes through the Micro Strip Detector (MSD). (Bottom) Computed magnetic field map produced by the FOOT magnets in Halbach configuration. The magnetic field intensity B, shown in the palette, is referred to its y-axis component [51].

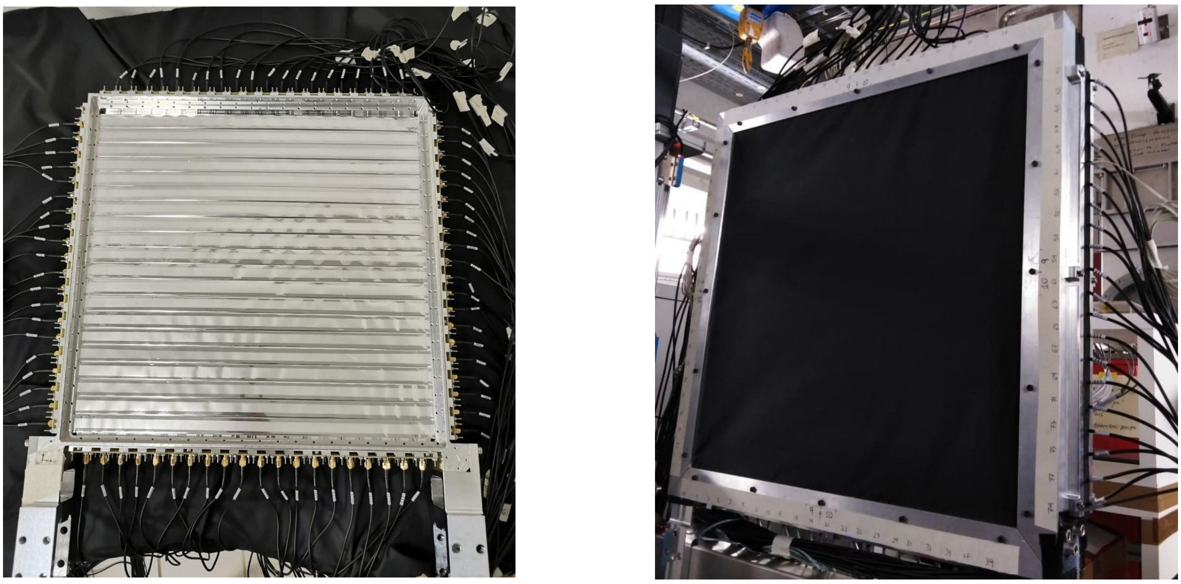

Figure 4.5: Picture of ToF Wall detector during the assembly (left) and on the beam line (right).

was chosen. The detector is composed by three x-y planes with an active area of 9.6 × $9.3\,\mathrm{cm}^2$, separated by a 2 cm gap along the beam direction and positioned right after the second magnet. In order to reduce the amount of material and to provide the x-y coordinate readout, a setup with two perpendicular $150\,\mu$m thick Single-Sided Silicon Detector (SSSD) sensors has been adopted for each MSD x-y plane. A strip pitch size of $50\,\mu$m has been chosen in order to minimize the fragment pile-up in the same strip. For each SSSD, one every three strips is read for a total of 640 channels.

A technical drawing of the interaction and tracking region of the electronic setup is reported in Fig. 4.4, top.

4.3.5 ToF Wall

The ToF Wall detector (TW) (Fig. 4.5) is composed of two layers of 20 plastic scintillator bars (EJ-200 by Eljen Technology), arranged orthogonally and wrapped with reflective aluminum and darkening black tape. Each bar is 0.3 cm thick, 2 cm wide and 44 cm long. The two orthogonal x-y layers form a $40 \times 40\,\mathrm{cm}^2$ active area detector that provides the measurements of the energy deposited ΔE, the stop time to compute the TOF (the start time is provided by the SC), and the hit position.

The simultaneous measurement of ΔE and TOF allows to identify the charge Z of the crossing ions. The Z-identification plays a fundamental role in determining the fragment mass and is used, together with the x-y hit position, as a seed for the track reconstruction through the magnetic field. The TW transverse dimensions have been chosen to match the angular aperture of the heavy fragments at the distance of the detector from the target ($1-2\,\mathrm{m}$) depending on experimental room conditions. The chosen granularity keeps the pile-up of multiple fragments in the same bar below 1%. The thickness of the bar has been chosen as a trade-off between a higher scintillation signal (reflecting in better timing and energy resolution) and a lower secondary fragmentation probability in the bars, which would spoil the particle identification and tracking. Each of the two edges of the TW bars is coupled to 4 SiPM with a $3\times3\,\mathrm{mm}^2$ active area and $25\,\mu\mathrm{m}$ microcell pitch. The signals of each channel (two channels per bar) are digitized at rates of $3-4\,\mathrm{GS/s}$ by the WaveDAQ system [54] as for the SC. A total of 1024 samples are collected for each signal allowing to record the whole waveform and to extract offline the time and the charge information. The thickness of the bars and the selected readout chain have been chosen to meet the FOOT requirements of a TOF resolution better than 100 ps and an energy loss resolution $\sigma(\Delta E)/\Delta E \approx 5\%$, for the heavier fragments. Thanks to the high number (4×14400) of pixels per channel of the SiPM, this setup is able to guarantee a dynamic range spanning over two orders of magnitude and allow the identification of fragments with significantly different energy release (from proton to Oxygen with different kinetic energies). Finally, the high precision time measurement can be used to reconstruct the hit position along the bar with a precision $\sigma_{\mathrm{pos}} < 8\,\mathrm{mm}$, better than the one achievable only exploiting the information about the bars crossing, an important information used to reduce the combinatorial association of multiple fragments in the front and rear side of the TW in the offline reconstruction.

4.3.6 Calorimeter

The FOOT calorimeter is the most downstream detector and it is designed to measure the kinetic energy of the fragments thus computing their mass A. Depending on the energy of the incoming fragment, different phenomena can take place in the calorimeter in the energy range of interest for the FOOT experiment.

At the highest energies, $\approx 700-800\,\mathrm{MeV/u}$, that will be used for space radioprotection purposes, the pion production threshold is exceeded and hadronic showering takes place. In these conditions a full containment cannot be achieved with affordable calorimeter dimensions, resulting in a worsening of the achievable resolution. However, the highest resolution is needed for target fragmentation studies, which involves $^{12}\mathrm{C}$ and ^{16}O up to $200\,\mathrm{MeV/u}$. In this energy range, the main mechanism of energy loss is the inelastic interaction with electrons described by the Bethe-Bloch formula. Nevertheless, in a fraction of events neutrons are emitted and part of the fragment energy escapes the detector. To cope with this issue, redundant information from other detectors will be used.

Since FOOT is expected to work at low beam intensities, there was no strict request on the detector decay time: hence, the choice was oriented to a dense crystal with high light yield with limited costs. Following this assessment, $\mathrm{Bi_4Ge_3O_{12}}$ (BGO) was chosen: the FOOT calorimeter will be composed by 320 BGO crystals covering an almost circular

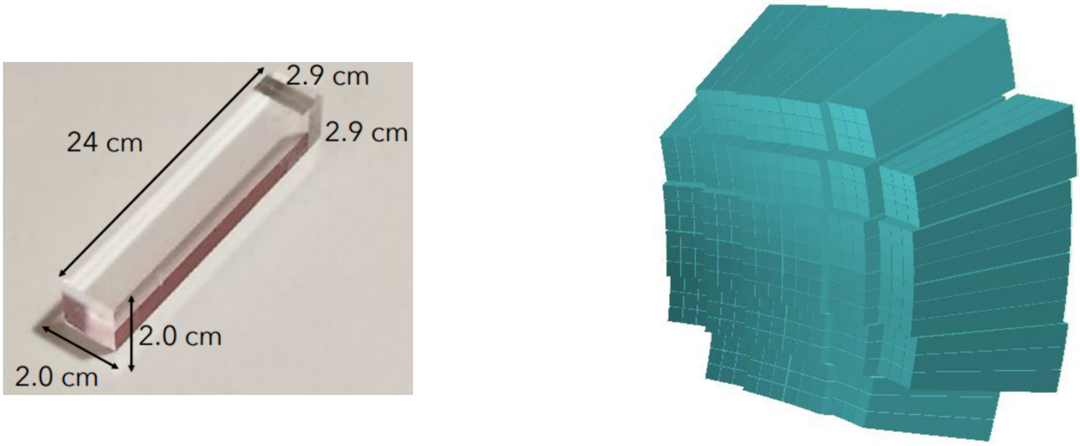

Figure 4.6: Picture of a BGO crystal (left) and schematic view of the FOOT calorimeter (right).

area of $\approx 20\,\text{cm}$ radius (Fig. 4.6). The crystals have a truncated pyramid shape with a front (back) area of about $2\times2\,\text{cm}^2$ ($3\times3\,\text{cm}^2$) and a length of 24 cm, chosen to minimize the energy leakage mainly due to neutrons escaping the calorimeter.

Each BGO crystal is coupled to a 25 SiPMs matrix with an active surface of $2\times2\,\text{cm}^2$. Each microcell has a $15\,\mu$m pitch, allowing to have a linear response in energy range up to about 10 GeV. The calorimeter will be readout by the WaveDAQ system as the SC and TW detectors at a rate of 1 GS/s in order to sample the full waveform.

Several beam tests with different ions and energies were performed showing a very good linearity response and a energy resolution $\sigma(E_\text{kin})/E_\text{kin}$ below 2% for heavier fragments.

4.3.7 Mass identification

The mass identification is a more complex task with respect to charge identification which will be described in detail in Chap. 6. For this reason, thanks to the redundancy of the FOOT setup, the mass of the fragments can be measured in three different ways combining the momentum, the TOF and the kinetic energy measurements:

$$p = mc\beta\gamma \tag{4.2}$$

$$E_\text{kin} = mc^2(\gamma - 1) \tag{4.3}$$

$$E_\text{kin} = \sqrt{p^2c^2 + m^2c^4} - mc^2 \tag{4.4}$$

where p is the momentum of the fragment, E_kin is its kinetic energy, γ is the Lorentz factor and β is the velocity of the fragment.

Since the calorimeter suffers from the neutron production, the best mass identification involves TOF and momentum measurements. However, all the three methods

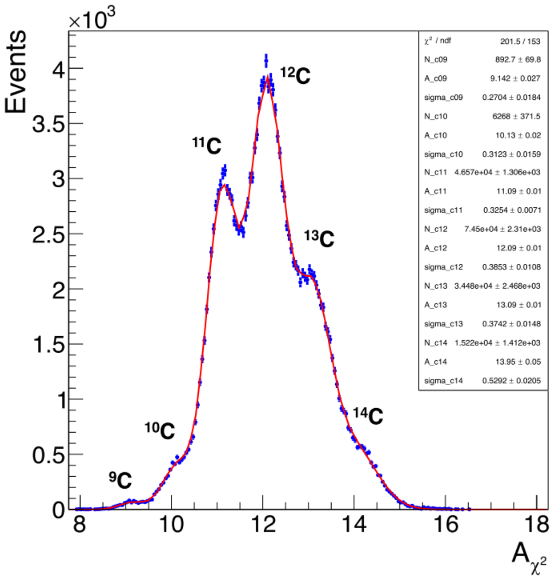

Figure 4.7: An example of mass number determination obtained with the χ^2 fit for the Carbon fragments for the case of $\sigma(T_{\text{tof}}) \approx 70\,\text{ps}$, $\sigma(p)/p \approx 3.7\%$ and $\sigma(E_{\text{kin}})/E_{\text{kin}} \approx 1.5\%$. The ^{11}C, ^{12}C and ^{13}C isotopes are clearly visible [51].

are employed to reduce the systematic uncertainties achieving the best results. To this end, two methods are used to combine all the measurements, namely the standard χ^2 minimization algorithm and the Augmented Lagrangian Method (ALM).

The first method is based on the minimization of the function

$$\chi^2 = \frac{(T_{\text{tof}} - \overline{T_{\text{tof}}})^2}{\sigma^2(T_{\text{tof}})} + \frac{(p - \overline{p})^2}{\sigma^2(p)} + \frac{(E_{\text{kin}} - \overline{E_{\text{kin}}})^2}{\sigma^2(E_{\text{kin}})} + \mathbf{A}^T \left(\mathbf{C}\mathbf{C}^T\right)^{-1} \mathbf{A} \tag{4.5}$$

where T_{tof}, p and E_{kin} are the reconstructed values, $\sigma(T_{\text{tof}})$, $\sigma(p)$ and $\sigma(E_{\text{kin}})$ are their uncertainties and $\overline{T_{\text{tof}}}$, $\overline{p}$ and $\overline{E_{\text{kin}}}$ are the fit output parameters.
$\mathbf{A} = (A_1 - \overline{A} \quad A_2 - \overline{A} \quad A_3 - \overline{A})$ is a vector where A_1, A_2 and A_3 are the reconstructed mass values from the three methods and $\overline{A}$ is a fit output parameter while $\mathbf{C}$ is the correlation matrix.

Instead, the ALM is based on a iterative procedure of minimization of the Lagrangian function $\mathcal{L}$:

$$\mathcal{L}(\overrightarrow{x}, \lambda, \mu) = f(\overrightarrow{x}) + \sum_{i=1}^{3} \lambda_i c_i(\overrightarrow{x}) + \frac{1}{2\mu} \sum_{i=1}^{3} c_i^2(\overrightarrow{x}) \tag{4.6}$$

where $f(\overrightarrow{x})$ is the function shown in Eq. 4.5 except for the last term, $c_i(\overrightarrow{x}) = (A_i - \overline{A})$ are the constraints, λ_i are the Lagrange multipliers and μ is the penalty parameter.

The results obtained with the two methods are similar: as reported in Fig. 4.7, the ^{11}C, ^{12}C and ^{13}C peaks are clearly visible thus mass identification can be performed.

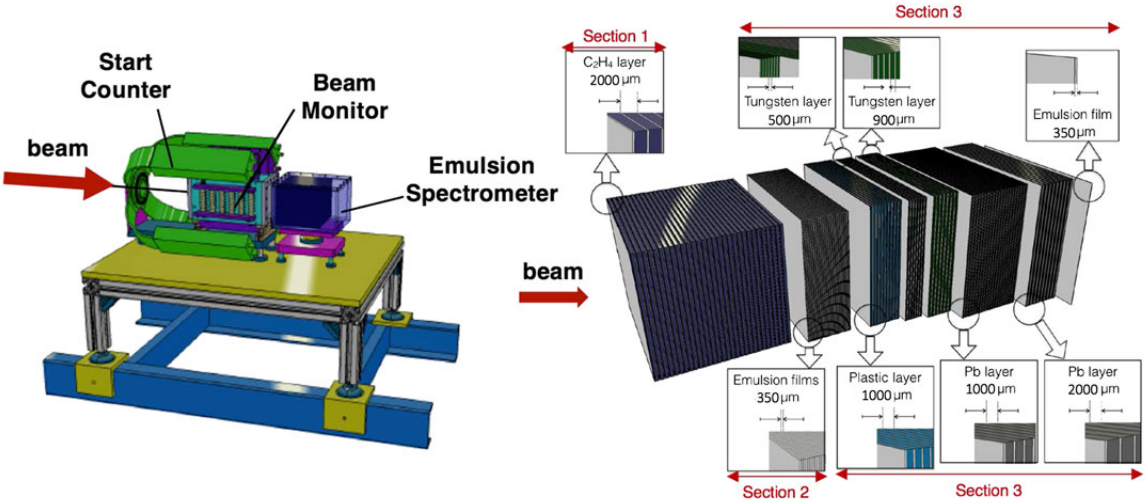

Figure 4.8: (Left) Emulsion spectrometer setup. (Right) Scheme of the emulsion spectrometer composition with C_2H_4 target [51].

4.4 The Emulsion Spectrometer

To characterize the production of low Z fragments with large polar angle (up to 70°), also an emulsion spectrometer (ES) has been included in the FOOT project. In Fig. 4.8 left, the arrangement of the emulsion chambers inside the FOOT detector is shown: the ES is placed after the SC and the BM, with the beam incoming from the left. The SC and BM are used only for beam monitoring purposes and the ES is a complete independent experiment. The SC and BM have been used to perform an online control of the beam flux on the active ES surface, to avoid spatial pile-up of events in the ES.

Among all tracking devices used in particle physics, nuclear emulsion detectors achieve the highest spatial resolution (sub-micrometric) for tracking ionizing particles. Emulsion chambers integrate target and detector in a very compact setup and provide a very accurate reconstruction of the interactions occurring inside the target. Moreover, no power supply or any readout electronics is required and this helps to keep the emulsion setup compact and handy to perform measurements in different experimental conditions.

As emulsions are pure passive detectors, they have to be developed after exposure: last generation microscopes provide a fast and automated scanning of all the films allowing a fast development with respect to a few years ago. Moreover, it is well known that it is possible to extend the dynamical range of emulsion by thermal treatments allowing charge identification of the produced fragments. The nuclear emulsion films, used for the FOOT experiment, consist of two $70\,\mu$m thick sensitive layers deposited on both sides of a $210\,\mu$m plastic base, resulting in a total thickness of $350\,\mu$m. The sensitive regions are made of AgBr crystals of $0.2\,\mu$m diameter scattered in a gelatine binder, able to detect charged particles. Then, all the nuclear films are developed and a track reconstruction algorithm finds all the track candidates. This process is quite delicate since in the ES all the events occurring during the exposure are piled up and have to be disentangled. Moreover, the ES can be used only once for a given beam and energy since the imprinting process cannot be reverted.

The FOOT ES is composed by three sections devoted to different tasks (refer to Fig. 4.8 right for ES sections):

- interaction and vertexing region (Section 1);
- charge identification region (Section 2);
- momentum measurement region (Section 3).

4.4.1 Interaction and vertexing region

This section is made of several elementary cells composed of layers of target element, C or C_2H_4 , alternated with emulsion films, as shown in Fig. 4.8 right. The primary particle can interact in any of these layers and secondary fragments are detected by next layers. The detector emulsion structure will track the fragments and reconstruct the interaction vertex position. The length of this section will be optimized for each different data taking, to achieve a statistically significant number of reactions accordingly to the combination of ion beam, energy and target. While with thin targets used in electronic setup the fragmentation rate of primary particles is as low as a few percent, the ES setup can reach a fragmentation rate up to 30%.

4.4.2 Charge identification region

The particles at the minimum of their ionizing power (MIPs) generate in nuclear emulsion thin tracks whose grain density ranges from 30 to 50 grains/100 μm, according to the emulsions sensitivity so that emulsions could show saturation effects with highly ionizing particles. However, by keeping them for an appropriate time at a certain temperature and humidity (for instance 28° and 95%), it is possible to erase them to some extent. The combination of several films, treated with different conditions (four, in FOOT ES case) after the exposure, can make emulsions insensitive to MIPs, protons and so on allowing a charge separation of produced fragments in the analysis step.

4.4.3 Momentum measurement region

The third section is made of emulsion films alternated with layers of passive material, as shown in Fig. 4.8 and it is dedicated to the momentum measurement. The section length, the number of passive layers and their thicknesses are set according to the incident beam energy. The materials used as passive layers at the data taking performed with the ES at GSI in 2019 were Lexan, W and Pb and their thicknesses ranged from 0.5 to 2 mm. Then, the momentum is evaluated with the range technique measuring the total length of the particle track and translating into a kinetic energy measurement (see Sec. 1.2).

Moreover, thanks to their high precision, emulsions can provide also an independent measurement of the momentum through the Multiple Coulomb Scattering method (see Sec. 1.3 and Eq. 1.16). In this way, both charge and mass identification of the emitted fragments can be performed [56].

Chapter 5

Trigger and Data Acquisition (TDAQ) system

As described in Chap. 4, the electronic setup of the FOOT experiment is composed by several subdetectors with different architectures. The system which takes care of collecting all data and of the management of the whole data acquisition is the *Trigger and Data Acquisition (TDAQ) System.*

The process of Data Acquisition encompasses all the steps from the generation of signals in the detector until their processing and storage on a disk. Several sectors can be identified, from the *front end electronics*, i.e. the first element near the detector which has often the task to convert analog to digital signal to the final event building. Moreover, TDAQ manages the distribution of trigger and busy signals which follow a complete different path from data.

Since FOOT is composed by several detectors, frontend electronics is managed by detector groups and the central DAQ system has to guarantee a correct event building of different detectors, i.e. to put correctly together data from different detectors. Moreover, these detectors are very different thus requiring multiple readout strategies, from standard electronics (i.e. VME boards) to FPGAs and custom electronics.

In this Chapter, some basic DAQ concepts useful for the FOOT experiment together with a description of the FOOT TDAQ system will be set out. Moreover, monitoring tools as well as the tools implemented for past and future data takings will be presented. Eventually, TDAQ performances under various conditions are shown.

5.1 Trigger

In many experimental scenarios, only a fraction of data can contain new and relevant physical information. For instance, fragmentation events in FOOT electronic setup are present in a few percent while in most cases primary particles do not interact in the target. In other cases, such as High Energy Physics (HEP) experiments (i.e. at LHC), the rate is as high as 40 MHz and it would be impossible to store data at such high rates.

For this reason, most of experiments implement a *trigger*: its task is to select interesting events in real-time based on experiment requests. The trigger is actually a condition which decides either to accept or to reject the event. A good trigger should be selective, i.e. efficient in identifying interesting events and in rejecting others, simple (since it should be implemented also in simulations) and quick as related physics can develop in very short time.

In most experiments, when a trigger occurs, the event is already developed in all detectors which should keep the information for a reasonable amount of time. The time passing between the formation of the signal and the trigger distribution to all detectors is called *latency*. It has to be under control event per event and kept as low as possible.

The FOOT electronic setup works mainly with two different triggers: the minimum bias and the fragmentation trigger to enhance the fraction of interesting recorded events. Both are generated by the WaveDAQ and issued by the V2495 board (see Sec. 5.4): the minimum bias trigger is designed to be generated when a particle of the beam enters the Start Counter.

On the other hand, the fragmentation trigger is expected to be generated when a fragmentation occurs. Namely, if the TOF wall detects an energy release outside the beam position or lower than what expected for the beam the trigger is generated.

Detectors can be triggered or triggerless: in the former case, detector are read only when a trigger occurs while in the latter the data flux from detectors is continuous. Among FOOT detectors, only the Vertex sensors (M28 chips) have a triggerless architecture: however, the Vertex readout electronics sends data to the central DAQ only if a trigger is received.

5.2 Requirements

Every experiment can have different DAQ requisites to acquire data. In particular, FOOT TDAQ has to be compact, easily movable and able to handle many different kinds of detectors. Indeed, looking at the electronic setup following the beam path as already done in Chap. 4, a lot of different readout techniques can be found: custom systems as DE10 boards for VTX, ITR and MSD, complex data acquisition systems as WaveDAQ for the Start Counter, ToF Wall and Calorimeter, standard VME boards for central trigger and Beam Monitor readout.

Memory and speed requirements have to be evaluated both on detector and physics standpoint. The maximum acquisition rate with the Minimum Bias trigger depends only on the beam rate and on the slowest detector of the experiment, i.e. the Vertex Detector which has a frame readout time of 185.6 μs which corresponds to a maximum theoretical readout rate R_{max} of about 5 kHz. Since the sensors are read in a rolling shutter mode, to be sure of collecting all the data for a given interaction, three consecutive frames are readout for each trigger, requiring at least $557\,\mu$s reducing the theoretical R_{max} to 1.8 kHz. The system was designed to handle an acquisition rate $R_{\mathrm{daq}} = R_{\mathrm{max}}$ but in order to reduce the pileup in the M28 chips the maximum acquisition rate is set at ≈ 1 kHz. If one considers a duty cycle of $f_{\mathrm{up}} = 30\%$ in stable running conditions, the FOOT experiment is able to collect up to 26 millions events per day.

The average size of a FOOT event is 70 kB, which means that at 1 kHz rate the data flow can be as high as 70 MB/s (≈ 2 TB per day). In order to avoid a bottleneck on writing data on disk, a SSD (Solid State Drive) disk was chosen: its writing speed (≈ 400 MB/s) is significantly higher than a normal HDD (Hard Disk Drive, maximum 150 MB/s) which would be too slow to store data during the run.

However, current prices per TB are much higher for SSD than for HDD so that a HDD-based offline storage is preferred. This is fulfilled by means of a 30 TB NAS (Network Attached Storage) in which data are transferred during idle times. Eventually, data stored on NAS are copied and backed up to long-term storage, i.e. CNAF in Bologna and GSI in Darmstadt, thus making them available for the whole collaboration.

5.3 The FOOT TDAQ architecture

The DAQ system designed for the whole apparatus is a flexible hierarchical distributed system based on Linux PCs, VME crates and boards, detector integrated readout systems and standard communication links like Ethernet, USB and optical fibers, schematized in Fig. 5.1.

The steering of the acquisition is managed by the Storage PC (located in the experimental room) which is controlled by the Control PC via remote connection. The Storage PC is equipped with two network interfaces allowing it to connect both with outside and with the internal network. The latter is a self-standing network connecting the whole acquisition system in which data are actually transferred during the run.

The main network node is an Ethernet switch with 24 1GbE, 2 10GbE and 2 10GbE SFP+ ports. As shown in Fig. 5.1, both the Storage PC and the NAS are connected through 10 GbE (red wires) while all the other devices are connected through 1 GbE (blue wires). The switch is used to collect all the data from the detectors: namely, 20 DE10nano or DE10 Terasic boards for the tracking system and the WaveDAQ for the Start Counter, ToF Wall and Calorimeter. In addition, a dedicated fiber link connects directly the Storage PC with the VME crate which hosts the V2495 board (i.e. the trigger board) and the electronics (TDC and discriminators) for Beam Monitor reading. This is achieved using the CAEN V2718 board, a VME optical link bridge able to read/write data from/to VME boards.

Besides that a third desktop computer, the Monitor PC, is dedicated to monitor the

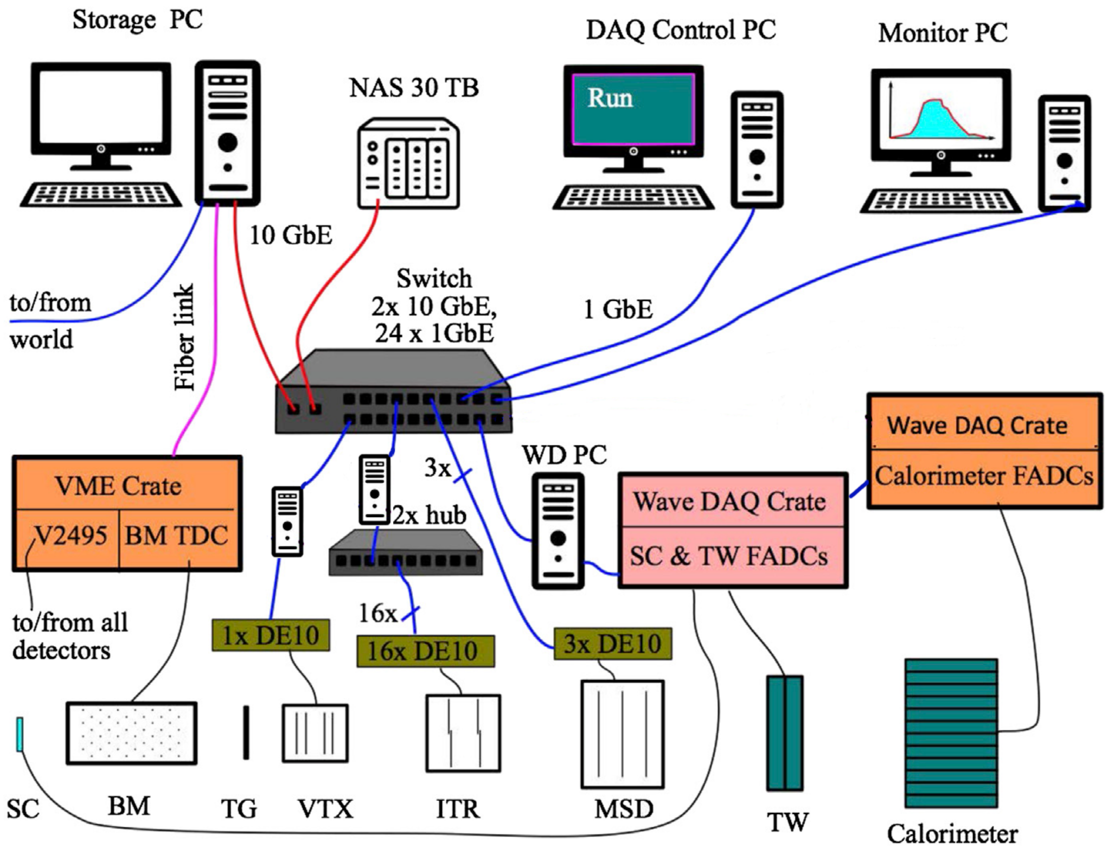

Figure 5.1: DAQ logical scheme. Adapted from [51].

acquisition and to perform some manual operations if needed.

5.4 General concepts of Data Acquisition

In a experiment with multiple subdetectors, it is crucial to assure that data are acquired only when all detectors are ready to, otherwise events could be incomplete or potentially mixed up. In order to do so, a *busy logic* has to be implemented: the busy is a condition which inhibits the generation of a trigger signal. This is necessary to allow the system to properly process the event and to allow detectors to get ready for the next event.

All busy signals, in addition to trigger, in the FOOT experiment are managed by the central trigger board, i.e. the CAEN V2495 board, a general purpose programmable FPGA and I/O unit hosted in the VME crate. The board receives busy signals from all the detectors and performs their logic OR: if at least one detector is not ready to take data, no trigger will be issued even if generated by the WaveDAQ. The busy time length can vary from event to event even if most of FOOT detectors have it fixed (excluding variable timing to empty buffers): as already said, the slowest detector is the Vertex detector.

In modern experiment design, the processing of events is completely decoupled from events themselves. This means that the system is able to acquire an event even if the previous one is still in process. Indeed, calling τ the *deadtime* of the system, i.e. the time needed to fully process an event (until its storage on disk) during which the system is not able to accept an event, f the frequency of the physics event (in FOOT it could be a beam particle passing through the Start Counter) and ν the DAQ output rate, i.e. the real acquisition rate, the probability to find the system ready to acquire data is $1 - \nu\tau$. Hence, $\nu = f(1 - \nu\tau) = f/(1 + f\tau)$ descending that the DAQ rate is always smaller than physics rate as well as efficiency, i.e. the ratio between the number of recorded events and their total number, will be below 1.

The loss in efficiency can be dramatic since, given a mean physics rate $f = 1\,\mathrm{kHz}$ and $\tau = 1\,\mathrm{ms}$, the efficiency drops to 50% as reported in Fig. 5.2. Even though this is true for stochastic process, e.g. radioactive decays, it works also during data taking in beam facility where a mean rate can be defined even if the instantaneous rate could be much higher given the time structure of synchrotron beams. Since the design of a system with minimum deadtime can result in high costs as well as some technical constraints cannot be overcome, the solution is to decouple the event receiving and data processing using buffers to absorb input rate fluctuations and to make the data processing more deterministic, thus reducing the probability to find the system busy. This approach is called *de-randomisation* and it can be achieved using a huge number of buffers in which multiple events are stored and read at constant time intervals. Buffers have to be placed in the whole DAQ chain and their depth has to be tuned according to DAQ rate and event size. In this scenario, busy signals are needed to inhibit the insertion of further

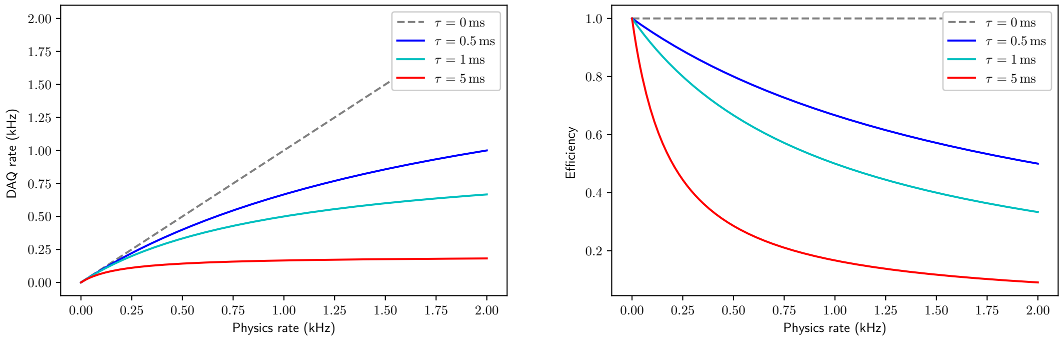

Figure 5.2: DAQ output rate versus input physics rate (left) and efficiency versus input physics rate (right) with different dead time τ.

data if the buffers are full or almost full so that the system can empty them by reading data.

Since buffers are spread throughout the system, it is important that, if a buffer gets full, it is able to propagate its busy also to upstream systems: this is called *backpressure*.

Another critical topic in data acquisition when a lot of detectors are involved is the time synchronization. Indeed, DAQ system has to assure that event fragments collected by all the detectors belong to the same physical event. The redundancy on timing information is of utmost importance since some critical points arise: for instance, if a detector fails to get even only one trigger signal, it loses the time alignment until the end of the run. In order to prevent any problem of this kind, in FOOT TDAQ system the V2495 board continuously generates a 1 MHz signal, called Timestamp clock (TS clock) distributing it to all the detectors: in this way, they can sample it and can write its value in the event payload. The alignment can be monitored in real time resulting in a very useful tool possibly also for offline synchronization.

5.5 The FOOT TDAQ infrastructure

The FOOT TDAQ system is based on ATLAS TDAQ system [57] and a lot of work was needed in order to adapt it to the FOOT experiment given several differences between the experiments.

The TDAQ system of the FOOT experiment has to accomplish different tasks: it has to ship data from the detector to mass storage, to control and monitor the whole experiment and to handle the trigger and busy logic.

One important part of TDAQ is the *Online Software*. The Online Software encompasses the software to configure, control, and monitor the TDAQ system but excludes the management, processing, and transportation of physics data. It is a customizable framework which provides essentially the *glue* that holds the various sub-systems together and it does not contain any detector specific element, thus allowing to handle any kind of detector together with monitoring devices. An important task of the Online Software is to provide services to drive the TDAQ through its startup and shutdown procedures so that they are performed in an orderly manner. It is responsible for the synchronization of the states of a run in the entire TDAQ system and for process supervision.

The Online Software architecture is composed by several layers and the highest, which is the one interacting with the final user, consists of three high-level services:

- *Control*, which is responsible to handle the control of the TDAQ system and detectors. Control sub-packages exist to support TDAQ system initialization and shutdown, to provide control command distribution, synchronization, error handling, and system verification.
- *Configuration*, which contains sub-packages for configuration of the TDAQ system and detectors. Configuration sub-packages exist to support system configuration description and access to it, record operational information during a run and access to this information. There are also boundary classes to provide read/write access to the conditions storage.
- *Monitoring*, which provides all the utilities to monitor the state of the acquisition performing some quick operations. This is of utmost importance during data taking since it is possible to check the detector alignment in real time as well as to monitor important quantities.

These high-level services lay on an intermediate software layer called *Inter Process Communication* (IPC) which is an API for the communication middleware based on CORBA. CORBA is the acronym for *Common Object Request Broker Architecture*, the OMG's [58] open, vendor-independent architecture and infrastructure that computer applications use to work together over networks. Using the standard protocol IIOP, a CORBA-based program from any vendor, on almost any computer, operating system, programming language, and network, can interoperate with a CORBA-based program from the same or another vendor, on almost any other computer, operating system, programming language, and network [59].

5.5.1 Control

The high-level operation of the data acquisition and the relation with the different sub-systems are described in terms of the behaviour model of a *finite state machine*. Namely, the TDAQ can be only in one state at a time from which it can reach only a specific group of states as depicted in Fig. 5.3. Regarding FOOT TDAQ states are as follows:

Figure 5.3: DAQ finite state machine.

- *initial*, this state represents the case when TDAQ sub-systems are started up but idle. It is the earliest state in which it is possible to send commands directly to the TDAQ control elements. The only operations which are allowed are those which bring the overall system to a situation where data-taking can be performed. The TDAQ system may also revert to this state in order to perform some critical or manual operations.
- *configured*, in this state the TDAQ system is ready, to initiate a data taking session. This means that the various components have been properly initialized. In particular, all the configuration parameters for all the detectors are sent successfully to different subsystems. These parameters, including trigger logic and detector-specific configurations, are stored in the main TDAQ PC and they are written in the offline database.
- *running*, in this state the TDAQ system has enabled trigger generation, busy logic and is taking data.

All the transitions are considered to be successful only if all subsystems in the acquisition are able to complete their own operations without errors. In particular, both the configure and the start transition are quite critical since the former involves register writing and opening connections (see below) while the latter brings all the systems in run modality.

5.5.2 Configuration

Configuration is a delicate step in the FOOT TDAQ workflow. It involves opening communication with all detectors, sending configuration for the forthcoming run and assuring the success of this setting. Almost all configuration parameters are stored in the main TDAQ computer, keeping the local configuration as little as possible, in view of a better database storage and clarity.

The configuration of detectors and their information is implemented using *Object Kernel Support* (OKS): it is a library to support a simple, active persistent in-memory object manager. It is suitable for applications which need to create persistent structured information with fast access but do not require full database functionality [60]. OKS is equipped with a C++ API allowing a full integration with the software: indeed, this library is able to generate C++ classes with members and methods which can be used in the TDAQ software.

In FOOT TDAQ this tool is used both for configuration and for monitoring and its user interface is implemented using standard XML files. These files can be tailored to each detector including a lot of data types, strings, vectors and numerical values which can be modified on run basis even while the infrastructure is up. These parameters are then gathered in the TDAQ software to be routed to detectors during *configure* transition or to be continuously monitored during acquisition.

5.5.3 Monitoring

A lot of parameters have to be monitored during data acquisition: among them, hardware and software system status, buffer occupancies and sensor temperature. Moreover, checking correlation and synchronization among detectors is an important part of real-time data quality while online plot of physical quantities can provide useful information even for detector alignment as several experimental facilities are not able to monitor ion beams at low rates required by the FOOT setup. Eventually, another important aspect of the monitoring framework is the error reporting which allows to identify any faulty part or process in the experiment and to promptly cope with it.

In the FOOT TDAQ distributed system it is necessary to transport the monitoring information from the places where it is produced to the places where it can be processed: this task is accomplished by the IPC which is common to all Online Software services and in monitoring framework itself. This means that information can be shared among all the acquisition devices regardless of their location and of operating system on the hosting machine: moreover, IPC is compatible with object-oriented languages allowing the use of both Java and C++ languages [61].

The monitoring framework is capable to handle different data types such as events or event fragments, statistics information, which reflect the operation of the hardware elements and software processes in the system, and errors which can be detected at different levels of the system. These types are significantly different in terms of data size, update frequency and type of access as shown in Tab. 5.1 [62].

The main monitoring tasks are divided into several services: the *Information Service* (IS) allows TDAQ applications to exchange user-defined information during a run using custom structure defined with OKS. In this way, it is possible to monitor run conditions, buffer status and important counters throughout the run. A graphical user interface which allows to browse the content of the IS is also provided.

The *Event Monitoring System* (EMS) is responsible for transportation of physics events to the software applications which can analyze them in order to monitor the state

Type	Format	Production	Access
Samples of physics events	Vector of 4-byte integers	On request	On request
Errors	ID+Severity+Text	In case of faults	Via subscription
Histograms	ROOT histograms	Periodically or when changes occur	On request and via subscription
Other information	User-defined (e.g. objects)	Periodically or when changes occur	On request and via subscription

Table 5.1: Monitoring data types [62].

of the data acquisition and the quality of physics data of the experiment [62]. The EMS can run in parallel with the main data taking at a custom rate: the maximum rate is set in such a way not to affect main acquisition.

The *Online Histogram Service* (OHS) allows applications to exchange ROOT histograms: from the implementation point of view it is a specialization of the IS which includes also a graphical interface (the *Online Histogram Presenter*, OHP) to browse the content of histograms as in ROOT files. These histograms are filled at each event and their number should be kept at minimum not to weigh down the data acquisition workflow.

Another online monitoring tool widely used in FOOT TDAQ is GNAM. GNAM is a modular framework where detector specific code can be easily plugged in to obtain online low-level monitoring applications [63]. GNAM is divided into two parts depicted in Fig. 5.4: the Core and the detector plugins. The Core handles the common actions, while detector specific code is implemented in the plugins.

The Core is responsible for asking event fragments to the EMS and unpacking them, ending up with a list of detector fragments without any decoding which is a task of each plugin. This is up to each plugin which in FOOT TDAQ share common classes for offline decoding of raw data: this choice guarantees a good compatibility and a smooth operation.

The decoded data are then collected back by the Core and provided to the histogramming plugin, where they are analyzed and used to fill histograms. The aim of having all the data decoded before calling any histogramming routine is to allow correlation histograms. Indeed, as every histogramming function can access all the decoded data, it is easy to study the correlation of different detectors, with separate plugins, without duplicating the effort of decoding the raw data. This is an important feature of GNAM since it allows, as said before, to combine information from several detectors thus monitoring time alignment, detector alignment, beam shape and position and trigger information.

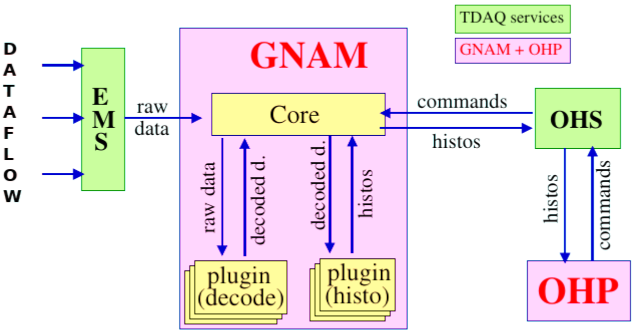

Figure 5.4: Schema of the GNAM and OHP monitoring chain. Adapted from [63].

The Core is also responsible for publishing the histograms on the OHS. GNAM was successfully implemented in FOOT TDAQ during these years and it was successfully tested in a test beam in Proton Therapy Center in Trento in view of the data taking performed at GSI in July 2021. In that context, GNAM was able to provide fundamental information about the beam and the status of the detectors and to provide a quick feedback on the detector alignment. Moreover, it supplied necessary information to successfully tune the fragmentation trigger used in physics runs.

5.6 Detector implementation

As said before, FOOT setup is composed by several types of detectors which have to be implemented in the overall setup. From DAQ standpoint, two different types of detectors are present: remote detectors and VME boards. While the latter were entirely developed and maintained by TDAQ group, from data generation to event building, the former result from a common effort with detector experts.

5.6.1 Remote detector implementation

In FOOT we developed remote detectors according to client-server model for the connection and consumer-produced model for the data flow. As depicted in Fig 5.1, all detectors are connected through Ethernet and a communication protocol has to be established. We chose to use *Transmission Control Protocol* (TCP), a widely-used reliable protocol for network communications. Indeed, unlike other protocols, TCP requires an existing connection to work and it provides reliable, ordered, and error-checked delivery of a data stream, thus preventing also data losses due to network congestion which can occur.

The code was developed starting from GNU C library tools, namely from sockets and communication protocols. In the client-server model, DAQ storage PC plays the role of

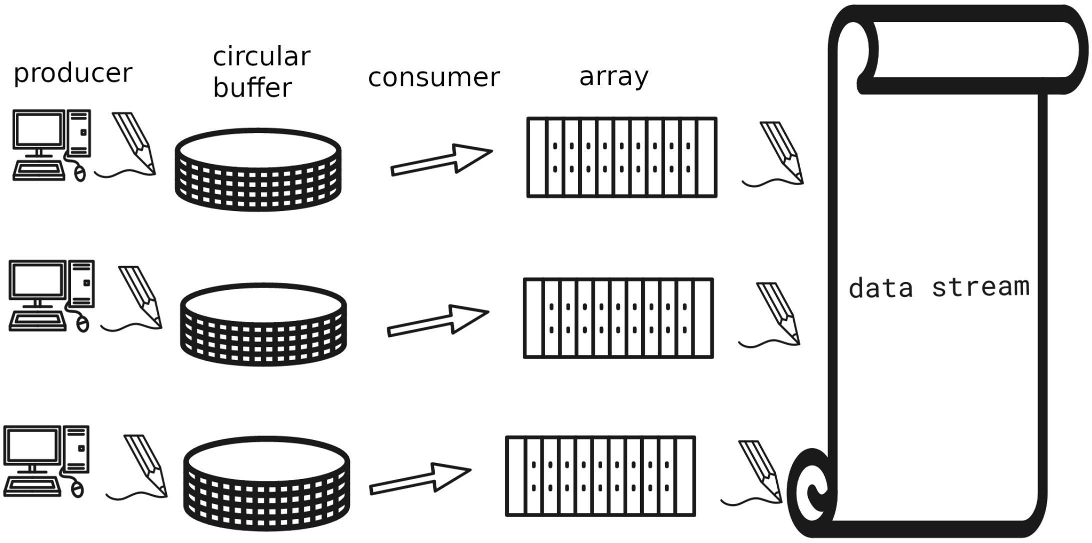

Figure 5.5: Drawing of producer consumer model.

the client while remote devices are data servers: this is not a standard network design since these are all one-to-one connections. However, this design allows a high flexibility and it proved to run smoothly with our number of devices.

Starting from those libraries, we developed two classes describing two different connections: the *slow* connection is designed to send initial configuration to remote detectors (see Sec. 5.5.2) and to handle continuous monitoring during the run (see Sec. 5.5.3). The *fast* connection is designed to send data and is by far the most critical: indeed, as set out in Sec. 5.4 it is not feasible to process and store one event at a time thus the presence of buffers in the whole system is required. Buffers have to be implemented also for remote detectors but they are shared between two processes, one reading the buffer and one filling it. The access to these buffers has to be synchronized in order to avoid undefined behaviour: this is known as *producer-consumer* problem.

This is a typical multi-process synchronization problem in which two cyclic and parallel processes, a producer and a consumer, share a common buffer which is continuously filled by the producer (i.e. remote detector) and emptied by the consumer (i.e. main DAQ PC). Moreover, the consumer itself has to synchronize read/write operations in its buffers with the main data stream.

The critical point is to guarantee that no simultaneous access to the same memory areas occurs during the run: such a condition can be prevented implementing *thread synchronization*, a mechanism ensuring that two or more concurrent processes or threads do not perform critical operations at the same time. Unlike standard functioning, the access of processes is constrained using synchronization techniques whose basics tools are

Posix, mutex as provided by the Boost library. When one thread starts executing the critical section (for example read/write operation) the other thread should wait until the first thread finishes. If proper synchronization techniques are not applied, it may trigger a so-called race condition where the values of variables may be unpredictable and vary depending on the timings of context switches of the processes or threads.

As depicted in Fig. 5.5, circular buffers and arrays are shared by concurrent processes: in particular, circular buffers are a common resource for producer and consumer while arrays are shared among consumer processes. The designed system was able to run without problems during the 48-hour long run at GSI in July 2021 with five server-client connections. Its performances will be outlined in the next section.

5.6.2 Beam monitor implementation

As set out in Sec. 5.5, the FOOT TDAQ architecture contains also VME electronics. In particular, the VME crate hosts both electronic boards for acquisition and custom boards for signal distributions and it was entirely developed by the DAQ group: namely, CAEN boards on VME are the V2495 trigger board and the V1190B Multihit Digital TDC for the beam monitor readout.

From DAQ standpoint, the beam monitor acquisition consists of the readout of 36 channels. Unlike other detectors, the only information stored for beam monitor is the time of fired channels since it can be translated into a space information. The time accuracy for this detector is particularly critical since it needs to measure the drift time without jitters: for this reason we designed a patch panel to distribute signals with the possibility to forward some copies of candidate trigger signals from the Wavedream system without waiting for V2495 board. In this way it is possible to avoid the jitter introduced by the sampling rate of the trigger board.

Regarding TDAQ infrastructure, VME boards are treated in the same way of remote detectors: however, there is no need to establish TCP connections since the communication between the DAQ and VME boards is handled by CAEN libraries. The VME crate is directly connected to the main DAQ PC through the V2718 CAEN bridge which is responsible for read/write operations on VME boards: once properly configured, it is totally transparent for the general acquisition as the TDAQ system is able to communicate with single boards.

We set up the beam monitor configuration and readout from the very beginning, integrating it into the TDAQ system. Firstly, the trigger configuration had to be tune according to our needs, in particular the width of the search window in which triggers can be collected. Then, busy condition for TDC had to be defined: the final choice was to send TDC in busy status if main data buffer is almost full. In this way, the generation of triggers is inhibited until TDC buffers are emptied by event readout. In the attempt to remove any bottleneck from our system we focused on VME data readout: even though VME is a well-proven standard offering mechanical, electrical and protocol standards, it can be slower with respect to other custom electronics. Indeed, single read cycle can take up to 1 μs to complete resulting in a maximum rate of 4 MB/s. For this reason we successfully implemented data reading using *block transfer* (BLT), a particular protocol based on single cycle which can increase the transfer rate up to 40 MB/s with 32-bit words. We also take advantage from TDC buffers by developing a fast read mode: in TDC module an event FIFO is introduced in order to help the event readout from the data buffer, since the size of the events is unknown *a priori*. When the event FIFO is enabled, once an event is written in the data buffer, a 32-bit word containing the event number and its size is written also in the event FIFO. In this way it is possible to transfer a bunch of TDC full events and to unpack them at a later time to build the actual DAQ event. This reading mode worked successfully at GSI without problems: the speed up in acquisition rate can be observed in the next section.

As for other detectors, online monitoring for the Beam Monitor was developed as well. Besides timing information, two heatmaps (one for each view) of hit channels are provided in GNAM and they were very useful in experimental scenarios in order to align the detector with the beam.

5.7 Performances

The performances of the developed TDAQ system were evaluated using two different input sources and different configurations. In particular, tests were carried out both with a pulser and a beam simulator as trigger sources. In the TDAQ setup, a DE10 nano simulating a Micro Strip Detector tracking station (X-Y planes) was switched on and off as well as the aforementioned BLT for VME boards readout. The DE10 nano board acts as a proxy for all the remote systems since these detectors share the same DAQ readout architecture. As already stated, in FOOT TDAQ system the processing of events is completely decoupled from events themselves thanks to the presence of buffers in the whole system. This means that it is possible to analyze DAQ performances using the concepts introduced in Sec. 5.4. In particular, in the first test I analyzed the response of the system with a periodic trigger signal generated by a Keysight Technology 33600A Series Waveform Generator: the signal was shaped according to TTL standard ($V_{\text{low}} = 0\,\text{V}$, $V_{\text{high}} = 3.3\,\text{V}$, width $= 100\,\text{ns}$) which was forwarded to V2495 board as trigger signal. Several frequencies were examined in the range 100 Hz − 5 kHz and the mean DAQ rate was evaluated.

In Fig. 5.6 the real acquisition rate under different configurations with respect to the physics rate, i.e. the pulser frequency, is reported. The red curve was acquired including both the TDC for beam monitor readout and the DE10nano simulating a MSD tracking station while for the red and the green curve the DE10nano was disabled. Moreover, in the third configuration (green curve) also BLT on VME bus was disabled. Using a pulser a step-like behaviour is expected since the curve should be linear up to

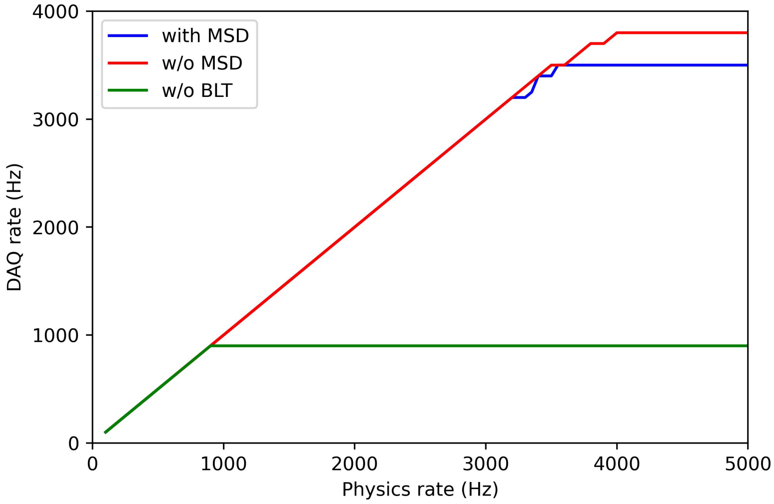

Figure 5.6: FOOT TDAQ output rate versus input physics rate with pulser trigger with MSD and BLT on (blue), with MSD off and BLT on (red) and with MSD off and BLT off (green).

a well-defined frequency value corresponding to two consecutive triggers closer than the minimum busy length of the system. Data in Fig. 5.6 agree with this picture: with DE10nano board included the maximum rate is as high as 3.5 kHz while without it the rate reaches 3.8 kHz. This difference suggests that the DAQ overhead increases when a new type of detector is included in the acquisition. Indeed, this rate reduction is not due to the MSD readout system since it showed to be able to keep a data rate as high as 20 kHz when other detectors are not present. In particular, since a DE10nano event has a variable number of words in this configuration (maximum 250, mean 142) it is possible to find a maximum throughput of 10 MB/s in the best case scenario although DE10nano boards are connected via 1 GbE. This 10-fold reduction is due to an out-of-date firmware version limiting the maximum rate at 100 Mb/s: even if this drop will not constitute a bottleneck for the whole system given FOOT lower rates of acquisition, the firmware upgrade is foreseen for the next future. Moreover, a large difference between red and green curves can be observed: this is due to the speedup of block transfer on VME crate: rather than reading one word at a time from V2495 and V1190, data are transferred in bunches. Without this development, the maximum DAQ rate would fall to 900 Hz, well below the experiment requirements.

The second type of test was carried out using a beam simulator as trigger source instead of a pulser. As already stated in Sec. 5.4, the time structure of synchrotron beams can mimic a stochastic process such as a radioactive decay: indeed, it is possible to define a mean rate even if the instantaneous rate can undergo great variations and it can significantly affect DAQ efficiency. For this reason, a beam simulator was implemented in another DE10nano board developing a completely different firmware for the FPGA.

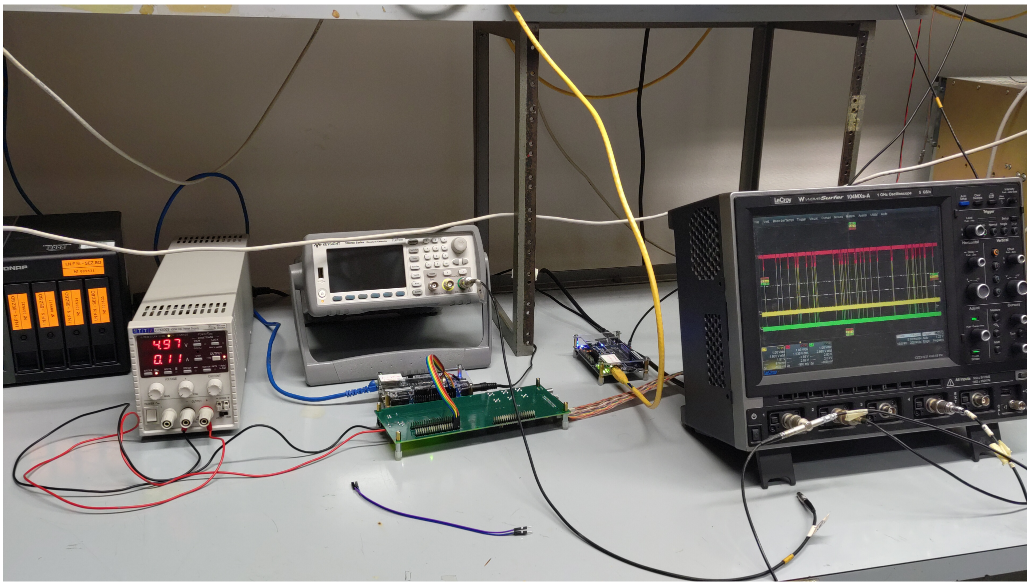

Figure 5.7: FOOT TDAQ setup for tests. The DE10nano board with the yellow cable provided the beam-like trigger while the board with blue cable was the simulator of the MSD readout system. On the oscilloscope beam signals are in yellow, trigger issued by the V2495 in green and the busy of the experiment in red.

A picture of the setup used for the following test is reported in Fig. 5.7. To simulate beam time structure, a time bunch of 8 s is divided into 20 non-equal parts. Each part has a different predefined intensity which can be multiplied by a common factor to tune the overall mean rate. This time structure is based on the Oxygen beam we observed in April 2019 at GSI. The multiplicative factor can be set without switching off the board by writing an FPGA register and can take two parameters a and b in the form $f(\mathrm{kHz}) = a + b \cdot 16^{-1}$ where $0 \leq a, b \leq 15$.

For a better evaluation of DAQ performances in this context, I decided to plot the efficiency, i.e. the ratio between recorded events and their total number, with respect to physics rate. These values were calculated using the V2495 information stored in the MySQL database: as a matter of fact, the V2495 trigger board is able to count both trigger candidates regardless of the busy status (*bare* counter) and the actual number of issued triggers (*gated* counter). This means that, knowing the total duration of the acquisition, it is possible to evaluate both the mean rate, as the ratio between bare triggers and total duration, and the efficiency, i.e. the ratio between gated and bare triggers. The results of the frequency scanning, from 60 Hz to 6 kHz, is reported in Fig. 5.8.

As it can be observed, no significant difference are present between the two setups (with and without MSD) as both curves undergo a loss in efficiency until 30% at 6 kHz. This means that, to enhance the recording of interesting events reducing the data taking

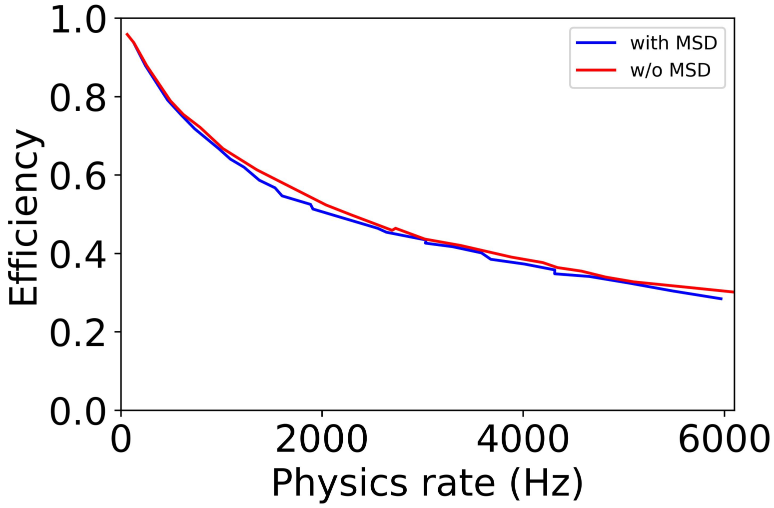

Figure 5.8: FOOT TDAQ efficiency versus input physics rate with beam simulator trigger with MSD on (blue) and with MSD off (red).

time, it is mandatory to employ the fragmentation trigger which cuts *a priori* the most of minimum bias events.

Chapter 6

First analysis of GSI 2021 data

In July 2021 the FOOT collaboration had the possibility to perform measurements on beam at GSI in Darmstadt. We requested ^{16}O beam at two different energies, 200 MeV/u and 400 MeV/u which were delivered in a non-stop run of more than 48 hours. At the end, from TDAQ standpoint we collected more than 40 millions events in various configurations with two different targets, Carbon and Polyethylene. A preliminary analysis on a subset of data (400 MeV/u ^{16}O + C) is presented in this Chapter. Firstly, the FOOT setup at GSI and the detectors considered in the analysis are presented. Then, MC performance studies and efficiency evaluation together with a description of the software output are outlined. In preparation of the event reconstruction, the detector alignment was performed and verified carefully. Eventually, preliminary results on elemental fragmentation cross section, both total and angle differential of selected runs will be presented.

6.1 The FOOT GSI setup

The data taking of July 2021 at GSI involved a reduced apparatus of the FOOT electronic setup. Indeed, since the magnets, the Inner Tracker (IT) and the full Calorimeter (CALO) will be available in 2022, the setup was composed by the Start Counter (SC), the Beam Monitor (BM), the Vertex Detector (VTX), the Micro Strip Detector (MSD), the ToF Wall (TW) and one module (9 crystals) of the CALO. This means that there will not be possible to measure the momentum of the fragments with this setup and that a hint on the fragment mass can only be provided by the CALO, even if with limited angular acceptance. All the subsystems ran smoothly and they were able to acquire data all the time: however, as the calibration and fine alignment machinery have not completed yet, the following analysis included only the SC, BM and TW.

Since feedback from tracking detectors is not considered in this analysis, the out-of-target fragmentation cannot be actively removed but it has to be evaluated in dedicated runs without target.

6.2 Software

The software framework developed for the FOOT experiment is called SHOE (Software for Hadrontherapy Optimization Experiment): it is an entirely C++ custom software based on ROOT [64] framework including external libraries for specific tasks (e.g. GENFIT for track reconstruction [65]). It is maintained and developed by the FOOT collaboration using a git repository provided by INFN. The software is designed to take care of all reconstruction steps, both for MC simulations and real data, for all subsystems. Indeed, several steps are needed to analyze data and many of them are common to simulation and data.

6.2.1 Simulation

The FOOT Monte Carlo simulation was built using two different frameworks (partially integrated in SHOE) among those used in nuclear and particle physics: FLUKA [66] and GEANT4 [67]. In the workflow of both frameworks, several steps can be identified:

- a detailed description of the experimental setup, namely of the geometry and materials to correctly evaluate interactions in active detectors and fragmentations has to be provided and checked against the description used for the reconstruction step;
- the MC code generates beam particles and their transport, scoring energy losses, nuclear interactions and secondary particle production together with their kinematic quantities such as momentum, velocity, initial and final position;
- all the results are stored in ROOT format for following reconstruction and analysis.

6.2.2 Reconstruction

After simulation step, MC ROOT files become SHOE inputs. The full event reconstruction proceeds in steps: at the beginning, MC and raw data, i.e. data written in binary format by FOOT TDAQ system presented in Chap. 5, follow different paths. Indeed, MC data undergo a digitization process: when a particle crosses a detector, it is needed to model and simulate the response on the detector. For example, given the charge and the velocity of a particle from the simulation, it is possible to evaluate the number of pixels (strips) fired in the VTX (MSD) detector. From that point on, MC and real data follow roughly the same path, except for calibration routines, to keep to a minimum unexpected behaviours. Starting from the decoding of the MC or real data information

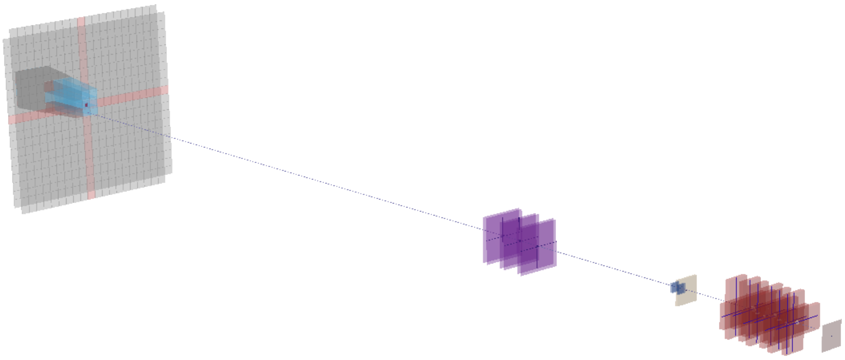

Figure 6.1: A screenshot of the FOOT event display for the GSI2021 setup. From right to left: SC, BM, target, VTX, MSD, TW, CALO.

the different subdetectors process the information and more complex objects are built in a sequence of actions. For instance, the following operations include pixel clusterization, combinatorial track finding and vertex position evaluation for VTX, strip clusterization for MSD, signal processing and charge identification for TW (see below).

The output of the event reconstruction is again a ROOT file containing histograms and/or trees according to users' needs: it is possible to include a partial reconstruction requiring only a subset of the detectors to save space and processing time. In order to properly configure the framework to handle different data and MC relative to different data taking or test beams and to use the proper calibration and configuration files when processing a given subset of runs in a given context, a *campaign manager* has been developed. When the decoding chain is launched, the software loads the corresponding files. Moreover, an event display is available to perform geometry and tracking checks (Fig. 6.1).

6.2.3 Charge identification with TW detector

As set out in Chap. 4, charge identification in the electronic setup of the FOOT experiment is an exclusive task of TW. Indeed, the TOF system (SC and TW) can provide both the Time of Flight T_{tof} and the energy loss ΔE: these quantities are related to the particle charge according to Bethe Bloch (BB) equation (Eq. 1.3) already presented in Chap. 1.

Given the slight dependence of T_{tof} (i.e. β) on the path length of the fragment, charge information can be used as a seed for the final track reconstruction [65]. In SHOE, the charge identification algorithm harnesses the mentioned BB relation using the $\Delta E - T_{\mathrm{tof}}$ plot. Firstly, the MC simulation is compared with data to correctly reproduce T_{tof} and ΔE in the given setting and to perform the detector calibration. Then, the algorithm is

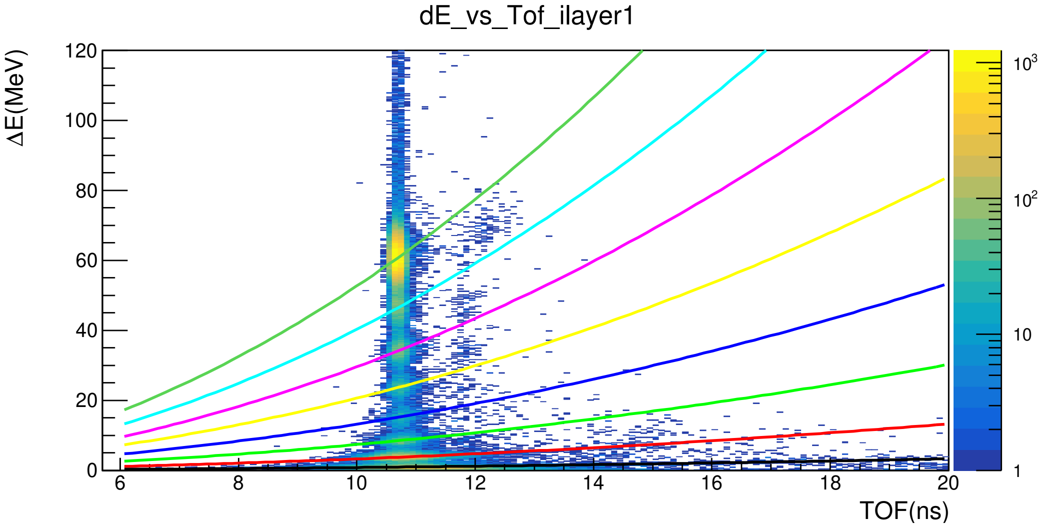

Figure 6.2: $\Delta E - T_{\text{tof}}$ plot of fragmentation run of GSI2021 campaign using BB curves.

offline tuned on MC data tailoring BB curves to different charge regions.

In Fig. 6.2 the $\Delta E - T_{\text{tof}}$ plot for a fragmentation run of GSI2021 campaign is drawn. It is possible to see eight regions corresponding to different charges (from $Z = 1$ to $Z = 8$) together with the superimposed BB curves in the interesting range. Once the curves are drawn, to each point in the plot the charge of the closest curve is assigned. Since at these energies fragments lie in the β^{-2} region of BB equation, given the relation between T_{tof} and β, the curves are proportional to T_{tof}^2.

Energy loss and Time of Flight were previously calibrated using dedicated runs. In particular, TOF calibration was performed using a dedicated run in which the SC was moved next to the TW. Moreover, the latter was moving thanks to an electric engine allowing to scan all the detector positions. In this way, delays due to electronics and cables can be evaluated. Regarding energy calibration, organic scintillators follow the Birks' law [68] and multiple energy loss points are needed for a proper calibration. Since the scan was performed only with 400 MeV/u ^{16}O ions, other data were gathered from produced fragments. As fragmentation spectrum is peaked at the projectile energy (as stated in Sec. 2.5.1), it is possible to use identified fragments as calibration points as they will mostly populate different values of ΔE lower than that of the primary beam.

Eventually, TW time performances allow to calculate the hit position along the bar by looking at the time difference between the signals at the two ends of the bar. This method allows to reach a higher precision compared to the simple bar superposition (a few mm vs 2 cm): however, the former method is still in its tuning phase and it was not employed in this analysis.

The aforementioned charge identification algorithm is independently applied to both TW layers: then the matching algorithm aims to put together those hits thought to be-

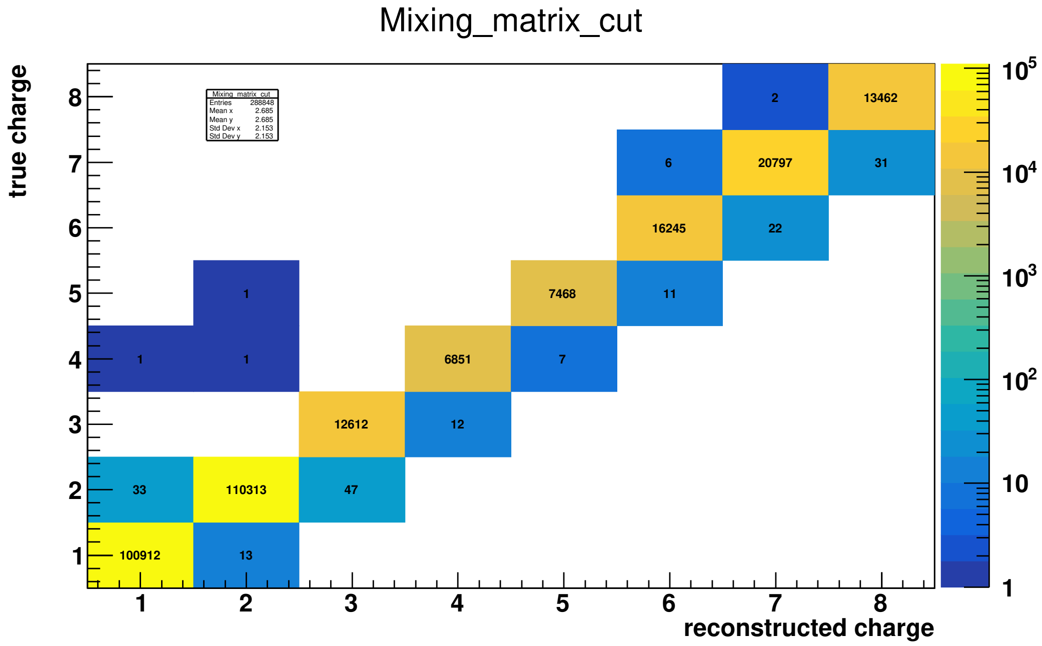

Figure 6.3: Charge mixing matrix from MC simulation.

long to the same particle by looking at their energy releases and positions. However, the clustering algorithm can suffer both from pile up in a bar and from fragmentation within the detector itself. For the following analysis, only matched clusters were considered even if this can cause a drop in efficiency.

6.3 MC simulation

The first step of the analysis was the processing of Monte Carlo simulations. To this end, 5×10^6 400 MeV/u ^{16}O primaries on C target were analyzed. Although usually FOOT simulations are *triggered*, i.e. only fragmentations events (a few %) are saved, this time only untriggered simulations for trigger studies were produced.

Firstly, only interesting events were selected: this was achieved requiring fragment produced by the primary particle in the target and that it was able to exit. Indeed, out of target fragmentations are very frequent and they can be an important source of background (see below).

The charge identification algorithm was tested on MC data requiring that the estimated charge in both layers was the same. The Charge Mixing Matrix (CMM) is reported in Fig. 6.3. It is worth underlining that the algorithm works very well in this context even if the constraints on matching hits can lead to a lower efficiency. The CMM was filled with reconstructed TW points generated by fragments with a kinetic energy in the $100 - 600\,\mathrm{MeV/u}$ range and produced within 1 cm from the target center. The main information to extract from MC data are detection efficiencies for cross section calculations. In this context the efficiency was measured as follows [69]:

$$\varepsilon(Z) = \frac{N_{\mathrm{TW}}(Z) + 1}{N_{\mathrm{track}}(Z) + 2} \tag{6.1}$$

where $N_{\mathrm{TW}}(Z)$ are the fragments with charge Z correctly reconstructed by the TW produced by primary particle in the target and $N_{\mathrm{track}}(Z)$ are the fragments generated by MC escaping from the target within the TW solid angle.

To not depend on fragmentation models in MC for the efficiency evaluation, for all MC analysis only fragments produced in the target were considered excluding secondary fragmentation outside the target. To extract N_{TW}, the number of TW points satisfying the same conditions of N_{track} were counted for each Z. Moreover, to not depend on the charge identification algorithm efficiency (even though it results to be high) N_{TW} were considered taking the true charge. This means that reconstruction efficiency should account for acceptance (both angular and in kinetic energy), intrinsic detector efficiency and clustering algorithm reconstruction efficiency. Errors on the efficiency were calculated using Bayesian formula as follows:

$$\epsilon_{\varepsilon}(Z) = \sqrt{\varepsilon(Z)\frac{N_{\mathrm{TW}}(Z) + 2}{N_{\mathrm{track}}(Z) + 3} - \varepsilon(Z)^2}. \tag{6.2}$$

In Fig. 6.4 total efficiencies integrated in angle and kinetic energy are shown. All the efficiencies range from 70% to 85%. These values are compatible with the strict requirement of Z matching and with a limited handling of pile up events: thus, there is still room for improvement in the next future.

In Fig. 6.5 angular efficiencies divided per charge are reported. The binning choice is based on the granularity of the TW: as stated before, no position calibration was implemented in this analysis so that the resolution of TW position is 2 cm. The granularity is defined by the square area resulting from the crossing of one bar in the front and one in the rear layer and it corresponds to $\approx 10\,\mathrm{mrad}$ for the TG-TW distance as measured at GSI ($\approx 193\,\mathrm{cm}$): as VTX and MSD are not included in this analysis the emission angle of the fragment will be evaluated with TW itself.

As it can be seen in the figure, low-Z fragments efficiencies increase with increasing angle. This is due to the fact that with this setup low-Z fragments are present in events with higher multiplicity and pile up in the same bars plays an important role in spoiling the signal if tracking detectors cannot remove the ambiguities. For high-Z fragments MC efficiency appears to be more constant.

No kinetic energy efficiencies are reported since, with the available detectors in GSI setup, it is not possible to extract such kind of information except from fragments in the central part of TW. This will require a careful calibration of calorimeter crystals.

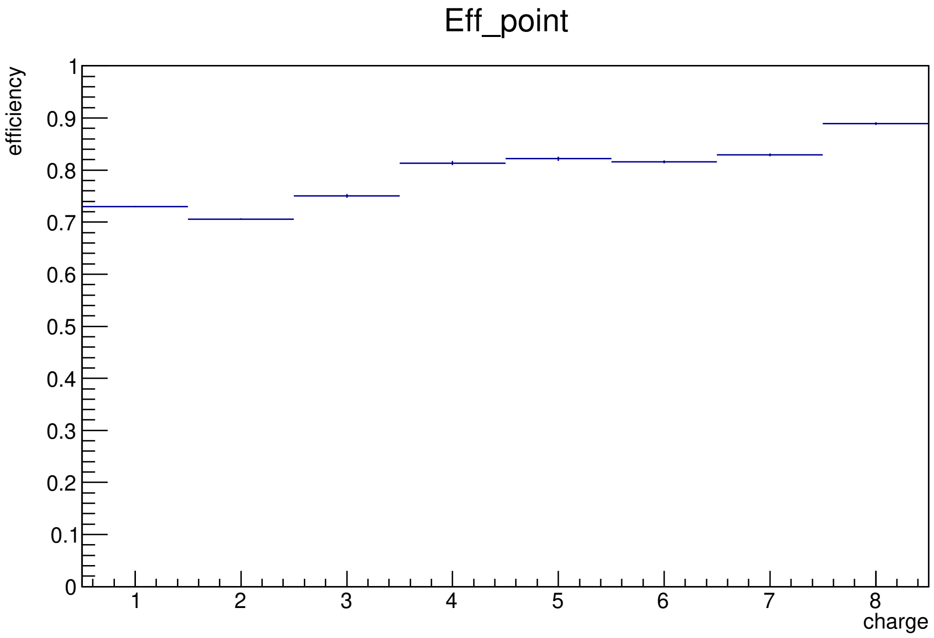

Figure 6.4: Fragment identification efficiency vs fragment charge (Z) from MC.

6.4 GSI data

In the GSI2021 data taking we collected more than 40 million events using Carbon (C) and Polyethylene (C_2H_4) targets with ^{16}O beam at 200 and 400 MeV/u.

In Table 6.1 the list of physics runs used for this analysis is reported: in all these runs the beam energy was always set to 400 MeV/u.

Both minimum bias and fragmentation trigger runs were selected together with a minimum bias run without target, all taken under stable beam and setup conditions. Given the number of files to analyze, all the analysis was carried out using the High-Performance Computing (HPC) infrastructure built by the GSI IT Department. Firstly, all the runs are decoded using SHOE framework asking for a complete output with ROOT

Run	Trigger type	Target	Events
4305	MB	C	162102
4306	MB	C	577096
4307	MB	C	513370
4310	Frag + MB	C	1012099
4313	MB	no	57133

Table 6.1: Run list GSI2021.

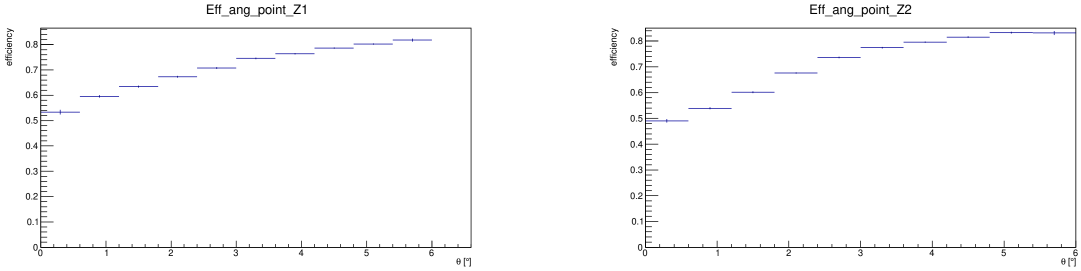

(a) MC angular efficiency for $Z = 1$

(b) MC angular efficiency for $Z = 2$

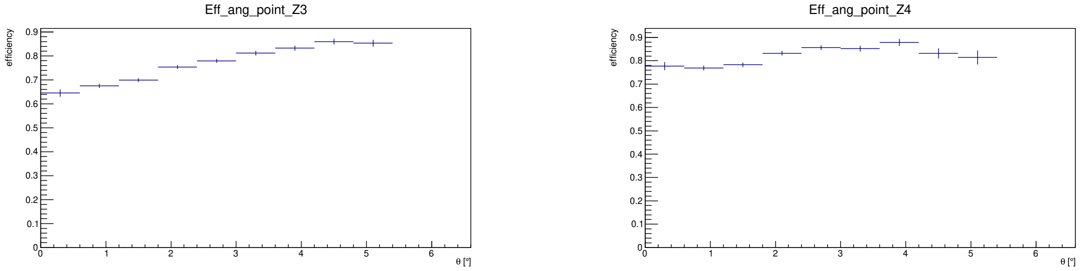

(c) MC angular efficiency for $Z = 3$

(d) MC angular efficiency for $Z = 4$

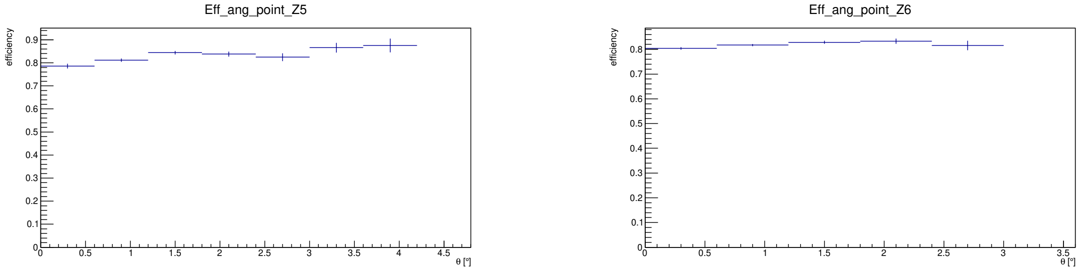

(e) MC angular efficiency for $Z = 5$

(f) MC angular efficiency for $Z = 6$

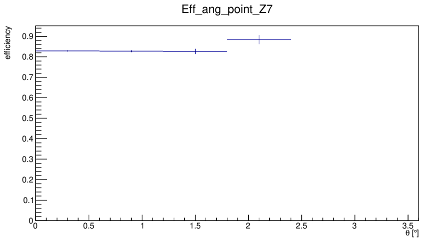

(g) MC angular efficiency for $Z = 7$

Figure 6.5: MC efficiencies vs emission angle for different fragment charge.

tree. Then, a ROOT macro was used to select interesting information from detectors included in the analysis. Eventually, all the output files were added up for the final analysis.

The goal of the preliminary analysis is to evaluate both angular and integrated elemental cross sections since there were no detectors providing the momentum or the kinetic energy of produced fragments. To this end, the elemental cross section for each Z can be written as follows:

$$\Delta\sigma(Z) = \int_{E_{\mathrm{min}}}^{E_{\mathrm{max}}} \int_{0}^{\theta_{\mathrm{max}}} \left(\frac{\partial^2 \sigma}{\partial\theta \partial E_{\mathrm{kin}}} \right) \mathrm{d}\theta \mathrm{d}E_{\mathrm{kin}} = \frac{Y(Z)}{N_{\mathrm{prim}} \cdot N_{\mathrm{TG}} \cdot \varepsilon(Z)} \tag{6.3}$$

where θ_{max} is the maximum TW detector acceptance angle (4.85°), E_{min} and E_{max} are the minimum and maximum kinetic energy, respectively, corresponding to the T_{tof} range in which charge identification algorithm works properly $(100 - 600\,\mathrm{MeV/u})$, $Y(Z)$ is the number of fragments of a given charge measured by TW, N_{prim} is the number of primaries impinging on the target, $\varepsilon(Z)$ is the total efficiency for a given charge as calculated in the previous section and N_{TG} is the number of interaction centres in the target per unit surface which can be written as

$$N_{\mathrm{TG}} = \frac{\rho \cdot \Delta x \cdot N_{\mathrm{A}}}{A} \tag{6.4}$$

where $\rho = 1.83\,\mathrm{g/cm^3}$ is the graphite target density, $\Delta x = 0.5\,\mathrm{cm}$ is the target thickness, N_{A} is the Avogadro number and $A = 12.0107$ is the graphite mass number.

Regarding angular elemental differential cross section, in Eq. 6.3 only integration in kinetic energy is performed leading to the following formula:

$$\frac{\mathrm{d}\sigma}{\mathrm{d}\theta}(Z) = \frac{Y(Z,\theta)}{N_{\mathrm{prim}} \cdot N_{\mathrm{TG}} \cdot \Delta\theta \cdot \varepsilon(Z,\theta)} \tag{6.5}$$

where $Y(Z,\theta)$ is the number of fragments of a given charge measured by TW within a given angle, $\varepsilon(Z,\theta)$ is the efficiency for a given charge in a given angle and $\Delta\theta$ is the bin width. The bin width was set to $10\,\mathrm{mrad}$ ($\approx 0.57°$) as already explained.

6.4.1 Detector alignment and event selection

The first step to properly analyze data is to check (and possibly correct) the alignment among detectors. Given the goal of this analysis, the alignment procedure was restricted to BM and TW.

To fully harness the fragmentation trigger presented in Sec. 5.1, the beam has to hit the TW in the crossing between the ninth bar in the front and rear layer: this means that the TW has to be moved before the acquisition according to beam position thus leading to geometry variations which have to be taken into account in the analysis. In its nominal

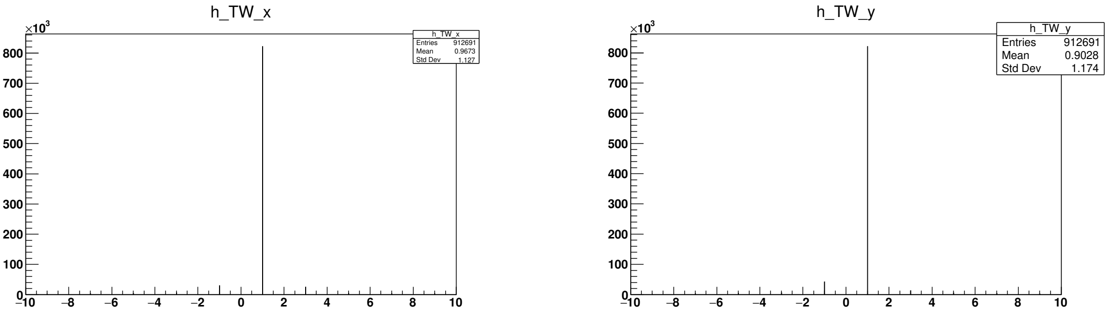

(a) TW hit X position in local frame.

(b) TW hit Y position in local frame.

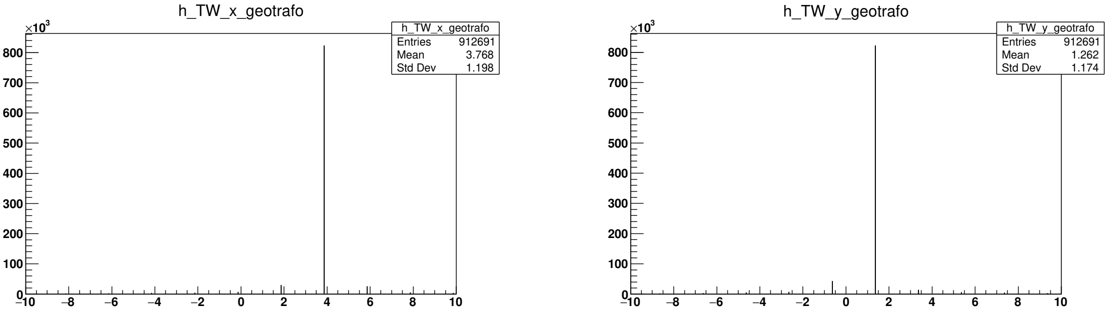

(c) TW hit X position in global frame.

(d) TW hit Y position in global frame.

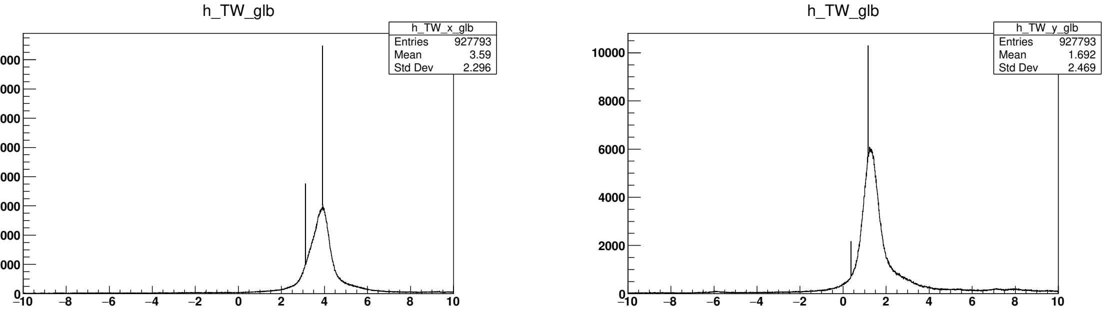

(e) BM X projection to TW position.

(f) BM Y projection to TW position.

Figure 6.6: TW hit positions and BM beam projections for alignment.

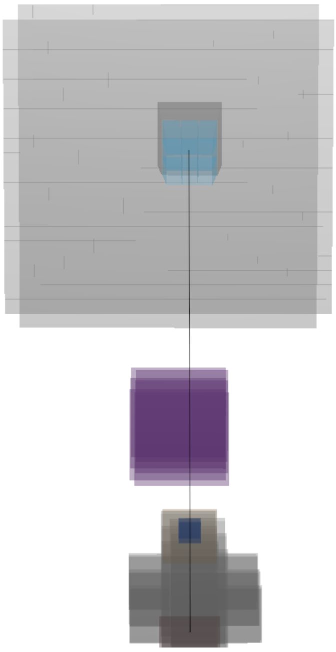

Figure 6.7: FOOT setup seen from above. The beam axis is reported in black. The TW shift with respect to other detectors can be noticed.

position, the beam should hit the TW in $(1,1)$ cm in TW local frame. The alignment is performed checking TW hits in global frame against BM projections of beam particles to the TW position. The offset resulting from their difference is the right value for the geometry map implemented in SHOE. Since tracker detectors are not included and the TW position resolution is limited to 2 cm there was no need for a finer alignment tool such as the one employed for the full setup. As the beam was a bit tilted, the final offset for TW alignment was 2.86 cm on X direction and 0.36 cm on Y direction as sketched in Fig. 6.7.

As already stated in Chap. 4, the BM has to measure the incoming direction of the beam and it has to reject pre-target fragmentation events. In the analysis, events in which the BM reconstructed only one good track were considered: with such a track, the beam intersection with the target and its projection to TW position for alignment purpose are calculated. In Fig. 6.8 an event display zoom on BM region with a good reconstructed track is reported. Since the Vertex Detector is not included, the angle of the fragment has to be calculated using the TW. In particular, the BM track is projected to the target position to find the interaction point of the primary particle. Then, the production angle of the fragment is the angle between the direction of primary particle and the flight direction of the fragment built from primary particle position in the target and TW hit position.

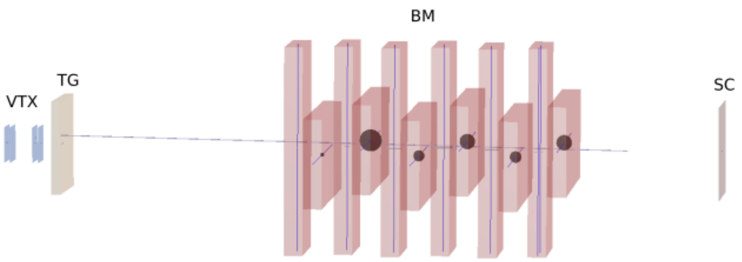

Figure 6.8: Zoom on BM region in FOOT event display. In the event a good track was reconstructed. The beam comes from right.

H	He	Li	Be
95.7 ± 0.2	98.2 ± 0.1	99.1 ± 0.2	99.3 ± 0.2
B	C	N	O
99.6 ± 0.1	99.8 ± 0.1	98.2 ± 0.1	8.46 ± 0.03

Table 6.2: Fragmentation trigger efficiencies (%) divided per fragment charge.

6.4.2 Cross section measurements

To properly calculate every kind of cross section it is mandatory to evaluate the total number of primaries considered in the analysis. The histogram with primary selection for minimum bias runs (4305, 4306, 4307) is reported in Fig. 6.9. In this context, nearly 26% of events was rejected as BM was not able to reconstruct a good track: new software developments are currently ongoing to cope with this inefficiency. As it can be seen in the histogram, in these runs no fragmentation trigger was issued since it was not activated (fourth bin): however, it is possible to recover trigger status information to check how many times the fragmentation trigger would have been fired if it was activated (fifth bin). This is a good indicator of the *acceptance factor* of the trigger: in Fig. 6.10 energy losses in the front layer of TW are reported. In black all selected events (third bin of Fig.6.9) were considered while in red only events in which fragmentation trigger would have been fired if it was requested in the run configuration. As it can be seen, the fragmentation trigger manages to remove a lot of primaries leaving almost all fragments. The acceptance factor of FOOT fragmentation trigger can be written as follows:

$$R = \frac{N_{\text{evtFragInMB}}}{N_{\text{evtMB}}} \tag{6.6}$$

and it results to be ≈ 0.1585 in MB runs. Moreover, it is possible to evaluate the bias introduced from trigger also to the yields of fragments by evaluating the trigger efficiency

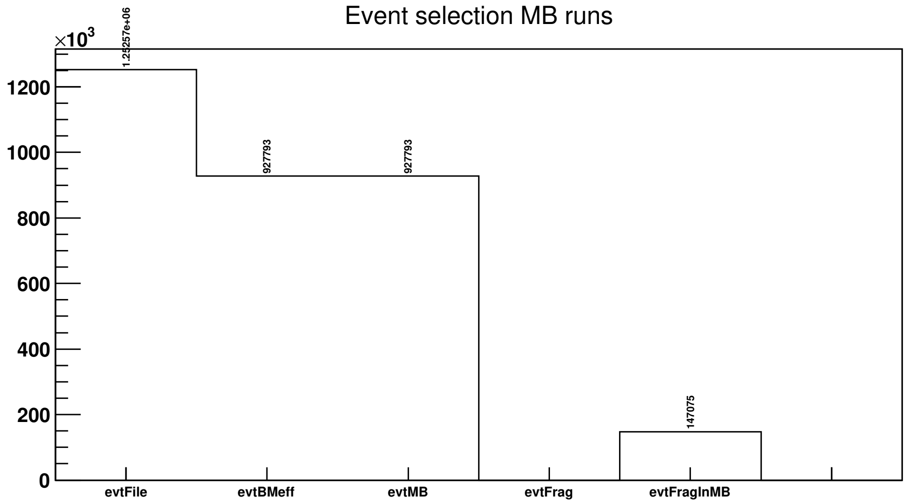

Figure 6.9: Event selection for Minimum Bias runs: total number of events in the files (first bin), events with one BM track (good events, second bin), good events acquired with MB trigger (third bin), good events acquired with fragmentation trigger (fourth bin), good events acquired with MB trigger in which also fragmentation trigger was fired (fifth bin).

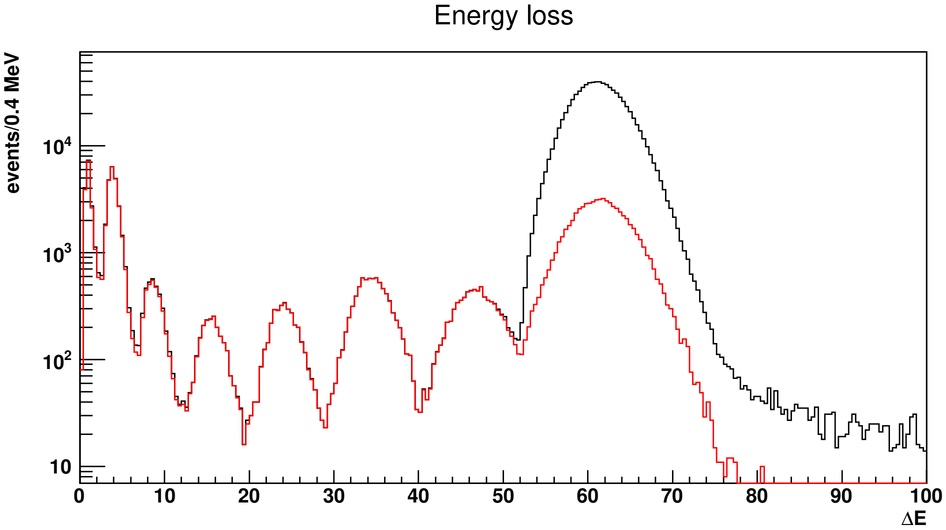

Figure 6.10: Energy loss in the front layer of TW for MB runs. In black all MB events are reported while in red only MB events in which fragmentation trigger would have been fired. The trigger is able to reject mostly primaries while accepting almost all the fragments.

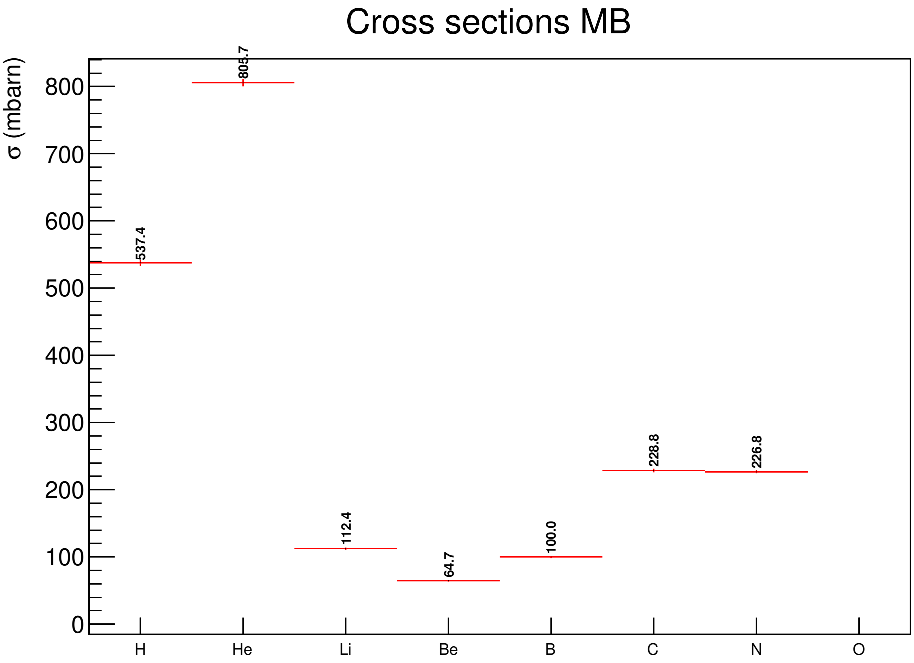

Figure 6.11: Elemental fragmentation cross section from Minimum bias runs.

for a given charge:

$$\varepsilon_{\text{frag}}(Z) = \frac{N_{\text{evtFragInMB}}(Z)}{N_{\text{evtMB}}(Z)}. \tag{6.7}$$

Indeed, the fragmentation trigger is sensitive to low ΔE energy release and it can introduce a bias due to inefficiencies in detecting low-Z fragments. In Table 6.2 fragmentation trigger efficiencies divided per fragment charge are reported. As expected, low-Z fragments have a slightly lower efficiency with respect to other fragments.

These quantities are particularly useful to scale the number of primaries and fragment yields when dealing with fragmentation runs. Moreover, the comparison of the ratios between all detected particles with $Z < 8$ and the total number of particles in MB bias and fragmentation events suggests that in this configuration a fragment production gain as high as 6 can be achieved, thus enhancing the share of interesting events.

Resolving Eq. 6.3 for minimum bias runs it is possible to evaluate elemental fragmentation cross sections reported in Fig. 6.11. In this case the number of selected events reported in the second bin of Fig. 6.9 is considered as the number of primaries N_{prim}.

On the other hand, when dealing with fragmentation run, some corrections have to be applied. Firstly, during the considered run, a mixed trigger strategy was employed: namely, all events with fragmentation trigger were acquired together with 1/10 of Minimum Bias events. This brings to the histogram in Fig. 6.12 in which, among good events,

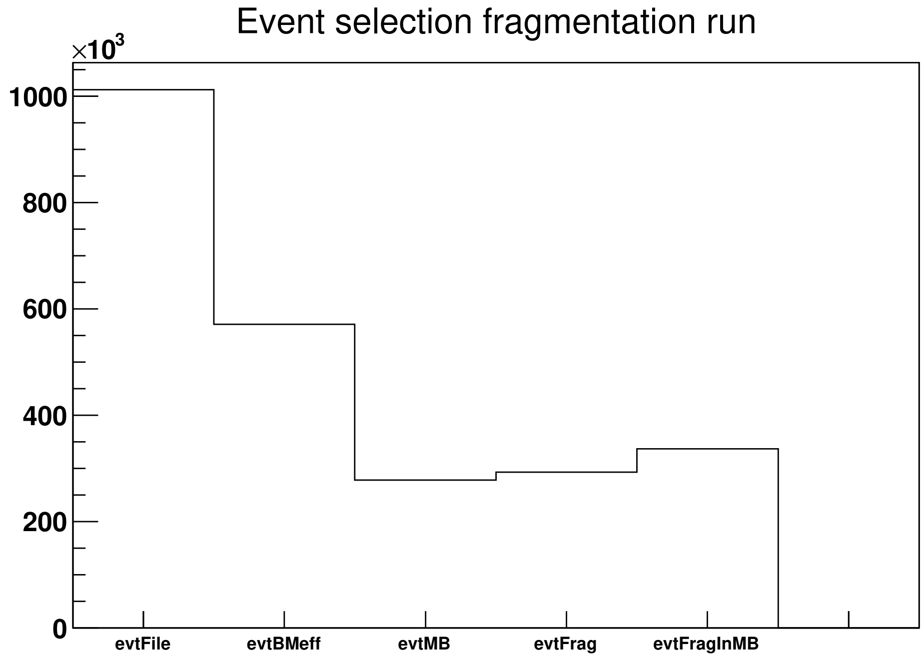

Figure 6.12: Event selection for fragmentation+MB runs: total number of events in the files (first bin), events with one BM track (good events, second bin), good events acquired with MB trigger (third bin), good events acquired with fragmentation trigger (fourth bin), good events acquired either with fragmentation and MB trigger in which also fragmentation trigger was fired (fifth bin).

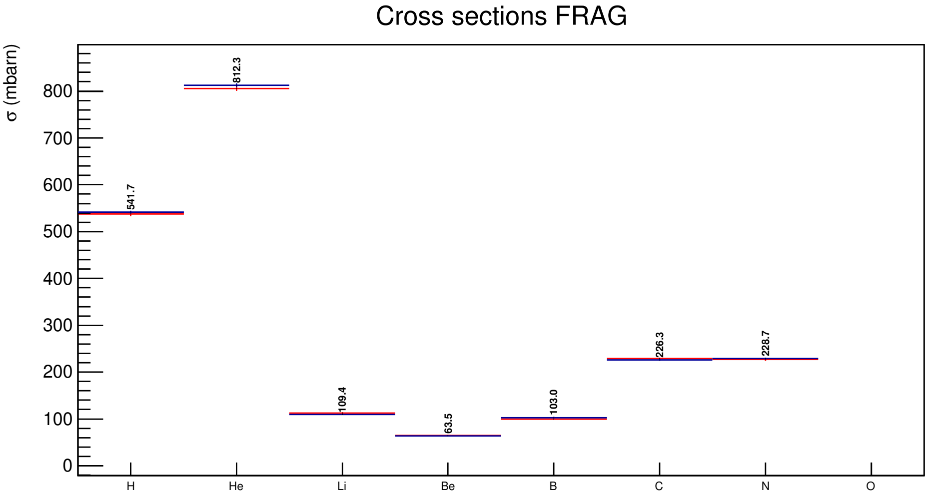

Figure 6.13: Elemental fragmentation cross section from fragmentation runs with numerical values (blue) and from MB runs (red).

the sample is almost equally divided between events acquired with fragmentation trigger and those acquired with MB. In the following, only events acquired with fragmentation trigger will be considered.

Before applying Eq. 6.3, it is needed to rescale both the number of primaries and the yields of fragments using the acceptance factor and the fragmentation trigger efficiencies as outlined in the previous discussion, in particular:

$$
\begin{aligned}
&N_{\text{prim}} = N_{\text{frag}}/R \\
&Y(Z) \to Y(Z)/\varepsilon_{\text{frag}}(Z).
\end{aligned}
$$

After the rescaling the measured cross section are reported in Fig. 6.13. In addition, angular fragmentation cross sections for different fragment charges in MB runs are also reported in Fig. 6.14.

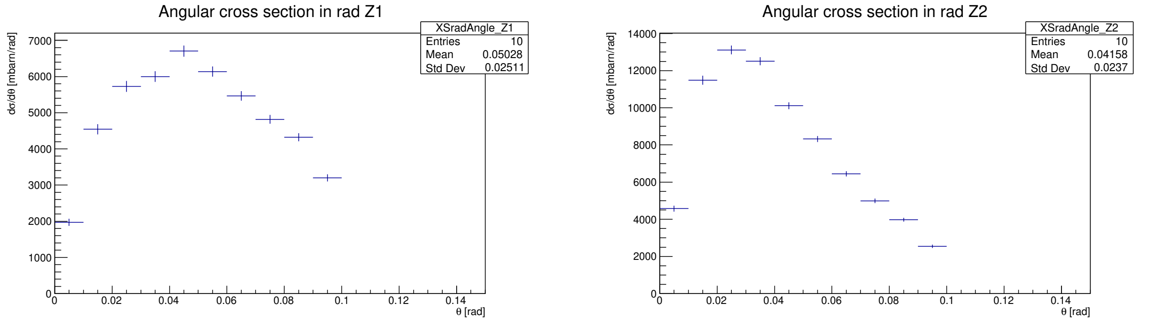

(a) Angular differential cross section for $Z = 1$ (b) Angular differential cross section for $Z = 2$

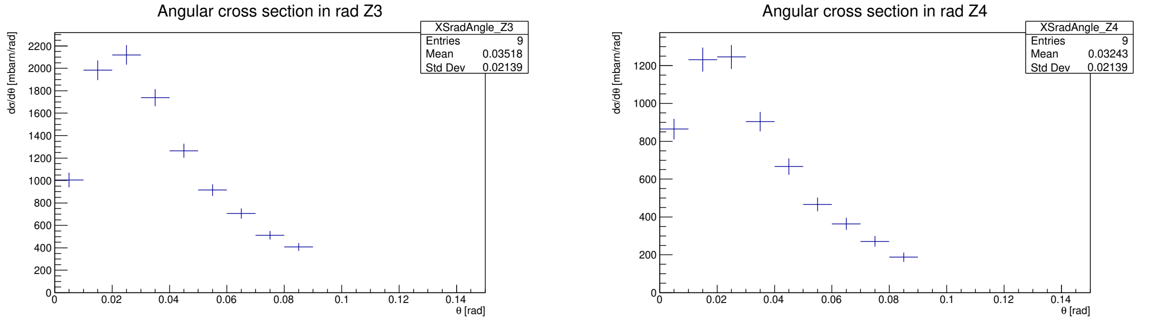

(c) Angular differential cross section for $Z = 3$ (d) Angular differential cross section for $Z = 4$

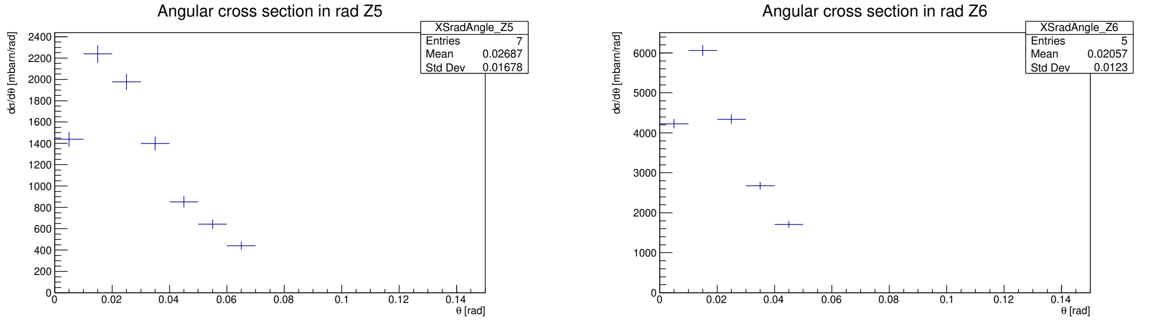

(e) Angular differential cross section for $Z = 5$ (f) Angular differential cross section for $Z = 6$

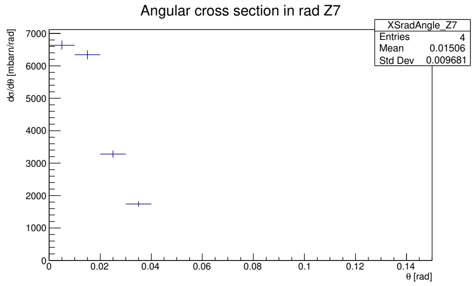

(g) Angular differential cross section for $Z = 7$

Figure 6.14: Angular differential cross sections for different fragment charge in MB runs.

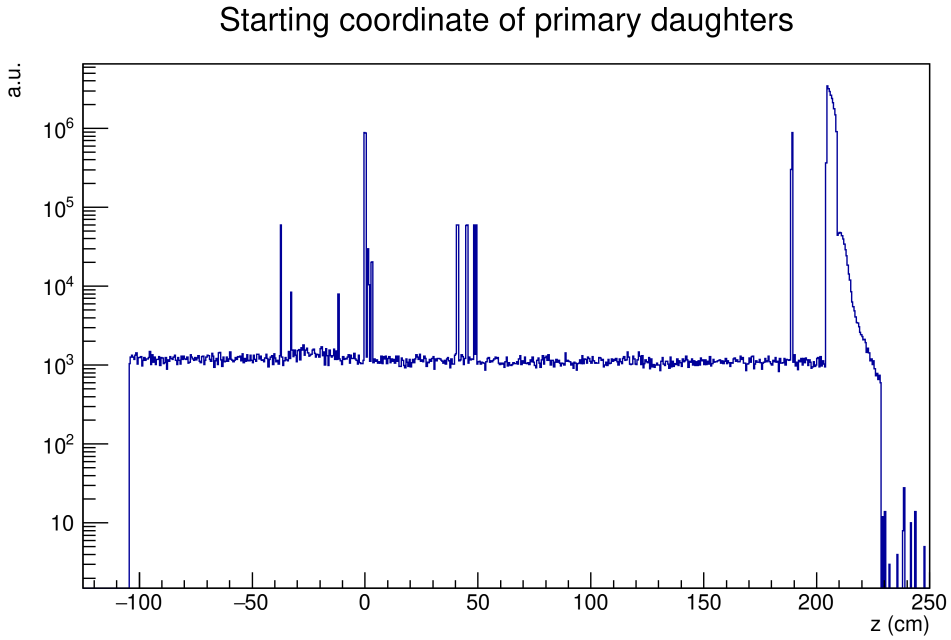

Figure 6.15: z coordinate of production of all charged fragments in Monte Carlo sample of 5×10^6 400 MeV/u ^{16}O primaries. Fragmentations due to air and detectors are visible accounting for $\approx 30\%$ of all fragmentations.

6.4.3 Background subtraction

As already stated at the beginning of this Chapter, tracking detectors are not included in this analysis. Therefore, they cannot provide useful information to remove the background composed by primary beam fragmentation outside the target. For this reason, a run without target (4313) was included in the analysis.

The out-of target fragmentation turns to be not negligible given the path length of fragments travelling in air. Looking back to Monte Carlo sample and scoring the z coordinate (i.e. along the beam path) of all charged fragments produced, one can find that almost 30% of fragmentation events occurs out of the target, especially in the air as reported in Fig. 6.15.

The same background contribution can be found in data: in Fig. 6.16 energy loss of fragments in the front layer of TW in MB runs (blue) and in no-target run (red) are reported. After rescaling for the different number of primaries it can be noticed that the background contribution is not negligible thus requiring a strategy to remove the out of target fragmentation from previous cross section measurements. Therefore, the final

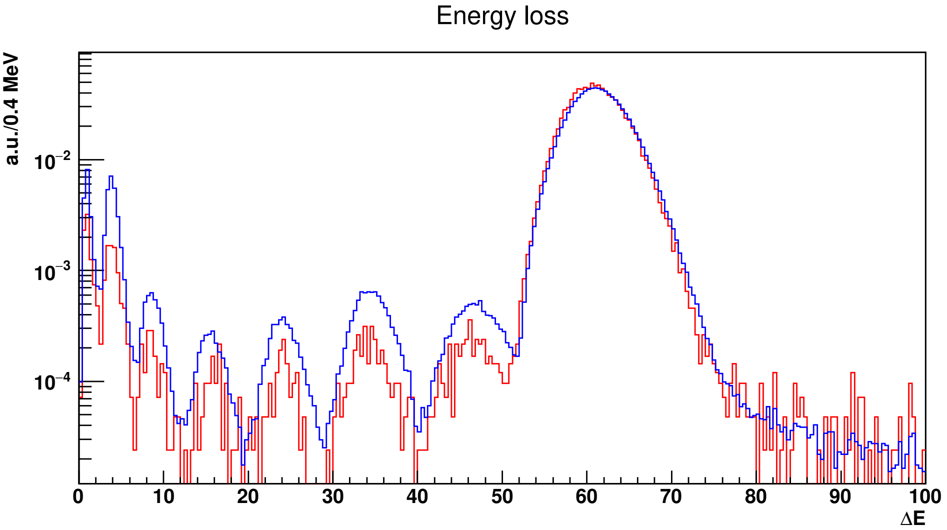

Figure 6.16: Comparison of energy loss in the front layer of TW between MB runs (blue) and no-target run (red) rescaled for the number of primaries.

Fragment	Y^{sig}	Y^{bkg}
H	16696 ± 129	339 ± 18
He	24213 ± 156	350 ± 19
Li	3591 ± 60	56 ± 8
Be	2242 ± 47	48 ± 7
B	3497 ± 59	61 ± 8
C	7944 ± 89	131 ± 11
N	8004 ± 89	179 ± 13
O	846504 ± 920	40603 ± 202

Table 6.3: Yields for different charges extracted from MB runs (Y^{sig}) and no-target run (Y^{bkg}).

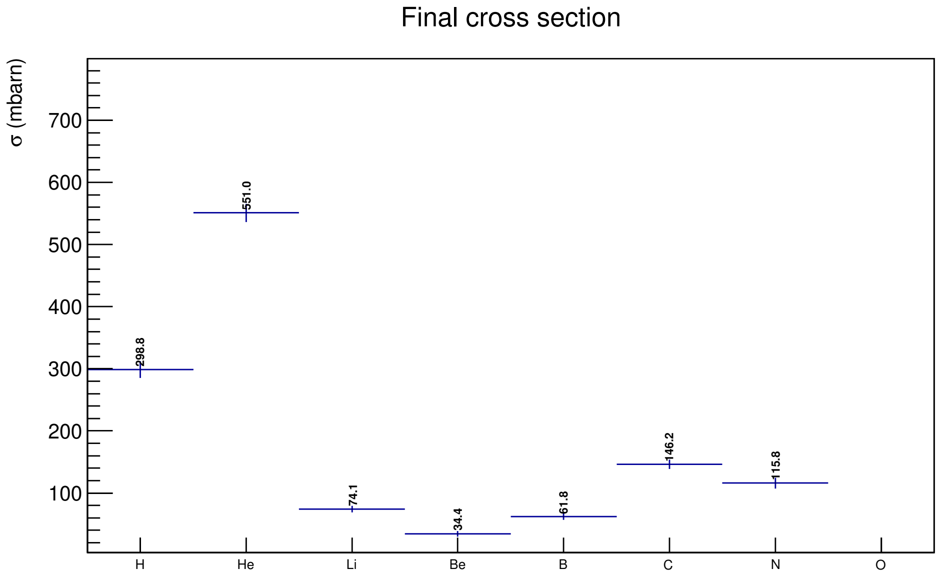

Figure 6.17: Elemental fragmentation cross section for MB runs after background subtraction.

H	He	Li	Be
299 ± 14	551 ± 15	74.1 ± 5.5	34.4 ± 4.6
B	C	N	
61.8 ± 5.2	146.2 ± 7.7	115.8 ± 8.7	

Table 6.4: Elemental fragmentation cross sections (mbarn) for MB runs after background subtraction.

fragmentation cross section can be written as follows:

$$\Delta\sigma(Z) = \frac{1}{N_{\mathrm{TG}} \cdot \varepsilon(Z)} \left(\frac{Y^{\mathrm{sig}}(Z)}{N^{\mathrm{sig}}_{\mathrm{prim}}(Z)} - \frac{Y^{\mathrm{bkg}}(Z)}{N^{\mathrm{bkg}}_{\mathrm{prim}}(Z)} \right) \tag{6.8}$$

where $Y^{\mathrm{sig}}(Z)/N^{\mathrm{sig}}_{\mathrm{prim}}(Z)$ is the yield of fragments with charge Z normalized to the number of primaries for physics runs (MB and/or fragmentation) while $Y^{\mathrm{bkg}}(Z)/N^{\mathrm{bkg}}_{\mathrm{prim}}(Z)$ is the yield of fragments with charge Z normalized to the number of primaries for no target run. Applying Eq. 6.8 to the MB runs the final elemental cross sections are shown in Fig. 6.17 and reported in Table 6.4. In the analysis, no systematic errors were considered, hence cross section values included only statistical errors. These are mainly driven by the background subtraction since the number of primaries of no target run was much lower than those of physics runs (Table 6.3).

On left column in Fig. 6.18 the angular cross sections after the background removal

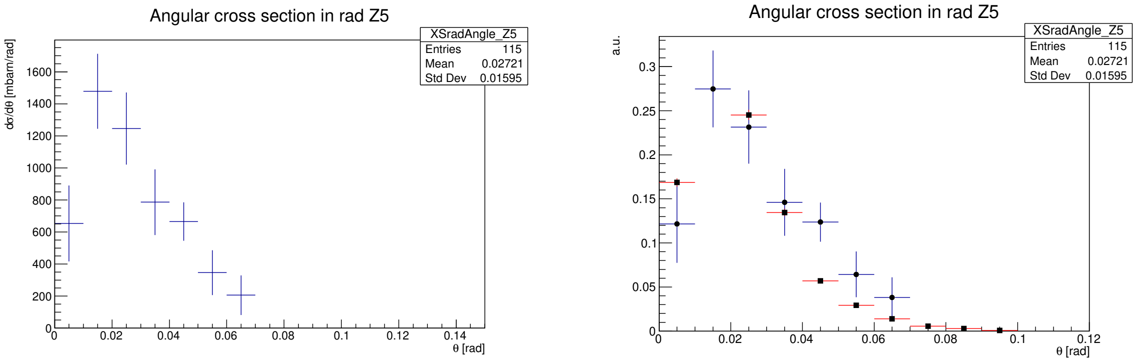

(a) Angular differential cross section after background removal for $Z = 5$

(b) Comparison of angular cross section with MC for $Z = 5$

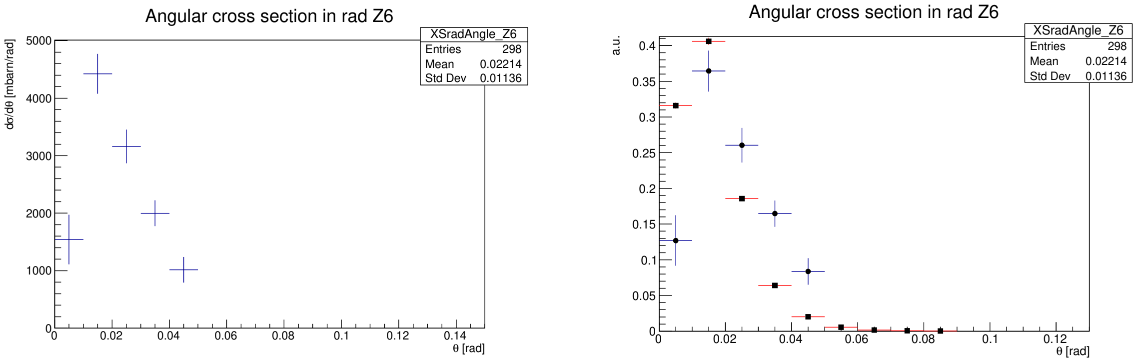

(c) Angular differential cross section after background removal for $Z = 6$

(d) Comparison of angular cross section with MC for $Z = 6$

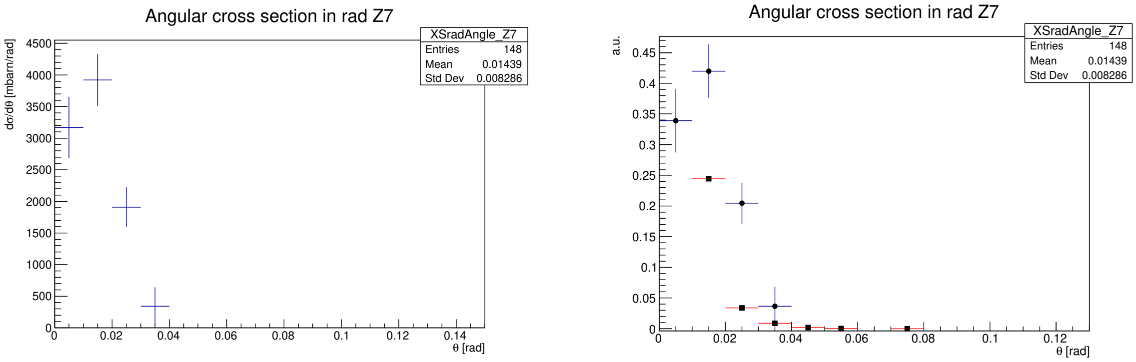

(e) Angular differential cross section after background removal for $Z = 7$

(f) Comparison of angular cross section with MC for $Z = 7$

Figure 6.18: On left column, angular cross sections after background subtraction and, on right column, their comparison (full circles) with the fragment yields in MC simulation (squares).

	This work	Ref.[70]	Weighted average	t
B	62 ± 5	70 ± 3	68.0 ± 2.6	-1.37
C	146 ± 8	131 ± 5	135.5 ± 4.2	1.66
N	116 ± 9	124 ± 4	122.6 ± 3.6	-0.86

Table 6.5: Cross sections values (mbarn) shown in Fig. 6.19. Weighted average between the measurements and t are also reported. t represents the consistency between the measurements and it is defined as the ratio of the difference between the measurements and the error on their difference.

for Boron, Carbon and Nitrogen are reported. On the right column the same plots are compared to the yields in Monte Carlo simulation after a proper scaling.

6.4.4 Comparison with literature

As already stated in Chap. 4, there are a few measurements in the beam-target configuration and energies of interest for the FOOT experiment. In particular, different charge-changing cross section measurements are available but usually there are very few elemental fragmentation cross section while there are none of (double) differential cross sections. Here a first comparison with existing data is presented. In particular, the most interesting data are reported in [70]: in this article, elemental fragmentation cross sections for different beam and target configurations (among which ^{16}O on C) are gathered. These measurements were performed through several years at NASA Space Radiation Laboratory (NSRL, New York State, US) and at the Heavy Ion Medical Accelerator in Chiba (HIMAC, Japan). The setup was composed by a telescope of lithium-drifted silicon detectors, arranged in pairs to facilitate data analysis. Those detectors placed downstream of the target at various distances with respect to the target covered different angles so that they were divided into large acceptance and small acceptance detectors. The former covered typically from 5° to 10° and they were able to identify fragments with $Z \geq Z_{\text{beam}}/2$ while the latter covered typically $1° - 2°$ and all fragment species could be resolved. However, since detectors were not segmented, they suffered from pile-up. Among the available settings in the article, 400 MeV/u ^{16}O on C target was chosen. The angular acceptance for large acceptance detectors was 6.7° while small acceptance detectors are not considered in this comparison. Firstly, the cross section results for the latter detectors include also different corrections given the angular emission of low-Z fragments exceeding the geometrical acceptance. Moreover, the angular acceptance of large acceptance detector is much closer to the one of the present analysis since heavier fragments are mostly forward peaked.

Eventually, the results of the comparison for B, C and N fragments are presented in Fig. 6.19: the cross sections obtained by the present analysis are reported in black while

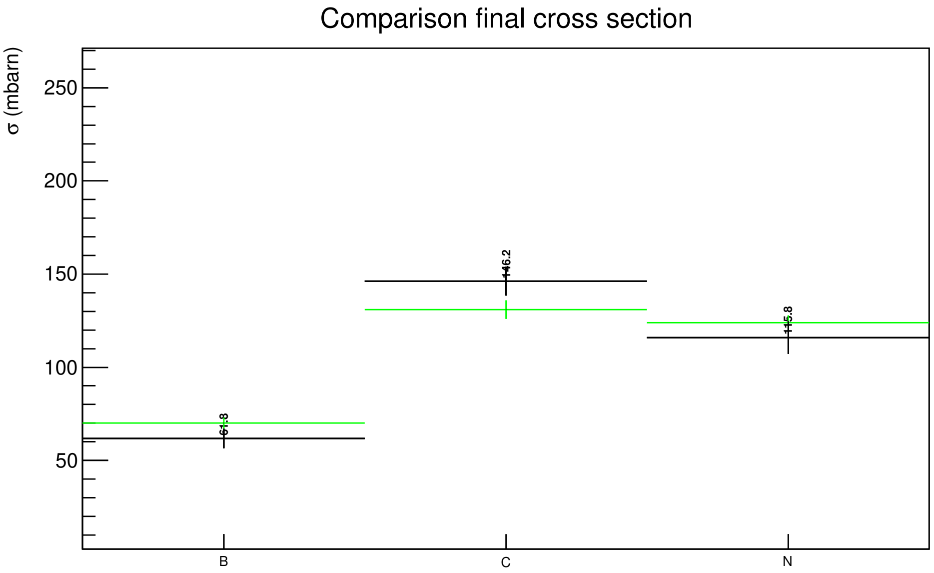

Figure 6.19: Final cross section with numerical values (black) compared to data found in [70] (green). Comparison is limited to high Z fragments.

those from the analysis performed in [70] are reported in green.

Conclusions

The FOOT experiment aims at measuring double differential cross sections of nuclear interactions of interest for hadrontherapy and space radioprotection. Final results will be used to benchmark existing Monte Carlo and deterministic codes used as treatment planning systems and as risks models for the astronauts. The experiment consists in two complementary setups: one is designed as an Emulsion Cloud Chamber to detect light fragments with a large acceptance angle while the other is designed as an electronic setup composed by a tracking system in a magnetic spectrometer to measure the momentum of the fragments and a region devoted to charge and mass identification.

In this Ph.D. project the Trigger and Data Acquisition (TDAQ) system for the electronic setup was developed. Namely, the VME boards for Beam Monitor readout and the remote detectors were included in the TDAQ. In this context, block transfer on VME boards was implemented in the system allowing a 10-fold speed up on the single read operations together with a processing of events completely decoupled from events themselves. The whole system was designed to work at a rate $\approx 2\,\mathrm{kHz}$ but tests performed with VME boards and a DE10nano board simulating a Micro Strip Detector tracking station reaches a maximum of 3.6 kHz with a periodic trigger. If block transfer on VME boards was switched off the rate fell to 900 Hz, showing its relevance to meet FOOT requirements. Using a beam simulator providing a trigger pattern similar to a real synchrotron beam, the system showed an efficiency of 40% with a mean trigger rate of 5 kHz. The code developed for remote detectors allows an acquisition rate as high as 20 kHz when slower detectors are not present.

Moreover, the online monitoring framework was enhanced to include several information for all the detectors, i.e. time synchronization among different detectors, beam shape in the whole tracking system to properly deal with misalignments and other tools to tune trigger settings. The DAQ system was extensively tested in different scenarios and it was able to take more than 40 million events at GSI in July 2021 using 200 and 400 MeV/u ^{16}O beams on Carbon (C) and Polyethylene (C_2H_4) targets. Data were acquired both with minimum bias and fragmentation trigger with an acquisition rate ranging from 200 Hz to 2 kHz depending on the beam. In that context, the online monitoring framework was able to provide a very quick feedback of the overall status of the apparatus: this was particularly useful since the beam was delivered in a non-stop run of 48 hours.

Furthermore, a first analysis on a subset of GSI data (400 MeV/u ^{16}O + C) of the elemental fragmentation cross sections for different produced charges have been obtained together with the first evaluations of the differential cross sections as a function of the fragment direction angle in the range $0 \leq \theta \leq 4.85°$. The analysis showed that the current fragmentation trigger was able to enhance the share of interesting events without spoiling the cross section evaluation. Indeed, total cross section calculated either with minimum bias and fragmentation runs gave the same results within statistical errors. To remove background due to out-of-target fragmentation, a run without target was employed. When possible, a comparison with other available measurements was performed: obtained cross sections for Boron, Carbon and Nitrogen fragments were in agreement with current data within 2σ. In particular, for Boron a value of 62 ± 5 mb for total production cross section was found, while for Carbon 146 ± 8 mb and for Nitrogen 116 ± 9 mb.

This work proved the capability of the FOOT experiment to properly address cross section measurements.

Bibliography

[1] G.F. Knoll. *Radiation detection and measurement.* 4. ed. Includes index. Hoboken, NJ: Wiley, 2010. XXVI, 830. ISBN: 9780470131480.

[2] W.R. Leo. *Techniques for Nuclear and Particle Physics Experiments.* Berlin, 1994. DOI: `10.1007/978-3-642-57920-2`.

[3] W.D. Newhauser and R. Zhang. "The physics of proton therapy". In: *Phys. Med. Biol.* 60 (2015), R155–R209. ISSN: 0031-9155. DOI: `10.1088/0031-9155/60/8/r155`.

[4] P. A. Zyla et al. "Review of Particle Physics". In: *Progress of Theoretical and Experimental Physics* 2020.8, 083C01 (Aug. 2020), p. 083C01. DOI: `10.1093/ptep/ptaa104`.

[5] C. Leroy. *Principles of radiation interaction in matter and detection.* Includes bibliographical references (p. 831-882) and index. Singapore, 2009. URL: `http://www.worldscientific.com/worldscibooks/10.1142/6872#t=toc`.

[6] R.R. Wilson. "Range, Straggling, and Multiple Scattering of Fast Protons". In: *Phys. Rev.* 71 (1947), pp. 385–386. ISSN: 0031-899X. DOI: `10.1103/physrev.71.385`.

[7] National Institute of Standards and Technology NIST. *Stopping-Power and Range Tables for Electrons, Protons, and Helium Ions.* 2017. URL: `https://www.nist.gov/pml/stopping-power-range-tables-electrons-protons-and-helium-ions`.

[8] S. P. Ahlen. "Theoretical and experimental aspects of the energy loss of relativistic heavily ionizing particles". In: *Rev. Mod. Phys.* 52 (1980). [Erratum: Rev.Mod.Phys. 52, 653–653 (1980)], pp. 121–173. DOI: `10.1103/RevModPhys.52.121`.

[9] C. Tschalär and H. D. Maccabee. "Energy-Straggling Measurements of Heavy Charged Particles in Thick Absorbers". In: *Phys.Rev.B* 1.7 (Apr. 1970), pp. 2863–2869. DOI: `10.1103/PhysRevB.1.2863`.

[10] H.W. Lewis. "Range Straggling of a Nonrelativistic Charged Particle". In: *Phys.Rev.* 85 (1952), pp. 20–24. DOI: `10.1103/physrev.85.20`.

[11] B. Rossi. *High Energy Particles.* 1952.

[12] C. Grupen and B. Schwartz. *Particle detectors.* Cambridge, UK: Cambridge Univ. Pr., 2008.

[13] H. A. Bethe. "Moliere's theory of multiple scattering". In: *Phys. Rev.* 89 (1953), pp. 1256–1266. DOI: `10.1103/PhysRev.89.1256`.

[14] V.E. Bellinzona et al. "On the parametrization of lateral dose profiles in proton radiation therapy". In: *Physica Medica* 31 (2015), pp. 484–492. ISSN: 1120-1797. DOI: `10.1016/j.ejmp.2015.05.004`.

[15] R. Frühwirth and M. Regler. "On the quantitative modelling of core and tails of multiple scattering by Gaussian mixtures". In: *Nucl. Instrum. Meth. A* 456 (2001), pp. 369–389. ISSN: 0168-9002. DOI: `10.1016/s0168-9002(00)00589-1`.

[16] K. Gunzert-Marx et al. "Secondary beam fragments produced by 200 MeV/u 12C ions in water and their dose contributions in carbon ion radiotherapy". In: *New J. Phys.* 10 (2008), p. 075003. ISSN: 1367-2630. DOI: `10.1088/1367-2630/10/7/075003`.

[17] J. Hufner, K. Schafer, and B. Schurmann. "Abrasion-ablation in reactions between relativistic heavy ions". In: *Phys. Rev. C* 12 (1975), pp. 1888–1898. DOI: `10.1103/PhysRevC.12.1888`.

[18] L. Sihver et al. "Total reaction and partial cross-section calculations in proton nucleus (Z(t) $\leq$ 26) and nucleus-nucleus reactions (Z(p) and Z(t) $\leq$ 26)". In: *Phys. Rev. C* 47 (1993), pp. 1225–1236. DOI: `10.1103/PhysRevC.47.1225`.

[19] H. L. Bradt and B. Peters. "The Heavy Nuclei of the Primary Cosmic Radiation". In: *Phys. Rev.* 77 (1950), pp. 54–70. DOI: `10.1103/PhysRev.77.54`.

[20] L. W. Townsend and J. W. Wilson. "Energy-Dependent Parameterization of Heavy-Ion Absorption Cross Sections". In: *Radiation Research* 106.3 (June 1986), p. 283. DOI: `10.2307/3576735`.

[21] R. K. Tripathi, Francis A. Cucinotta, and John W. Wilson. "Accurate universal parameterization of absorption cross sections". In: *Nuclear Instruments and Methods in Physics Research B* 117.4 (Oct. 1996), pp. 347–349. DOI: `10.1016/0168-583X(96)00331-X`.

[22] F. Horst et al. "Measurement of ^{4}He charge- and mass-changing cross sections on H, C, O, and Si targets in the energy range 70–220 MeV/u for radiation transport calculations in ion-beam therapy". In: *Phys. Rev. C* 99.1 (2019), p. 014603. DOI: `10.1103/PhysRevC.99.014603`.

[23] J. Dudouet et al. “Benchmarking GEANT4 nuclear models for hadron therapy with 95 MeV/nucleon carbon ions”. In: *Phys. Rev. C* 89.5 (2014), p. 054616. DOI: `10.1103/PhysRevC.89.054616`. arXiv: `1309.1544 [nucl-ex]`.

[24] T. T. Böhlen et al. “Benchmarking nuclear models of FLUKA and GEANT4 for carbon ion therapy”. In: *Physics in Medicine and Biology* 55.19 (Oct. 2010), pp. 5833–5847. DOI: `10.1088/0031-9155/55/19/014`.

[25] M. Durante and H. Paganetti. “Nuclear physics in particle therapy: a review”. In: *Reports on Progress in Physics* 79.9, 096702 (Sept. 2016), p. 096702. DOI: `10.1088/0034-4885/79/9/096702`.

[26] J.W. Norbury et al. “Advances in space radiation physics and transport at NASA”. In: *Life Sciences in Space Research* 22 (2019), pp. 98–124. ISSN: 2214-5524. DOI: `10.1016/j.lssr.2019.07.003`.

[27] World Health Organization. *WHO Cancer Fact Sheet.* 2021. URL: `https://www.who.int/news-room/fact-sheets/detail/cancer`.

[28] NIH National Cancer Institute. *Surveillance, Epidemiology, and End Results (SEER) Program.* 2021. URL: `https://seer.cancer.gov/`.

[29] International Atomic Energy Agency. *Radiotherapy in Cancer Care: Facing the Global Challenge.* Vienna: International Atomic Energy Agency, 2017. URL: `https://www.iaea.org/publications/10627/radiotherapy-in-cancer-care-facing-the-global-challenge`.

[30] J.M. Slater. “From X-rays to Ion Beams: A Short History of Radiation Therapy”. In: *Ion Beam Therapy.* Ed. by U. Linz. Springer, 2011. Chap. 1.

[31] R.R. Wilson. “Radiological use of fast protons”. In: *Radiology* 47 (May 1946).

[32] Particle Therapy Co-Operative Group PTCOG. *PTCOG website.* 2021. URL: `http://ptcog.ch/`.

[33] International Atomic Energy Agency. *IAEA DIRAC (DIrectory of RAdiotherapy Centres).* 2021. URL: `https://dirac.iaea.org/`.

[34] M. Dosanjh. “The changing landscape of cancer therapy”. In: *Cern Courier* 58.1 (2018), pp. 32–34.

[35] M.C. Frese et al. “Application of Constant vs. Variable Relative Biological Effectiveness in Treatment Planning of Intensity-Modulated Proton Therapy”. In: *International Journal of Radiation Oncology Biology Physics* 79.1 (Jan. 2011), pp. 80–88. DOI: `10.1016/j.ijrobp.2009.10.022`.

[36] D. Schardt, T. Elsässer, and D. Schulz-Ertner. “Heavy-ion tumor therapy: Physical and radiobiological benefits”. In: *Reviews of Modern Physics* 82.1 (Jan. 2010), pp. 383–425. DOI: `10.1103/RevModPhys.82.383`.

[37] G. Kraft. “Tumor therapy with heavy charged particles”. In: *Progress in Particle and Nuclear Physics* 45 (2000), S473–S544. ISSN: 0146-6410. DOI: `https://doi.org/10.1016/S0146-6410(00)00112-5`.

[38] M.B. Chadwick, D.T.L. Jones, and H.H. Barschall. *Nuclear data for fast neutron and proton therapy (INDC(NDS)-428)*. International Atomic Energy Agency (IAEA), 2001.

[39] R.F. Carlson. “Proton-Nucleus Total Reaction Cross Sections and Total Cross Sections Up to 1 GeV”. In: *Atomic Data and Nuclear Data Tables* 63.1 (1996), pp. 93–116. ISSN: 0092-640X. DOI: `https://doi.org/10.1006/adnd.1996.0010`.

[40] C. Grassberger and H. Paganetti. “Elevated LET components in clinical proton beams”. In: *Physics in Medicine and Biology* 56.20 (Sept. 2011), pp. 6677–6691. DOI: `10.1088/0031-9155/56/20/011`.

[41] F. Tommasino and M. Durante. “Proton Radiobiology”. In: *Cancers* 7.1 (2015), pp. 353–381. ISSN: 2072-6694. DOI: `10.3390/cancers7010353`.

[42] L. Sihver et al. “A comparison of total reaction cross section models used in FLUKA, GEANT4 and PHITS”. In: *2012 IEEE Aerospace Conference*. 2012, pp. 1–10. DOI: `10.1109/AERO.2012.6187014`.

[43] M. Durante and F.A. Cucinotta. “Physical basis of radiation protection in space travel”. In: *Rev.Mod.Phys.* 83.4 (2011), pp. 1245–1278. DOI: `10.1103/RevModPhys.83.1245`.

[44] M. Spurio. *Probes of Multimessenger Astrophysics*. 2. ed. Springer International Publishing, 2018. XIX, 591. ISBN: 9783319968537. DOI: `10.1007/978-3-319-96854-4`.

[45] Particle Data Group et al. “Review of Particle Physics”. In: *Progress of Theoretical and Experimental Physics* 2020.8 (Aug. 2020). DOI: `10.1093/ptep/ptaa104`.

[46] M. Durante and F.A. Cucinotta. “Heavy ion carcinogenesis and human space exploration”. In: *Nature Reviews Cancer* 8 (6 2008), pp. 465–472. DOI: `https://doi.org/10.1038/nrc2391`.

[47] C. Zeitlin et al. “Shielding and fragmentation studies”. In: *Radiation Protection Dosimetry* 116.1-4 (Dec. 2005), pp. 123–124. DOI: `10.1093/rpd/nci064`.

[48] J. W. Wilson et al. “Issues in Space Radiation Protection”. In: *Health Physics* 68.1 (Jan. 1995), pp. 50–58. DOI: `10.1097/00004032-199501000-00006`.

[49] John W. Norbury et al. “Are Further Cross Section Measurements Necessary for Space Radiation Protection or Ion Therapy Applications? Helium Projectiles”. In: *Frontiers in Physics* 8 (2020), p. 409. ISSN: 2296-424X. DOI: `10.3389/fphy.2020.565954`.

[50] M. Durante. “Space radiation protection: Destination Mars”. In: *Life Sciences in Space Research* 1 (2014), pp. 2–9. ISSN: 2214-5524. DOI: `https://doi.org/10.1016/j.lssr.2014.01.002`.

[51] G. Battistoni et al. “Measuring the Impact of Nuclear Interaction in Particle Therapy and in Radio Protection in Space: the FOOT Experiment”. In: *Frontiers in Physics* 8 (2021), p. 555. DOI: `10.3389/fphy.2020.568242`.

[52] J.W. Norbury et al. “Nuclear data for space radiation”. In: *Radiation Measurements* 47.5 (2012), pp. 315–363. ISSN: 1350-4487. DOI: `https://doi.org/10.1016/j.radmeas.2012.03.004`.

[53] J. Dudouet et al. “Double-differential fragmentation cross-section measurements of 95 MeV/nucleon ^{12}C beams on thin targets for hadron therapy”. In: *Phys. Rev. C* 88 (2 Aug. 2013), p. 024606. DOI: `10.1103/PhysRevC.88.024606`.

[54] L. Galli et al. “WaveDAQ: An highly integrated trigger and data acquisition system”. In: *Nuclear Instruments and Methods in Physics Research Section A: Accelerators, Spectrometers, Detectors and Associated Equipment* 936 (2019), pp. 399–400. ISSN: 0168-9002. DOI: `https://doi.org/10.1016/j.nima.2018.07.067`.

[55] Y. Dong et al. “The Drift Chamber detector of the FOOT experiment: Performance analysis and external calibration”. In: *Nuclear Instruments and Methods in Physics Research Section A: Accelerators, Spectrometers, Detectors and Associated Equipment* 986 (2021), p. 164756. DOI: `https://doi.org/10.1016/j.nima.2020.164756`.

[56] G. Galati et al. “Charge identification of fragments with the emulsion spectrometer of the FOOT experiment”. In: *Open Physics* 19.1 (2021), pp. 383–394. DOI: `10.1515/phys-2021-0032`.

[57] P. Jenni et al. *ATLAS high-level trigger, data-acquisition and controls: Technical Design Report.* Technical design report. ATLAS. Geneva: CERN, 2003. URL: `https://cds.cern.ch/record/616089`.

[58] Object Management Group OMG. *OMG website.* 2021. URL: `https://www.omg.org/`.

[59] Common Object Request Broker Architecture CORBA. *CORBA website.* 2021. URL: `https://www.omg.org/corba/`.

[60] R. Jones et al. “The OKS persistent in-memory object manager”. In: *IEEE Trans. Nucl. Sci.* 45 (1998). Ed. by J. P. Dufey, pp. 1958–1964. DOI: `10.1109/23.710971`.

[61] R. Jones et al. “Applications of CORBA in the ATLAS prototype DAQ”. In: *IEEE Trans. Nucl. Sci.* 47 (2000). Ed. by D. R. Machen, pp. 331–336. DOI: `10.1109/23.846175`.

[62] M. Barczyk et al. "Online monitoring software framework in the ATLAS experiment". In: *eConf* C0303241 (2003), THGT003. arXiv: `hep-ex/0305096`.

[63] P. F. Zema et al. "The GNAM monitoring system and the OHP histogram presenter for ATLAS". In: *ATL-DAQ-CONF-2005-029* (2005).

[64] R. Brun and F. Rademakers. "ROOT: An object oriented data analysis framework". In: *Nuclear Instruments and Methods in Physics Research A* 389 (Feb. 1997), pp. 81–86. DOI: `10.1016/S0168-9002(97)00048-X`.

[65] R. Ridolfi. "The magnetic spectrometer of the FOOT experiment". In: *Il Nuovo Cimento C* 2-3 (2021). DOI: `10.1393/ncc/i2021-21073-x`.

[66] T. Böhlen et al. "The FLUKA Code: Developments and Challenges for High Energy and Medical Applications". In: *Nucl.Data Sheets* 120 (2004), pp. 211–214. DOI: `10.1016/j.nds.2014.07.049`.

[67] J. Allison et al. "Geant4 developments and applications". In: *IEEE Transactions on Nuclear Science* 53.1 (2006), pp. 270–278. DOI: `10.1109/TNS.2006.869826`.

[68] A.C. Kraan et al. "Charge identification of nuclear fragments with the FOOT Time-Of-Flight system". In: *Nuclear Instruments and Methods in Physics Research Section A: Accelerators, Spectrometers, Detectors and Associated Equipment* 1001 (2021), p. 165206. ISSN: 0168-9002. DOI: `https://doi.org/10.1016/j.nima.2021.165206`.

[69] T. Ullrich and Z. Xu. *Treatment of Errors in Efficiency Calculations*. 2012. arXiv: `physics/0701199`.

[70] C. Zeitlin et al. "Fragmentation of ^{14}N, ^{16}O, ^{20}Ne, and ^{24}Mg nuclei at 290 to 1000 MeV/nucleon". In: *Phys. Rev. C* 83 (3 Mar. 2011), p. 034909. DOI: `10.1103/PhysRevC.83.034909`.